

Electronic Theses and Dissertations, 2004-2019

2018

Creating a Consistent Oceanic Multi-decadal Intercalibrated TMI-GMI Constellation Data Record

Ruiyao Chen
University of Central Florida

 Part of the [Electrical and Computer Engineering Commons](#)
Find similar works at: <https://stars.library.ucf.edu/etd>
University of Central Florida Libraries <http://library.ucf.edu>

This Doctoral Dissertation (Open Access) is brought to you for free and open access by STARS. It has been accepted for inclusion in Electronic Theses and Dissertations, 2004-2019 by an authorized administrator of STARS. For more information, please contact STARS@ucf.edu.

STARS Citation

Chen, Ruiyao, "Creating a Consistent Oceanic Multi-decadal Intercalibrated TMI-GMI Constellation Data Record" (2018). *Electronic Theses and Dissertations, 2004-2019*. 5816.
<https://stars.library.ucf.edu/etd/5816>

**CREATING A CONSISTENT OCEANIC MULTI-DECADAL
INTERCALIBRATED TMI-GMI CONSTELLATION DATA RECORD**

by

RUIYAO CHEN

B.S. Electrical Engineering, Wuhan University of Science and Technology, 2012
M.S. Electrical Engineering, University of Central Florida, 2014

A dissertation submitted in partial fulfillment of the requirements
for the degree of Doctor of Philosophy
in the Department of Electrical Engineering and Computer Science
in the College of Engineering and Computer Science
at the University of Central Florida
Orlando, Florida

Spring Term
2018

Major Professor: W. Linwood Jones

© 2018 Ruiyao Chen

ABSTRACT

The Tropical Rainfall Measuring Mission (TRMM), launched in late November 1997 into a low earth orbit, produced the longest microwave radiometric data time series of 17-plus years from the TRMM Microwave Imager (TMI). The Global Precipitation Measuring (GPM) mission is the follow-on to TRMM, designed to provide data continuity and advance precipitation measurement capabilities. The GPM Microwave Imager (GMI) performs as a brightness temperature (T_b) calibration standard for the intersatellite radiometric calibration (XCAL) for the other constellation members; and before GPM was launched, TMI was the XCAL standard. This dissertation aims at creating a consistent oceanic multi-decadal T_b data record that ensures an undeviating long-term precipitation record covering TRMM-GPM eras. As TMI and GMI share only a 13-month common operational period, the U.S. Naval Research Laboratory's WindSat radiometer, launched in 2003 and continuing today provides the calibration bridge between the two. TMI/WindSat XCAL for their >9 years' period, and WindSat/GMI XCAL for one year are performed using a robust technique developed by the Central Florida Remote Sensing Lab, named CFRSL XCAL Algorithm, to estimate the T_b bias of one relative to the other. The 3-way XCAL of GMI/TMI/WindSat for their joint overlap period is performed using an extended CFRSL XCAL algorithm. Thus, a multi-decadal oceanic T_b dataset is created. Moreover, an important feature of this dataset is a quantitative estimate of the T_b uncertainty derived from a generic Uncertainty Quantification Model (UQM). In the UQM, various sources contributing to the T_b bias are identified systematically. Next, methods for quantifying uncertainties from these sources are developed and applied individually. Finally, the resulting independent uncertainties are combined into a single overall uncertainty to be associated with the T_b bias on a channel basis. This

dissertation work is remarkably important because it provides the science community with a consistent oceanic multi-decadal *Tb* data record, and also allows the science community to better understand the uncertainty in precipitation products based upon the *Tb* uncertainties provided.

*To Mom & Dad for your love, strength, effort, hard work that drive me to this far. You are
the biggest inspiration in my entire life.*

To my brother Peng, you are special and wonderful in my heart

*To my husband Bing for making me laugh, wiping my tears, hugging me tight, and keeping
me strong. You are my everything.*

ACKNOWLEDGMENTS

I would like to express my sincere gratefulness and appreciation to my advisor, Dr. W. Linwood Jones, for his guidance, dedication, patience, and support over the years. Your mentorship has propelled me into the professional I am in and has pushed me beyond my goals.

I would like to thank my committee members: Dr. Wasfy Mikhael, Dr. Lei Wei, Dr. Thomas Wilheit and Dr. Darren McKague for their ideas, discussions and comments that have been absolutely invaluable for this dissertation.

I would like to acknowledge Dr. Daoji Li for sharing his statistical expertise during this process. I would like to thank Dr. David Draper for his response to my technical questions regarding satellite instruments. I would like to thank the NASA GPM XCAL Working Group for creating the space for knowledge sharing and discussions.

I would like to thank all my colleagues and friends in CFRSL for their unflinching support and encouragement, and for bringing out the potential in me. I really appreciate all the good times we shared together in the workplace. You are all the best.

I would like to acknowledge the NASA Precipitation Processing System for providing satellite data for this dissertation work. The financial support to pursue my Ph.D. degree was sponsored by NASA grants.

TABLE OF CONTENTS

LIST OF FIGURES	x
LIST OF TABLES	xvi
1 INTRODUCTION	1
1.1 Significance of Radiometric Intercalibration	1
1.2 History of GPM XCAL Group.....	1
1.3 Dissertation Objectives	2
1.4 Dissertation Overview.....	3
2 INSTRUMENTS.....	4
2.1 TMI.....	4
2.2 GMI.....	6
2.3 WindSat.....	7
3 CFRSL XCAL ALGORITHM	9
3.1 Gridding Process	10
3.2 Spatial and Temporal Collocation.....	10
3.3 Ocean Radiative Transfer Model	11
3.4 CFRSL XCAL Algorithm	13
3.5 Ocean Radiative Transfer Model Impact on CFRLS XCAL Algorithm	14
3.5.1DD Sensitivity to Atmospheric Absorption Models.....	14
3.5.3 DD Sensitivity to Ocean Surface Emissivity Models	15
4 THREE-WAY INTER-SATELLITE RADIOMETRIC CALIBRATION BETWEEN GMI, TMI AND WINDSAT	22

	4.1 Long-term Radiometric Intercalibration stability of TMI and WindSat	23
	4.2 Three-way Intercalibration between TMI, GMI and WindSat.....	28
5	UNCERTAINTY QUANTIFICATION MODEL	38
	5.1 Uncertainty and Error.....	39
	5.2 Uncertainty Source Classification	41
	5.3 Individual Uncertainty Estimate Quantification	42
	5.3.1 Uncertainty in Sampling Process	44
	5.3.2 Uncertainty in Geophysical Parameters.....	47
	5.3.2.1 Monte Carlo Simulation Procedure	50
	5.3.2.2 Procedure of Monte Carlo Simulation	51
	5.3.3 Uncertainty in Rayleigh Jeans Approximation	60
	5.3.4 Uncertainty in Different RTM and Different Geophysical Datasets	64
	5.4 Uncertainty Estimates Combination.....	67
6	UNCERTAINTY QUANTIFICATION OF TMI/WINDSAT AND WINDSAT/GMI INTERCALIBRATION.....	69
	6.1 UQM Applied to TMI/WindSat Intercalibration in long-term.....	69
	6.2 UQM Applied to WindSat/GMI Intercalibration.....	80
7	CONCLUSION.....	85
8	FUTURE WORK.....	86
	APPENDIX A: GPM CONSTELLATION	87
	APPENDIX B: GPM CALIBRATION	90
	APPENDIX C: ADDITIONAL ANALYSIS OF TMI/WINDSAT INTERCALIBRATION	94

LIST OF REFERENCES 100

LIST OF FIGURES

Figure 1-1 Desired Observing Characteristics for Weather and Climate Applications (*Courtesy of Graeme Stevens).....	3
Figure 2-1 The TRMM observatory with the TMI instrument circled in red.....	5
Figure 2-2 The GPM observatory with the GMI instrument circled in red.....	6
Figure 2-3 The WindSat radiometer on board the Coriolis satellite.....	8
Figure 3-1 Block diagram of the normalization process in CFRSL XCAL Algorithm.....	10
Figure 3-2 Radiative Transfer Equivalent Block Diagram.....	12
Figure 3-3 Block diagram of XCAL double difference technique.....	13
Figure 3-4 Periods of collocated datasets.....	17
Figure 3-5 <i>DD</i> from GMI & TMI inter-calibration stratified by latitude, blue line represents <i>DD</i> calculated using RSS RTM, and red line is XCAL RTM.....	18
Figure 3-6 <i>DD</i> anomaly for GMI & SSMIS-F17 with yaw = 0°/180° and asc/des orbits. Blue color represents that using RSS RTM, and red color is XCAL RTM.....	19
Figure 3-7 Triple difference between the <i>DD</i> values from GMI and TMI for XCAL and RSS RTM's by channel.....	20
Figure 4-1 Monthly average TMI-WindSat double difference bias time-series at 10 V-, 10 H, 37 V- and 37 H-pol channels, for XCAL year and 2011.....	26
Figure 4-2 Monthly average TMI-WindSat double difference bias of ascending passes at all channels, for XCAL year and 2011.....	26
Figure 4-3 Monthly average TMI-WindSat double difference of asc.(top) & dsc. (bottom) passes, through north hemisphere, at 10 V, for XCAL year and 2011.....	27

Figure 4-4 Example of near-simultaneous orbits (May 21, 2014) from GMI, TMI and WindSat on a global map (upper panel), with 3-way collocated $1^{\circ}\times 1^{\circ}$ boxes within ± 2 -hour shown in the expanded image (lower panel).	30
Figure 4-5 Distribution of 3-way collocations for GMI, TMI and WindSat over oceans, within ± 2 -hour time-window for the over-lap period of March 2014-March 2015. Upper left-hand panel presents the collocations, and the color scale represents the number. The upper right-hand panel represents TMI/WindSat <i>DD</i> biases, the lower panels are the WindSat/GMI and the TMI/GMI <i>DD</i> biases (left to right), and the color bar on the right side of each panel indicates the value of bias.	31
Figure 4-6 Monthly <i>DD</i> of 3-way inter-calibration among GMI, TMI and WindSat by radiometer channel.	33
Figure 4-7 Zonal stratification of radiometer channel <i>DD</i> 's for the overlap period.....	34
Figure 4-8 Radiometer channel bias anomalies (<i>DD</i> – mean- <i>DD</i>) stratified by the average scene T_{obs} for the reference radiometer, which is WindSat for TMI & WindSat, and GMI for the other two radiometer comparisons.	35
Figure 4-9 Radiometer channel bias anomalies (<i>DD</i> – mean- <i>DD</i>) stratified by GDAS ocean surface wind speed for the overlap period.....	36
Figure 5-1 Diagram of Uncertainty Quantification Model.	39
Figure 5-2 Sources that contribute to the calibration bias uncertainty.	42
Figure 5-3 Double difference mean and STD of the common 9 channels between TMI and GMI for the 8 cases using different temporal resolutions. The dots represent mean values, and bars crossing the dots represent the values.	46

Figure 5-4 Block diagram of RTM.	49
Figure 5-5 Select 8 regions that cover the whole oceans.....	51
Figure 5-6 An example of randomly sampled sea surface temperature histograms at region 1...	52
Figure 5-7 An example of double difference histograms for each channel at Region 1.	54
Figure 5-8 Uncertainty Estimates of 10,400 iterations grouped in region for each channel using Mono absorption model.	55
Figure 5-9 Uncertainty Estimates of 10,400iterations grouped in region for each channel using Rosenkranz absorption model.....	55
Figure 5-10 Uncertainty Estimates of 10,400 iterations grouped in channel for each region using Mono absorption model.	56
Figure 5-11 Uncertainty Estimates of 10,400 iterations grouped in channel for each region using Rosenkranz absorption model.....	57
Figure 5-12 Regional standard uncertainty along with the total standard uncertainty for each channel.....	59
Figure 5-13 Difference (ΔTb) of the Planck brightness temperature from Rayleigh-Jeans Tb at Tb varying between 0 and 300 K.	62
Figure 5-14 Difference (ΔTb) of the Planck brightness temperature and Rayleigh-Jeans Tb at frequency varying between 0 and 300 GHz.....	62
Figure 5-15 Difference (ΔDD) of ΔTb between TMI and GMI of their 9 common channels. ..	63
Figure 5-16 Standard uncertainty as a function of absolute difference between GMI and TMI frequencies.	64

Figure 5-17 Diagram of uncertainty estimation procedure for Mono and Rosenkranz model deviation.....	65
Figure 5-18 Diagram of uncertainty estimation procedure for RSS and Elsaesser model deviation.	65
Figure 5-19 Diagram of uncertainty estimation procedure for GDAS and ERA-I model deviation.	66
Figure 6-1 Mean and standard deviation of calibration bias of TMI relative to WindSat for 6 years between 2005 and 2014.	70
Figure 6-2 Monthly calibration bias of TMI relative to WindSat for 6 years between 2005 and 2014.....	72
Figure 6-3 Mean, standard deviation and spatial uncertainty of double difference bias between TMI and WindSat per channel for year 2011.	73
Figure 6-4 Mean, standard deviation and temporal uncertainty of double difference bias between TMI and WindSat per channel for year 2011.	73
Figure 6-5 Spatial uncertainties of double difference biases between TMI and WindSat per channel for 6 different years.....	74
Figure 6-6 Temporal uncertainties of double difference biases between TMI and WindSat per channel for 6 different years.	74
Figure 6-7 Uncertainty Estimates of 18,400 iterations grouped in region for each channel for TMI and WindSat intercalibration of year 2011.	76
Figure 6-8 Uncertainty Estimates of 18,400 iterations propagated from GDAS are grouped in channel for each region for TMI and WindSat intercalibration of year 2011.	76

Figure 6-9 Uncertainty Estimates from GDAS of TMI and WindSat intercalibration for the 6 years.	77
Figure 6-10 Uncertainty Estimates of TMI and WindSat intercalibration in Rayleigh-Jeans Approximation from Planck’s Law for the 6 years.	77
Figure 6-11 Uncertainty Estimates in MONO and Rosenkranz atmosphere absorption models for TMI and WindSat intercalibration for the 6 years.	78
Figure 6-12 Uncertainty Estimates in Elsaesser and RSS surface emissivity models for TMI and WindSat intercalibration for the 6 years.	78
Figure 6-13 Uncertainty Estimates in discrepancy between ERA-I and GDAS models for TMI and WindSat intercalibration for the 6 years.	79
Figure 6-14 Spatial uncertainty of WindSat/GMI intercalibration.	80
Figure 6-15 Temporal uncertainty of WindSat/GMI intercalibration.....	81
Figure 6-16 GDAS uncertainty of WindSat/GMI intercalibration grouped in region.....	82
Figure 6-17 GDAS uncertainty of WindSat/GMI intercalibration grouped in channel.....	82
Figure 6-18 Rayleigh-Jeans uncertainty of WindSat/GMI intercalibration.....	83
Figure 8-1 Latitude dependence of calibration bias of TMI relative to WindSat. The patterns are stable along the years, and the water vapor channels (19V, 19H, and 22V) present smile shape and a peak—to-peak 0.5 drift along the whole latitude range.	95
Figure 8-2 Monthly <i>DD</i> anomaly in time series from 2005 to 2014, where a cyclic pattern is shown.	96
Figure 8-3 Observed mean single difference and simulated (modeled) mean single difference of TMI relative to WindSat for the 6 years.	96

Figure 8-4 Observed and simulated *Tb* anomaly of TMI for the 6 years. 97

Figure 8-5 Observed and simulated *Tb* anomaly of WindSat for the 6 years..... 97

Figure 8-6 TMI single differences for the 6 years. 98

Figure 8-7 WindSat single differences for the 6 years. 98

Figure 8-8 Averaged *DD* anomaly for each quarter (3 months) of TMI relative to GMI for the 6 years. 99

LIST OF TABLES

Table 2-1: GMI, TMI, and WindSat instrument parameters (source: [2], [5], [6]).	7
Table 3-1 <i>DD</i> values between TMI and GMI with different atmosphere absorption models.	15
Table 3-2 Imager channels in GMI constellation.	16
Table 3-3 Mean and std of double differences.....	21
Table 4-1 <i>DD</i> mean and std between TMI and WindSat for V-pol.....	24
Table 4-2 <i>DD</i> mean and std between TMI and WindSat for H-pol.....	25
Table 4-3 Double differences mean/std, upper panel is ± 1 hr and lower panel is ± 2 hr temporal resolution.....	32
Table 5-1 Temporal resolutions.....	44
Table 5-2 Spatial resolutions.	45
Table 5-3 Standard uncertainty in sampling process.	47
Table 5-4 Uncertainty in GDAS geophysical parameters for 8 oceanic regions [25].	53
Table 5-5 Double difference bias between TMI and GMI.	58
Table 5-6 Standard uncertainties propagated from geophysical parameters.	58
Table 5-7 Regional standard uncertainties propagated from geophysical parameters.	59
Table 5-8 Standard uncertainty propagated from Rayleigh-Jeans approximation.....	64
Table 5-9 Standard uncertainty for Mono and Rosenkranz model deviation.	66
Table 5-10 Standard uncertainty for RSS and Elsaesser model deviation.....	66
Table 5-11 Standard uncertainty for GDAS and ERA-I deviation.	67
Table 5-12 rss uncertainty without GMI calibration uncertainty.....	68
Table 5-13 Combined uncertainty with GMI calibration uncertainty.	68

Table 6-1 Averaged calibration biases of TMI/ WindSat intercalibration.	70
Table 6-2 Combined standard uncertainty of TMI/ WindSat intercalibration.....	79
Table 6-3 Uncertainty from model deviation.....	83
Table 6-4 Combined uncertainty of WindSat/GMI intercalibration.....	84

1 INTRODUCTION

1.1 Significance of Radiometric Intercalibration

With an international network of multiple satellites carrying microwave radiometers with similar designs, it is possible to provide a near-real time global observations of earth radiance and to further ensure unified estimates of precipitation. Because these microwave radiometers are built and launched by different space agencies with widely varying specifications and capabilities, it is necessary that the brightness temperatures (Tb), which are the inputs to the precipitation retrieval process, be physically consistent between sensors. This means that differences in the observed Tb between sensors should agree with the expected differences based on radiative transfer model simulations that account for variations in the observing frequencies, channel bandwidths, view angles, etc. Properly accounting for sensor differences is critical to producing consistent precipitation estimates between radiometers, and this is the only way to ensure that observed changes in precipitation are real and not the result of sensor calibration issues.

1.2 History of GPM XCAL Group

The GPM Intersatellite Calibration Working (XCAL) Group was established in 2007 as an ad hoc working group within the NASA Precipitation Measurement Missions (PMM) science team. The XCAL group has responsibility for the intercalibrated level 1C Tb files that are used as input for the radiometer retrieval algorithm. Prior to the launch of GPM this involved developing the level 1C format and producing initial calibration tables for the constellation sensors using TMI as the reference standard. After the launch of the GPM Core Observatory, the XCAL group initially

focused on the GMI on-orbit radiometric calibration to ensure it provided the best possible calibration reference for the other microwave radiometers in the GPM constellation. Once the GMI calibration was finalized for the version 4 (V04) reprocessing, the group worked to identify issues affecting the calibration and stability of the constellation radiometers, developed corrections for these issues, and then produced intercalibration tables to adjust for residual sensor calibration differences in a physically consistent manner. XCAL has also served as a general-purpose consultant to the rest of the science team on radiometer technical issues [1]. The XCAL group currently consisted of four teams, namely: University of Maryland (formerly Texas A&M University, Colorado State University, University of Michigan, and the Central Florida Remote Sensing Lab (CFRSL) at the University of Central Florida.

1.3 Dissertation Objectives

Despite the difficulty in forecasting climate change and its consequences, it is imperative to address the wide uncertainties and long-term stabilities in our understanding of climate change and its effects (shown in Figure 1-1). Therefore, systematic analysis and consistent methods of incorporating uncertainty into global change assessments will become increasingly necessary. Therefore, this dissertation aims at creating a consistent, multi-decadal, intercalibrated, oceanic brightness temperature data record for TRMM-GPM eras using the WindSat as a radiometric calibration bridge for the 11-year time gap, with the focuses (1) to use WindSat to provide additional intercalibration for both TMI and GMI and (2) to develop a generic uncertainty quantification model which provides the uncertainty estimates associated with calibration bias.

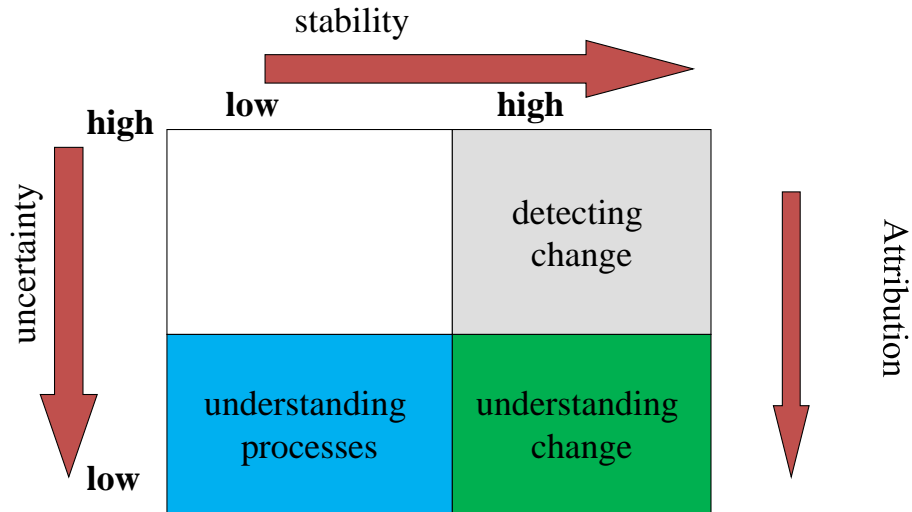


Figure 1-1 Desired Observing Characteristics for Weather and Climate Applications (*Courtesy of Graeme Stevens).

1.4 Dissertation Overview

This dissertation is aimed at creating a consistent multi-decadal oceanic brightness temperature data record for the TRMM and GPM eras. It will start with the description of TMI, GMI and WindSat instruments in Chapter 2. Chapter 3 will present the procedures involved in the CFRSL XCAL algorithm in detail. In Chapter 4, the three-way radiometric intercalibration between TMI, GMI and WindSat is shown. A generic uncertainty quantification model (UQM) is described with results analyzed in Chapter 5. It is followed with the developed UQM being applied to TMI/WindSat XCAL and WindSat/GMI XCAL, and results are presented in Chapter 6. Finally, the conclusions and future work are presented in Chapter 7 and Chapter 8 respectively.

2 INSTRUMENTS

2.1 TMI

The Tropical Rainfall Measuring Mission (TRMM) satellite (shown in Figure 2-1), a collaboration between NASA and the Japan Aerospace Exploration Agency (JAXA) that was launched into an earth orbit of 350 km (later boosted to 405 km) altitude and 35° inclination in late November 1997. This original 3-year science mission using a precipitation radar (PR) and a multi-frequency microwave radiometer (TRMM Microwave Imager, TMI) to measure the rainfall statistics in the tropics [2].

TMI was a conical scanning radiometer designed to provide rainfall measurements over a swath of 878 km. This multi-frequency, externally calibrated, total power radiometer design was a derivative of the Special Sensor Microwave/Imager (SSM/I), which has successfully operated on the Defense Meteorological Support Program (United States Air Force weather satellites) since 1987. After the TRMM mission was extended, its scientific role was expanded to include a constellation of cooperative international weather satellite programs that carried microwave radiometers capable of measuring rainfall, which later evolved into the current Global Precipitation Measurement (GPM) program. TMI eventually provided a 17-plus-year time-series of calibrated brightness temperature (T_b) that have remarkable value for investigating the effects of the Earth's climate change over the tropics [3].



Figure 2-1 The TRMM observatory with the TMI instrument circled in red.

For the TRMM constellation, the NASA project used a single satellite radiometer rain retrieval algorithm (GPROF), which assumed all the radiometers sensors were intercalibrated. Because TRMM's low earth orbit provided frequent near-simultaneous crossings with the polar satellites (carrying other microwave radiometers), TMI was selected as the radiometric transfer standard to perform inter-satellite radiometric cross-calibration (XCAL) of the constellation, until it was decommissioned in 2015. As a result, TRMM collected 17 years of rainfall data and created an invaluable rainfall climatology, which serves the international global hydrological cycle research community [1].

2.2 GMI

The follow-on Global Precipitation Measurement (GPM) mission satellite was launched in February 2014, to provide data continuity and to improve precipitation measurement capabilities. Like TRMM, the GPM observatory shown in Figure 2-2 has two primary precipitation remote sensors, namely: the Dual Frequency Precipitation Radar (DPR) and the GPM Microwave Imager (GMI). Moreover, the GPM orbit extends the coverage to over $\pm 65^\circ$ latitude, and both sensors have improved sensitivity to measure light precipitation and snow that occurs at higher latitudes. GPM now also comprises a constellation of cooperating weather and research satellites that have suitable microwave radiometers [4].



Figure 2-2 The GPM observatory with the GMI instrument circled in red.

GMI is also a conical scanning microwave radiometer with 13 channels of which 9 overlap with TMI, and 7 overlap with WindSat given in Table 2-1. The GMI instrument has a 1.2 m diameter antenna, which at 407 km altitude achieves higher spatial resolution than TMI and all other radiometers in the GPM constellation. Furthermore, based upon a successful 6-month on-orbit calibration/validation period, GMI's performance has met all requirements of radiometric sensitivity and calibration stability; and as a result, it has been designated as the new radiometric transfer standard for GPM. Based on previous experience with TMI and available on-board fuel, the GPM spacecraft is estimated to operate for 10-15 years [5].

Table 2-1: GMI, TMI, and WindSat instrument parameters (source: [2], [5], [6]).

	Channel 1 (V-pol)			Channel 2 (H-pol)			Channel 3 (V-pol)			Channel 4 (H-pol)			Channel 5 (V-pol)			Channel 6 (V-pol)			Channel 7 (H-pol)		
Freq (GHz)	10.65	10.65	10.7	10.65	10.65	10.7	18.7	19.35	18.7	18.7	19.35	18.7	23.8	21.3	23.8	36.64	37.0	37.0	36.64	37.0	37.0
B(MHz)	96.5	100	300	94.7	100	300	193	500	750	194	500	750	367	200	500	697	2000	2000	707	2000	2000
IFOV (km)	19.4	41.3	38	19.4	41.3	38	10.9	20.9	27	10.9	20.9	27	9.7	18.9	20	9.4× 15.6	11.1	13	9.4	11.1	13
	X	X	X	X	X	X	X	X	X	X	X	X	X	X	X		X	X	X	X	X
	32.1	68.1	25	32.1	68.1	25	18.1	34.6	16	18.1	34.6	16	16.0	31.1	12		18.3	8	15.6	18.3	8
EIA (deg)	52.8	53.2	50.3	52.8	53.2	50.3	52.8	53.2	55.9	52.8	53.2	55.9	52.8	53.2	53.5	52.8	53.2	53.5	52.8	53.2	53.5

* In each channel, the left column is for GMI, the middle is for TMI and the right is for WindSat. B stands for bandwidth and IFOV is instantaneous field of view.

2.3 WindSat

WindSat shown in Figure 2-3 is the world's first polarimetric microwave radiometer in space, which was developed by the Naval Research Laboratory (NRL) and launched in January 2003 on board the USAF Coriolis satellite into a 840-km sun-synchronous polar orbit [6]. The

sensor has a conically scanning reflector antenna that produces a forward-looking swath of approximately 1000 km. It consists of 22 channels of polarized Tb ; as mentioned previously, 7 channels overlap with TMI and GMI as given in Table 2-1. The WindSat radiometric calibration campaign has been believed to be an outstanding success, and excellent results have been published to provide high confidence in the Tb 's from WindSat Sensor Data Records (SDR) [6, 7].



Figure 2-3 The WindSat radiometer on board the Coriolis satellite.

3 CFRSL XCAL ALGORITHM

A robust inter-satellite calibration algorithm has been developed by CFRSL and applied to multiple microwave radiometers. It compares two satellite radiometer observations, on a channel basis, for homogeneous earth scenes, that are collocated spatially and temporally [8]. In the simplest sense, if the corresponding channels of two radiometers, with identical design, were to make an observation over the earth at the exact same time and space, the difference in their Tb 's should reflect the radiometric calibration bias between the instruments. Unfortunately, for radiometers of different designs, the situation is more complicated due to different center frequencies, bandwidths and/or earth incidence angles; thus, normalization between the radiometers is required before cross-calibration. Using the CFRSL XCAL algorithm, this normalization utilizes microwave radiative transfer theory to translate the measurement of one or the other to a common basis before comparison. This algorithm involves three procedures in the normalization process to obtain simulated Tb 's to derive the calibration biases. A block diagram of these procedures is shown in Figure 3-1.

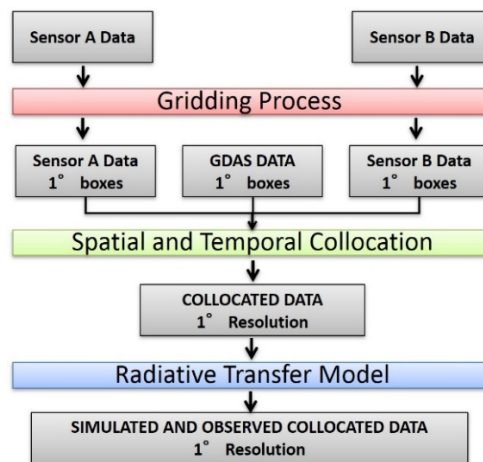


Figure 3-1 Block diagram of the normalization process in CFRSL XCAL Algorithm.

3.1 Gridding Process

In this step, the raw sensor Tb 's are averaged spatially into 1° boxes, which are generated on a per orbit basis, for each sensor and each radiometer channel. For XCAL over oceans, filters are used to select clear-sky homogeneous scenes, such as standard deviation of Tb 's per box should be no more than 2 K in V-polarization (V-pol), and 3 K in H- polarization (H-pol). Because high Tb standard deviations within a box are indicative of nonhomogeneous environmental conditions, including weather fronts with rain and/or small island contamination, these boxes are removed when standard deviations exceed 2 and 3 K for vertical and horizontal polarizations, respectively. Further editing is applied at all frequencies based on the upper limits of Tb 's expected from rain-free ocean; and a conservative land mask is also applied, to filter out possible Tb contamination from nearby land pixels.

3.2 Spatial and Temporal Collocation

To assure identical environmental conditions, the two radiometers' gridded observations along with geophysical parameters are spatially collocated within a ± 1 -hour time window. The primary geophysical parameters used are from the NOAA Global Data Assimilation System (GDAS) which uses the National Center for Environmental Prediction (NCEP) Global Forecast System (GFS) model (NCEP 2000) to provide outputs at 0000, 0600, 1200, and 1800 Greenwich Mean Time (GMT), on a $1^\circ \times 1^\circ$ latitude/longitude grid [9]. These data include the vertical profiles of atmospheric temperature, pressure, humidity, and cloud water density at 21 pressure layers, as

well as the surface measurements of sea surface temperature, and ocean wind speed at a 10-m height. For validation purpose, a second geophysical dataset known as the European Centre for Medium-Range Weather Forecasts (ECMWF) Reanalysis Interim (ERA-I) was used, which provides the same sets of geophysical parameters but with 29 layers in the atmosphere profiles [10].

3.3 Ocean Radiative Transfer Model

When the same earth scene is observed by two radiometers of different designs, there might be significant differences in their respective brightness temperature measurements, which does not necessarily constitute calibration errors (e.g., different frequencies and incidence angles would result in different Tb 's); but with the use of a Radiative Transfer Model (RTM), it is possible to determine the expected theoretical difference in their Tb 's [11].

A block diagram of the XCAL Ocean RTM is given in Figure 3-6. This model is used to calculate the apparent brightness temperature (Tb) at the aperture of the satellite radiometer antenna, which is the desired sensor measurement. Because of an imperfect antenna and transmission losses between the antenna and receiver, the antenna temperature T_A is different from the desired T_b . Nevertheless, through the application of appropriate calibration and correction algorithms, the T_A may be converted into a precise estimate of Tb . The Tb at polarization p is the result of the scalar sum of three components of brightness temperature given by

$$Tb(\text{satellite}) = \gamma_a(T_{SE}^p + T_{scat}^p) + T_{up} \quad (1)$$

where γ_a is the one-way atmospheric transmissivity, T_{SE} is the ocean surface emission, T_{scat} is the downwelling atmospheric emission that undergoes specular reflection, and T_{up} is the upwelling atmospheric temperature. Thus the RTM is a collection of subroutines that compute these

components, and the current NASA XCAL RTM comprises the Remote Sensing System (RSS) ocean emissivity model [12] and the Mono atmospheric absorption model [13]. Further, the RTM requires knowledge of the pertinent environmental parameters from the atmosphere and ocean surface, which are provided by numerical weather model outputs (GDAS or ERA-I).

Moreover, the XCAL group continues to evaluate and update the RTM used for intersatellite radiometric calibration; however, by agreement, each member uses the same RTM and evaluation dataset to perform their independent analysis. In this manner, the differences between radiometric biases are mostly technique related and much less dependent on RTM. Moreover, the resulting T_b differences are removed when the various satellite radiometers are normalized to the constellation radiometric standard (TMI or GMI).

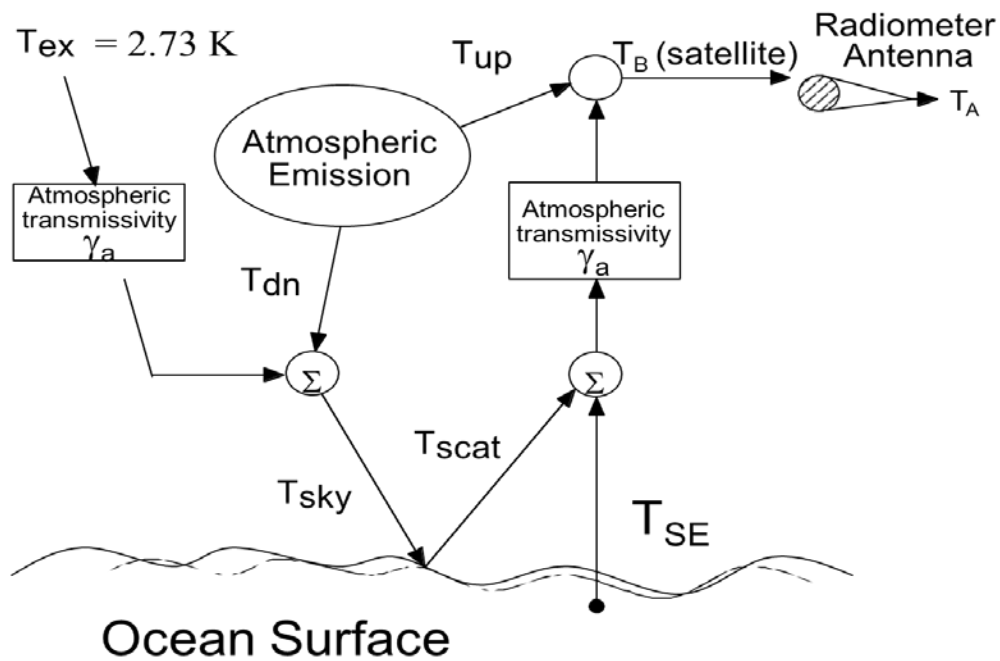


Figure 3-2 Radiative Transfer Equivalent Block Diagram.

3.4 CFRSL XCAL Algorithm

Because the environmental parameter inputs derived from numerical weather models, as well as the physics of the radiative transfer theory, are not perfect, the simulated Tb 's may have absolute Tb offsets of several Kelvin, which is not acceptable for inter-satellite calibration. To mitigate these effects Gopalan [11], developed a technique, which calculated the difference between differences (double difference) of measured and modeled (theoretical RTM) brightness temperatures. This approach was subsequently improved by Biswas et al. [8] and became the CFRSL XCAL algorithm shown in Figure 3-3. Thus using the double differences, the imperfect physics in the RTM, errors in the associated environmental parameters from GDAS, and the effects of frequency and EIA differences between radiometers, are mostly common mode and usually cancel.

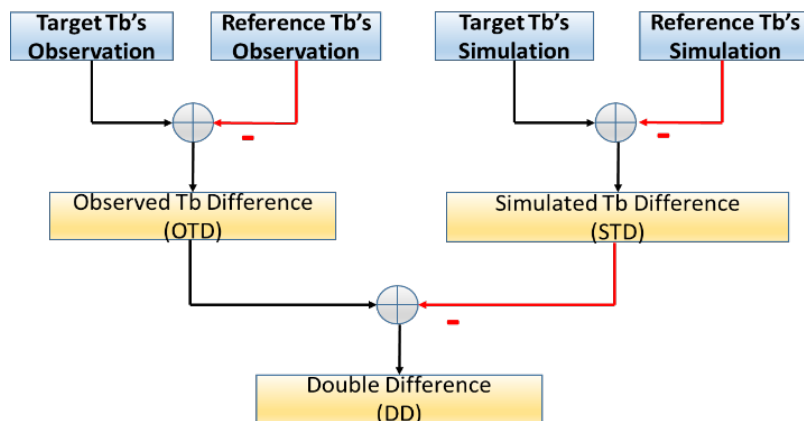


Figure 3-3 Block diagram of XCAL double difference technique.

In this algorithm, there are two radiometers being cross calibrated, namely: the target radiometer (sensor to be calibrated) and the radiometric standard (reference). Within a 1° Lat/Lng box, the observed Tb 's for a particular channel are averaged to improve the noise equivalent delta-

Tb , NEDT, and to produce the REF_{obs} and TGT_{obs} . Next, the oceanic RTM (Section 3.3) is run, using the collocated environmental parameters and given sensor parameters (frequency, incidence angle and polarization), to produce theoretical simulated Tb for REF_{sim} and TGT_{sim} . The expected Tb single difference is defined as $(TGT_{sim} - REF_{sim})$, and the observed single difference is $(TGT_{obs} - REF_{obs})$. The final step is to calculate the double difference (DD), which is the Tb bias as:

$$Tb_{bias} = DD = (TGT_{obs} - REF_{obs}) - (TGT_{sim} - REF_{sim}) \quad (2)$$

This technique essentially cancels out any absolute bias that may exist in the RTM, and it represents the radiometric bias of the target radiometer with respect to the reference radiometer. Before retrieving precipitation, this bias will be then applied to the target radiometer Tb to be consistent with the reference radiometer (calibration transfer standard) that is usually TMI or GMI.

3.5 Ocean Radiative Transfer Model Impact on CFRLS XCAL Algorithm

The use of an oceanic RTM is an integral part of our CFRSL XCAL algorithm. Because the RTM physics is imperfect and because the geophysical parameters are likewise only estimates of their true values based on numerical weather models, it is important to assess the sensitivity of the derived Tb biases to these limitations.

3.5.1 DD Sensitivity to Atmospheric Absorption Models

Previously, the Rosenkranz models were used by the GPM XCAL Group to calculate the atmospheric absorption coefficients for: water vapor (WV) [14], cloud liquid water (CLW) [15],

oxygen [16], and nitrogen[17]; later the monochromatic RTM (MONO, MonoRTM) [13] replaced the Rosenkranz water vapor sub-routine in the RTM.

The *DD* bias between TMI and GMI are calculated using both models, and the results are presented in Table 3-1. Significant differences between these calculations occur for the channels at 23 V and the 19 V & H channels. The cause of this is suspected to be the imperfect simulation of the water vapor profiles in the numerical weather models and inadequate knowledge of the radiative transfer modeling near the 22.235 GHz water vapor line.

After considerable study within the XCAL working group, the MonoRTM was chosen to be included in the current XCAL RTM, and it was concluded that the disagreement between the two atmospheric absorption models can contribute to the uncertainty associated with the *DD* bias.

Table 3-1 *DD* values between TMI and GMI with different atmosphere absorption models.

	10V	10H	19V	19H	23V	37V	37H	89V	89H
MONO <i>DD</i>	0.70	0.56	0.16	0.71	0.03	-0.82	1.05	0.19	-0.80
Rosenkranz <i>DD</i>	0.72	0.58	0.45	1.23	1.07	-0.75	1.07	0.25	-0.60

3.5.2 DD Sensitivity to Ocean Surface Emissivity Models

The contents of this section have been published in the following article:

R. Chen, H. Ebrahimi, and W. L. Jones, “Sensitivity of XCAL double difference approach to ocean surface emissivity and its impact on inter-calibration in GPM constellation,” in 2016 IEEE International Geoscience and Remote Sensing Symposium (IGARSS), 2016, pp. 871–874 [18].

In this section, the inter-calibration between GMI and other constellation satellite microwave radiometers is presented for 9 microwave imager channels ranging from 10 to 89 GHz (see Table 3-2), using the CFRSL XCAL algorithm with two different ocean surface emissivity models. The first RTM, known as XCAL, uses the ocean surface emissivity model by Elsaesser [19]; and the second RTM, known as Remote Sensing Systems (RSS), replaces the surface emissivity model with that of Meissner and Wentz [12]. The major difference of these models is the dependence of the surface emissivity with ocean roughness (surface wind speed). Because the majority of the imager channels' T_b comes from the ocean surface, it is important that we assess the impact of these two models on the derived DD biases.

Table 3-2 Imager channels in GMI constellation.

	GMI	TMI	WindSat	AMSR2	SSMIS
Channel #	Central Freq & Pol	Central Freq & Pol	Central Freq & Pol	Central Freq & Pol	Central Freq & Pol
1	10.65 V	10.65 V	10.70 V	10.70 V	-
2	10.65 H	10.65 H	10.70 H	10.70 H	-
3	18.70 V	19.35 V	19.35 V	18.70 V	19.35 V
4	18.70 H	19.35 H	19.35 H	18.70 H	19.35 H
5	23.80 V	21.30 V	23.80 V	23.80 V	22.235 V
6	36.64 V	37.00 V	37.00 V	36.50 V	37.00 V
7	36.64 H	37.00 H	37.00 H	36.50 H	37.00H
8	89.00 V	85.50 V	-	89.00 V	91.655 V
9	89.00 H	85.50 H	-	89.00 H	91.655 H

The periods of the datasets used are shown in Figure 3-4 for different pairs of radiometers, and the corresponding results are analyzed to assess the robustness of the CFRSL XCAL algorithm to the selection of the ocean surface emissivity model.

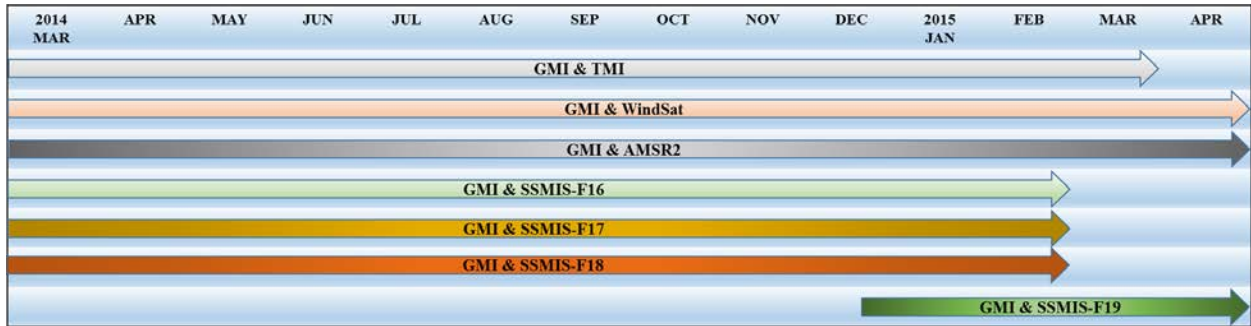


Figure 3-4 Periods of collocated datasets.

The experimental data set consisted of individual 1° boxes with associated *DD* biases computed using two independent RTMs. The usual analysis procedure is to sort the boxes in various manners and to display the *DD* biases versus different parameters e.g., time, space (latitude), or environmental parameters (sea surface temperature, wind speed, integrated atmospheric water vapor and cloud liquid water). The expectation is that the true radiometric bias is a constant, independent of the sorting method.

An example of the *DD* biases between GMI and TMI for the two RTM's (red = XCAL and blue = RSS) is plotted versus the box latitude in Figure 3-5. Data symbols are the mean *DD*'s calculated over the corresponding box latitude bins for the ~ 1-year period. Note that 10 GHz and 37 GHz results are “flat”, which indicates that the CFRSL XCAL algorithm is working well and that the results are nearly the same for both RTM's. Results for 89 GHz are similar except there is an offset of ~ 0.2 K for the H-pol, which indicates a sensitivity to the RTM used.

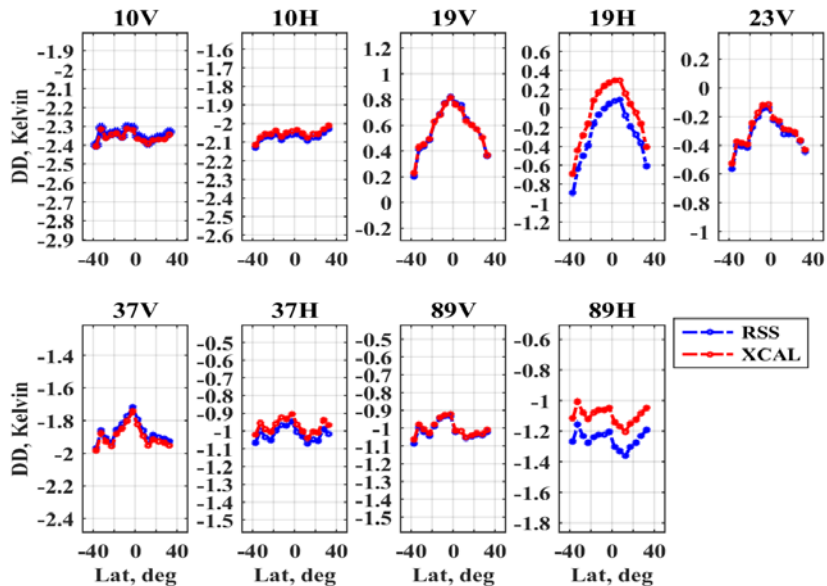


Figure 3-5 *DD* from GMI & TMI inter-calibration stratified by latitude, blue line represents *DD* calculated using RSS RTM, and red line is XCAL RTM.

On the other hand, *DD* results for 19 GHz and 23 GHz show a latitude dependence, which is most likely that the RTM does not accurately represent the theoretical *T_b* for water vapor that changes symmetrically about the equator. However, the V-pol results show negligible differences for the two surface emissivity models; whereas, results for 19 GHz H-pol have a significant offset of ~ 0.3 K.

When the data are sorted by ascending and descending passes for satellite yaw = 0° (flying forward) and 180° (flying backward) the *DD* results (Figure 3-6) exhibit no sensitivity to the two surface emissivity models. Yet, from Figure 3-5, we recognize that the *DD* biases for some channels are not constant. This illustrates the importance of examining the *DD* biases over all possible combinations of parameters to assure an accurate cross-calibration with GMI.

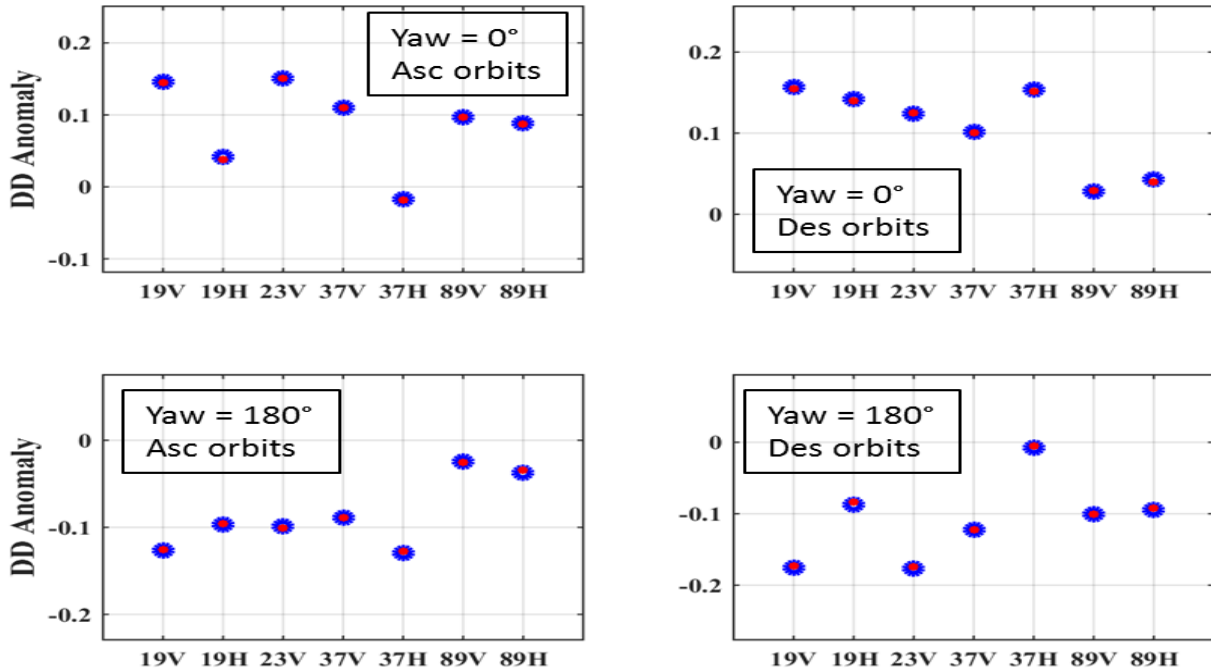


Figure 3-6 *DD* anomaly for GMI & SSMIS-F17 with yaw = 0°/180° and asc/des orbits. Blue color represents that using RSS RTM, and red color is XCAL RTM.

In addition, the reason for the sensitivity of the *DD* biases (for certain channels) to the RTM is examined in Figure 3-7. Here the difference of the *DD* biases (triple difference) for the two RTM's are plotted versus the ocean surface wind speed. Since the ocean wind speed follows a Rayleigh distribution with mean ~ 6.5 m/s, the *DD* result is effectively the average over wind speed between 3 – 10 m/s. Over this range, the triple difference for most channels is close to zero, except for 19 GHz H-pol, 23 GHz and 89 GHz H-pol. For these channels, differences in the emissivity model responses to wind speed cause significant changes, which are RTM dependent.

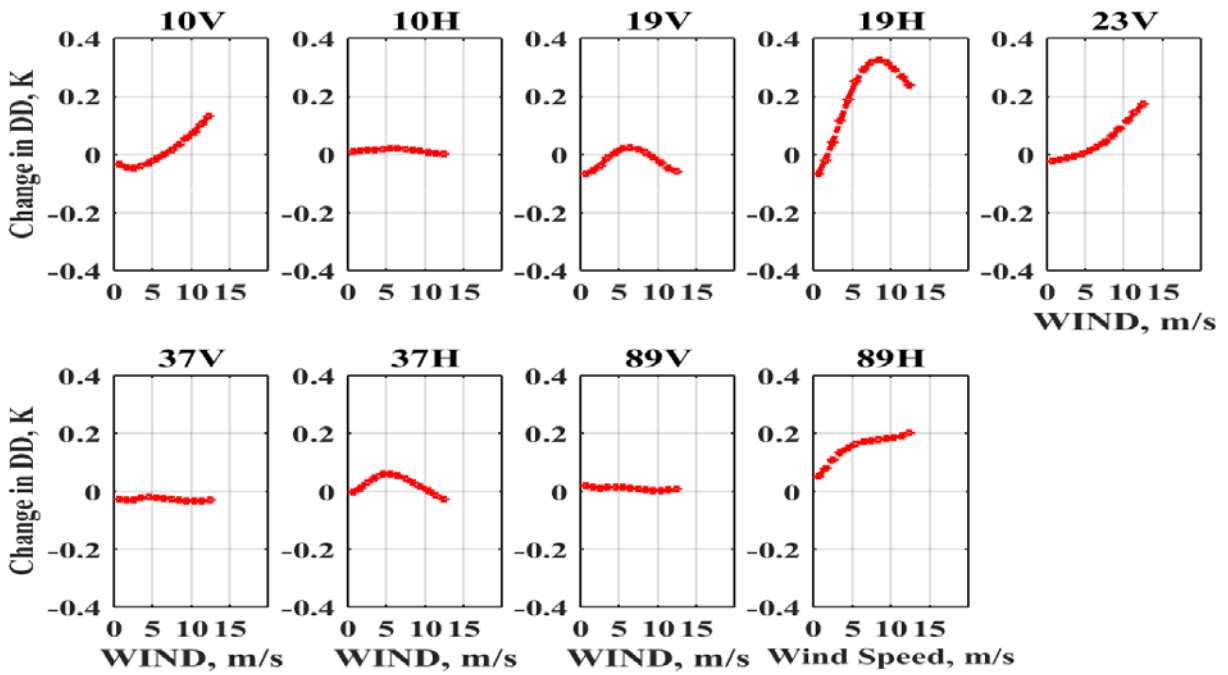


Figure 3-7 Triple difference between the *DD* values from GMI and TMI for XCAL and RSS RTM's by channel.

Finally, the overall box average *DD* biases (relative to GMI) are tabulated for 7 constellation satellites, 9 channels and the two RTM's in Table 3-3. Of the 53 combinations, the triple differences are excellent for all but 13 marked in red color, and these are associated with 19 GHz H-pol and 89 GHz H-pol discussed above.

Table 3-3 Mean and std of double differences.

	TMI	WindSat	AMSR2	SSMIS-F16	SSMIS-F17	SSMIS-F18	SSMIS-F19
10V	-2.34/-2.35	-1.17/-1.14	3.22/3.20	N/A	N/A	N/A	N/A
10H	-2.07/-2.05	-0.71/-0.65	2.84/2.90	N/A	N/A	N/A	N/A
19V	0.57/0.57	0.67/0.71	3.86/3.83	0.08/0.06	-0.07/-0.07	0.19/0.18	0.53/0.52
19H	-0.29/-0.07	1.95/1.86	1.76/1.94	-0.72/-0.96	-0.90/-1.1	-0.52/-0.75	1.77/1.56
23V	-0.32/-0.30	0.88/0.90	3.16/3.03	-0.89/-0.88	-1.04/-1.06	-0.83/-0.81	1.23/1.24
37V	-1.87/-1.89	1.17/1.45	2.07/2.03	-1.78/-1.76	-1.82/-1.80	-1.69/-1.68	-0.09/-0.07
37H	-1.02/-0.98	1.09/1.46	3.67/3.82	-1.05/-1.09	-0.96/-1.00	-0.95/-1.00	1.97/1.91
89V	-1.01/-1.00	N/A	0.57/0.45	-0.80/-0.75	-0.99/-0.94	-1.10/-1.05	-1.68/-1.64
89H	-1.25/-1.10	N/A	1.45/1.33	-1.44/-1.23	-1.34/-1.13	-1.53/-1.33	-0.56/-0.38

While these models yield different Tb 's of several Kelvin, the Tb bias results are nearly identical, which shows the robustness of this XCAL technique. The anomaly presenting in 19 GHz H-pol and 89 GHz H-pol was investigated and explained by significant differences in the emissivity models for these two channels. For most of the comparisons (satellites and channels), it is apparent that the DD biases from both the XCAL and RSS RTM's are nearly identical (< 0.1 K); indicating that the CFRSL XCAL algorithm is not sensitive to the choice of RTM. However, for the 19 GHz H-pol and 89 GHz H-pol significant differences were noted. After independent investigations of the XCAL working group, the RSS model was selected as the surface emissivity model.

4 THREE-WAY INTER-SATELLITE RADIOMETRIC CALIBRATION BETWEEN GMI, TMI AND WINDSAT

The TRMM satellite launched in late November 1997 into a low earth orbit, produced the longest satellite-derived precipitation time series of 17 years. During the second half of this mission, a collection of cooperative weather satellites, with microwave radiometers, were combined to produce a 6-hour tropical precipitation product, and the TRMM Microwave Imager (TMI) was used as the radiometric transfer standard to inter-calibrate the constellation members. To continue this valuable precipitation climate data record, the Global Precipitation Mission (GPM) observatory was launched in February 2014; and the GMI became the new transfer standard that normalized the microwave radiance measurements of the GPM constellation radiometers. Because the radiometric transfer standard for this constellation has changed to GMI, it is highly desirable to perform XCAL between GMI and TMI to link the TRMM and GPM precipitation measurements to form a multi-decadal climate dataset.

Intercomparisons between TMI and the Naval Research Laboratory's WindSat polarimetric radiometer over oceans has been conducted, from which the radiometric calibration of TMI relative to WindSat exhibited exceptional long-term radiometric stability over a period > 8 years. Results will be presented in this chapter. Moreover, for purposes of assessing global climate change, it is crucial that a seamless transfer between the TRMM and the GPM microwave *Tb* time series be achieved. Therefore, this chapter will also present arguments that the 3-way (WindSat, TMI and GMI) intersatellite radiometric comparisons, performed during the 13-month period overlap, can be used to bridge the TRMM and GPM eras, and assure a stable radiometric

calibration between the diverse constellation's member radiometers. The instrumental parameters of the common channels of these three radiometers are listed in Table 2-1.

4.1 Long-term Radiometric Intercalibration stability of TMI and WindSat

The contents of this section have been published in the following article:

R. Chen, A. Santos-Garcia, S. Farrar, and W. L. Jones, "Assessment of the long-term radiometric calibration stability of the TRMM microwave imager and the WindSat Satellite Radiometers," in 2014 13th Specialist Meeting on Microwave Radiometry and Remote Sensing of the Environment (MicroRad), 2014, pp. 187–191 [20].

Since the initial XCAL meeting 11 years ago, the short-term stability of TMI has been verified by several researches, using complementary approaches [21]. This section focuses on evaluating the long-term stability of inter-satellite radiometric calibration of TMI respect to WindSat. The CFRSL XCAL algorithm described in Chapter 3 is used here to derive the radiometric calibration biases between TMI and WindSat for two one-year periods. The TMI *Tb* product used in this analysis was the previous version 1B11 V7; therefore, the biases are slightly different from the extended analysis over even longer time spans with the most updated TMI *Tb* product, 1B11 V8 [3] (will be discussed in Chapter 6), and this does not conflict with the argument that the TMI is radiometrically stable in long-term with respect to WindSat.

The assumption is that the radiometers are stable, thus, the biases should be independent of time. This is verified by comparing monthly collocations over the two one-year periods (XCAL year and CY 2011). When the biases are correlated with any of the instruments, orbital or

environmental parameters, the radiometer calibration is considered flawed and must be corrected to eliminate the systematic trends, before the inter-satellite calibration is performed. The CFRSL has participated in the radiometric calibration campaign of WindSat since its launch, and excellent results have been published to provide high confidence in WindSat’s Brightness Temperature Sensor Data Records (SDR) [6, 7].

Two independent inter-comparisons over oceans for the XCAL year and 2011 are calculated and displayed in Table 4-1 (V-pol) and Table 4-2 (H-pol). The mean and standard deviation of the *Tb* biases of TMI with respect to WindSat are given, along with the mean oceanic *Tb* of TMI at which they were observed. Also shown are the changes of the yearly averaged biases between XCAL year and 2011.

It’s surprising and encouraging to see that the radiometric biases of these two one-year periods, separated by more than a five-year interval, are almost identical. Except 19 H- and V-pol, the changes between the two periods of all the channels are much smaller than 0.1 K, which is the goal of the CFRSL XCAL algorithm. Even in the worst case, 19 H-pol, the change 0.18 K is acceptable for GPM calibration purposes.

Table 4-1 DD mean and std between TMI and WindSat for V-pol.

	Mean (K)	Std. (K)	Change in Mean (K)	@ <i>Tb</i> (K)
10 V	0.33 / 0.34	0.30 / 0.32	0.01	170 / 170
19 V	-0.50 / -0.35	0.59 / 0.61	0.15	199 / 200
22 V	-1.61 / -1.56	0.66 / 0.65	0.05	219 / 220
37 V	-3.188 / -3.185	0.583 / 0.585	0.003	214 / 214

Numbers before and after “/” represent XCAL year and 2011, respectively

Table 4-2 *DD* mean and std between TMI and WindSat for H-pol.

	Mean (K)	Std. (K)	Change in Mean (K)	@ <i>Tb</i> (K)
10 H	-1.564 / -1.559	0.37 / 0.39	0.005	88 / 89
19 H	-2.78 / -2.60	0.8189/0.8190	0.18	132 / 133
37 H	-2.50 / -2.52	0.91 / 0.92	-0.02	152 / 153

Numbers before and after “/” represent XCAL year and 2011, respectively

The *DD* biases for each channel were sorted in various ways to assure that no systematic dependency existed (e.g., by month (seasonal), time of day (day/night), with latitude, and ascending/descending segments of the orbit). Thus, finding no such effects, results presented in Figure 4-1 compare the monthly average bias time-series between XCAL year and 2011, for both V- and H-pol channels at 10 and 37 GHz. Since 10 and 37 GHz are the least and most atmosphere-affected frequencies, respectively, the comparisons of the monthly *DD* between the two periods are representative of all channels. The results are remarked similar in that monthly *DD* between XCAL year (red) and 2011 (blue) in 10 V- and H-pol are nearly equal.

Figure 4-2 shows the monthly *DD* of ascending passes for both XCAL year (red) and 2011 (blue) by channels. Similar to Figure 4-1, the *DD* between these two periods match very well in all the channels except that 19 V- and H-pol channels that have relatively larger changes. However, the changes are still less than 0.2 K, which is quite acceptable. Also, the same patterns of the monthly *DD* are seen in descending passes.

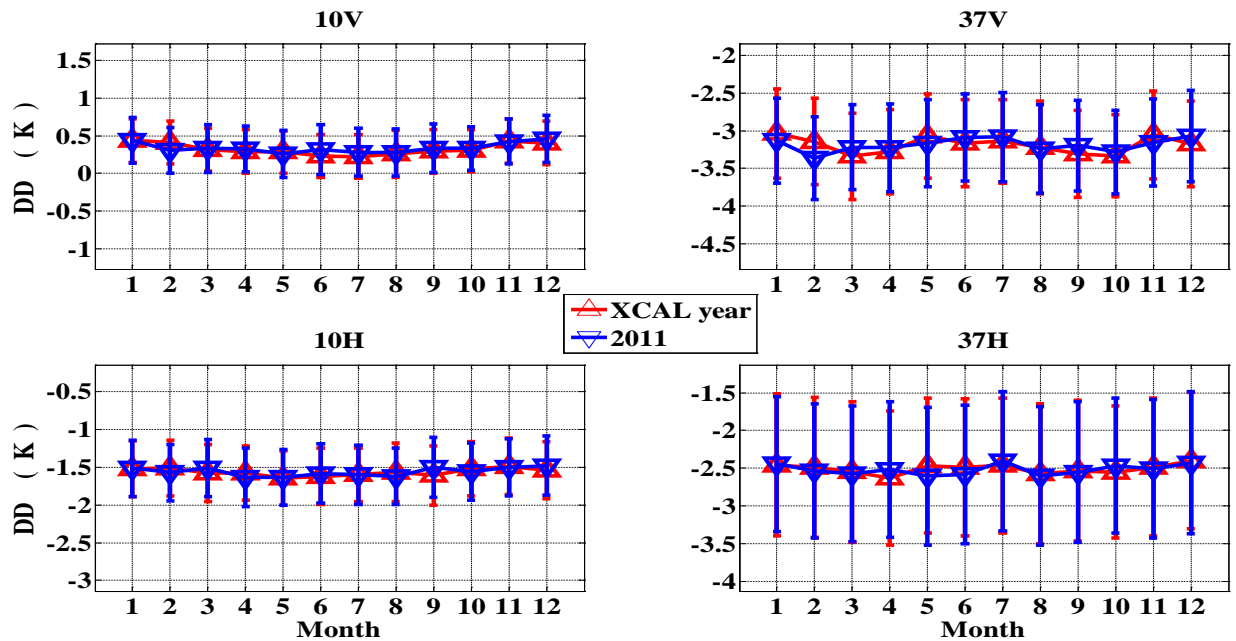


Figure 4-1 Monthly average TMI-WindSat double difference bias time-series at 10 V-, 10 H, 37 V- and 37 H-pol channels, for XCAL year and 2011.

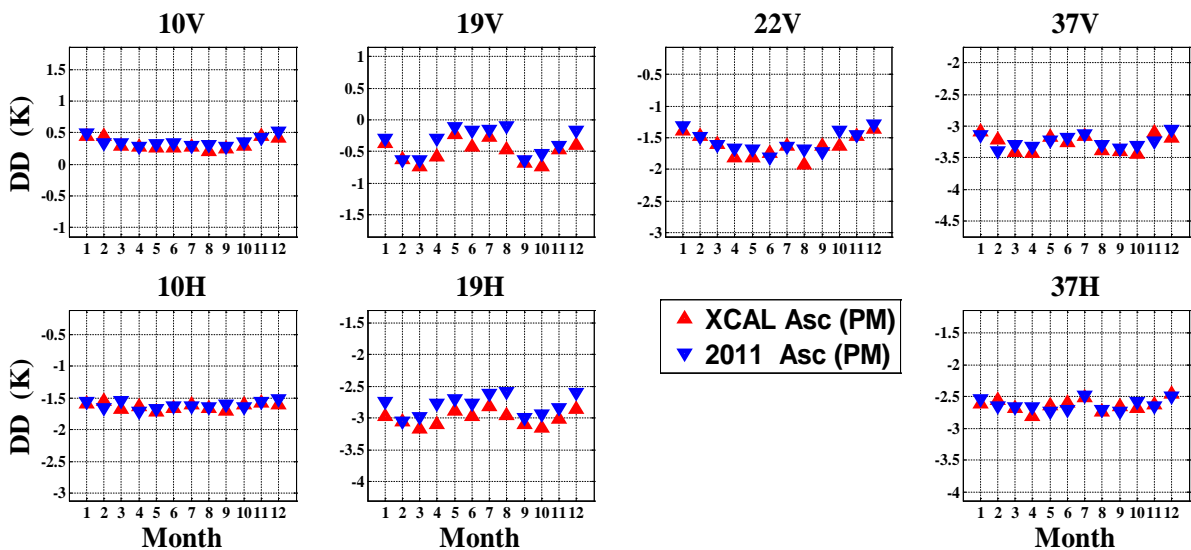


Figure 4-2 Monthly average TMI-WindSat double difference bias of ascending passes at all channels, for XCAL year and 2011.

At both north and south hemispheres, the monthly *DD*'s of ascending and descending passes also show very good consistency between the XCAL year and 2011. In Figure 4-3, the top panel shows the *DD* of ascending passes through north hemisphere at 10 V-pol channel. The variation range of this case is around 0.2 K which is quite satisfactory. Moreover, the bottom panel shows that the monthly *DD* of descending passes at 10 V-pol channel are nearly equivalent between the two periods as well. The *DD*'s of ascending and descending passes in the south hemisphere present similar results, which further verifies the long-term consistency of the inter-satellite radiometric calibration between TMI and WindSat.

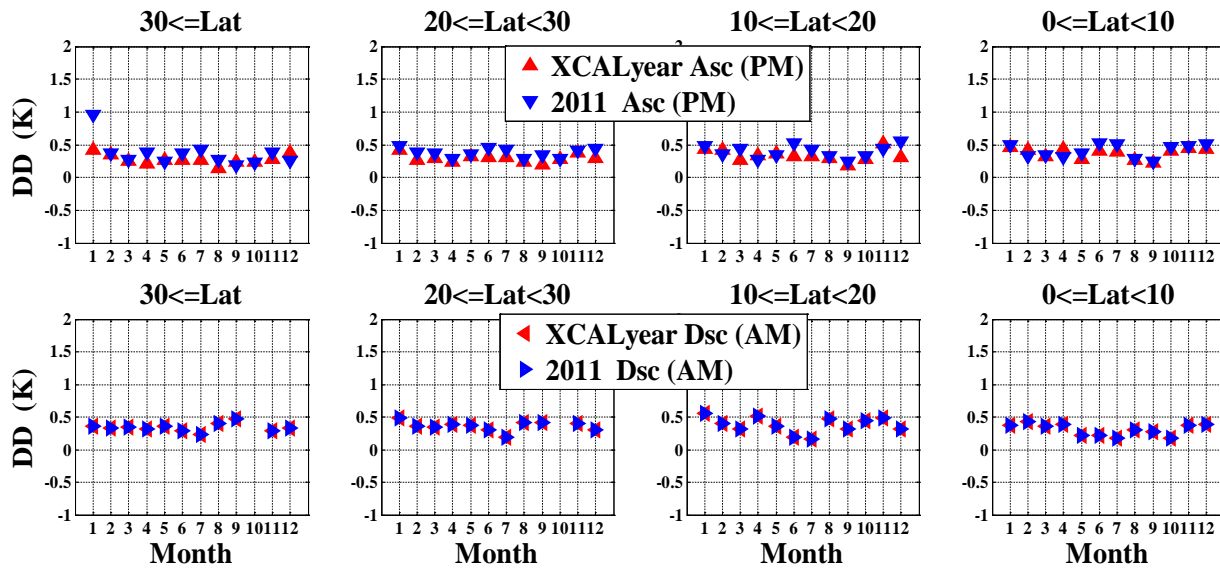


Figure 4-3 Monthly average TMI-WindSat double difference of asc.(top) & dsc. (bottom) passes, through north hemisphere, at 10 V, for XCAL year and 2011.

In conclusion, this section focuses on evaluating the long-term stability of the inter-satellite radiometric calibration, between TMI and WindSat, derived from data collected during the XCAL year and 2011. The *T_b* biases between corresponding radiometers channels, are analyzed by: months, ascending/descending passes and latitude-based geolocation. These two one-year periods

are separated by more than five years, which is very significant for evaluating the long-term consistency of TMI relative to WindSat.

The best case (10 V-pol) has an average change 0.01 K between these two periods, and this is much better than the XCAL goal of 0.1 K. The change of the worst case (19 H-pol), 0.18 K, is slightly larger than the goal but still quite acceptable. The comparison of monthly *DD* for TMI with respect to WindSat, between these two periods, reveals that the relative long-term stability of these two radiometers is excellent. Further, the biases are random errors that exhibit no systematic dependence on any orbital or instrument parameter.

In addition, because of the excellent stability of these two data sets, separated by a period greater than 5 years on orbit, these results also validate the long-term consistency of the CFRSL XCAL algorithm to provide a very stable transfer standard (e.g. TMI or GMI) for calibration of the precipitation measuring constellation of satellite radiometers.

4.2 Three-way Intercalibration between TMI, GMI and WindSat

The contents of this section have been published in the following article:

R. Chen, H. Ebrahimi, and W. Linwood, "Three-way inter-satellite radiometric calibration between GMI, TMI and WindSat," in 2016 IEEE International Geoscience and Remote Sensing Symposium (IGARSS), 2016, pp. 2036–2039 [22].

Because the radiometric transfer standard for the GPM constellation has changed to GMI, it is highly desirable to perform XCAL between GMI and TMI to link the TRMM and GPM precipitation measurements to form a multi-decadal climate dataset. Since TRMM and GPM operated together during a 13-month overlap period, it is possible to perform an inter-satellite

radiometric calibration; however, this activity raises the concern about the stability of this XCAL over the 17-years lifetime of TMI. Fortunately, the WindSat radiometer has existed since January 2003 and continues today; so it can provide additional XCAL with both TMI and GMI, which mitigates the long-term radiometric calibration stability issue. The purpose of this section is to extend the previous radiometric analysis between two radiometers to three radiometers, and presents a 3-way intersatellite radiometric calibration between GMI, TMI and WindSat over oceans during their 13-month of mission operations overlap (March 2014 – March 2015). This work has been published [22], and the analysis based on the latest versions of GMI V05A and TMI *Tb* 1B11 V8 product is exhibited in this section.

First, the gridding process described in Section 2.1.1 is applied to the *Tb*'s of each radiometer, where conservative filters (based upon mean values and standard deviations) are applied to exclude non-homogeneous ocean scenes (e.g., islands and weather fronts/precipitation) and other data quality issues.

Second, the gridded *Tb*'s of the three radiometers are collocated in ± 1 or ± 2 -hour time window along with the geophysical parameters from GDAS. The typical coverage provided by a single orbit from each of the three sensors on May 21, 2014 is shown in Figure 4-4, and one area of triple collocations is expanded in this image. Over the 13 months of XCAL, there are approximately 33,300 boxes available for analysis.

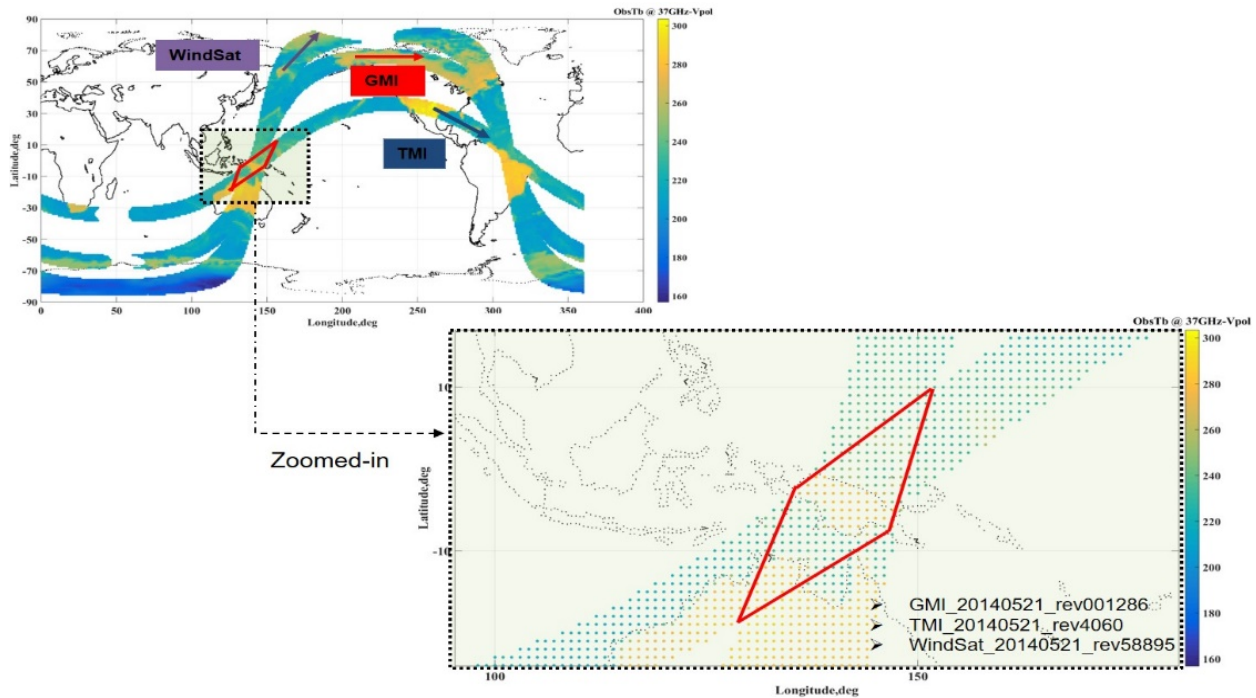


Figure 4-4 Example of near-simultaneous orbits (May 21, 2014) from GMI, TMI and WindSat on a global map (upper panel), with 3-way collocated $1^\circ \times 1^\circ$ boxes within ± 2 -hour shown in the expanded image (lower panel).

Next, theoretical (simulated) brightness temperatures, Tb_{sim} , for each radiometer are calculated using the XCAL RTM with the collocated geophysical parameters from GDAS as inputs.

Finally, the *DD* technique described in Section 3.4 is used to calculate the calibration bias between each pair of radiometers, i.e., TMI to GMI, WindSat to GMI, and TMI to WindSat. Note that for each two-way comparison, the former is the target radiometer and the latter is the reference.

After all boxes have been processed, the data are stratified into various categories to examine for systematic trends in the biases. For example, calibration biases are sorted monthly, as a function of latitude, and as a function of scene Tb .

Figure 4-5 shows that the collocated boxes for all channels within a time-window of ± 2 hours are approximately uniformly distributed between $\pm 40^\circ$ latitude (limited by the TRMM orbit). The upper left panel in Figure 4-5 displays the collocated boxes, with the color scale representing the number of boxes. The other 3 panels show the corresponding 3-way 37GHz V-pol *DD*'s plotted in color for TMI/WindSat, WindSat/GMI, and TMI/GMI.

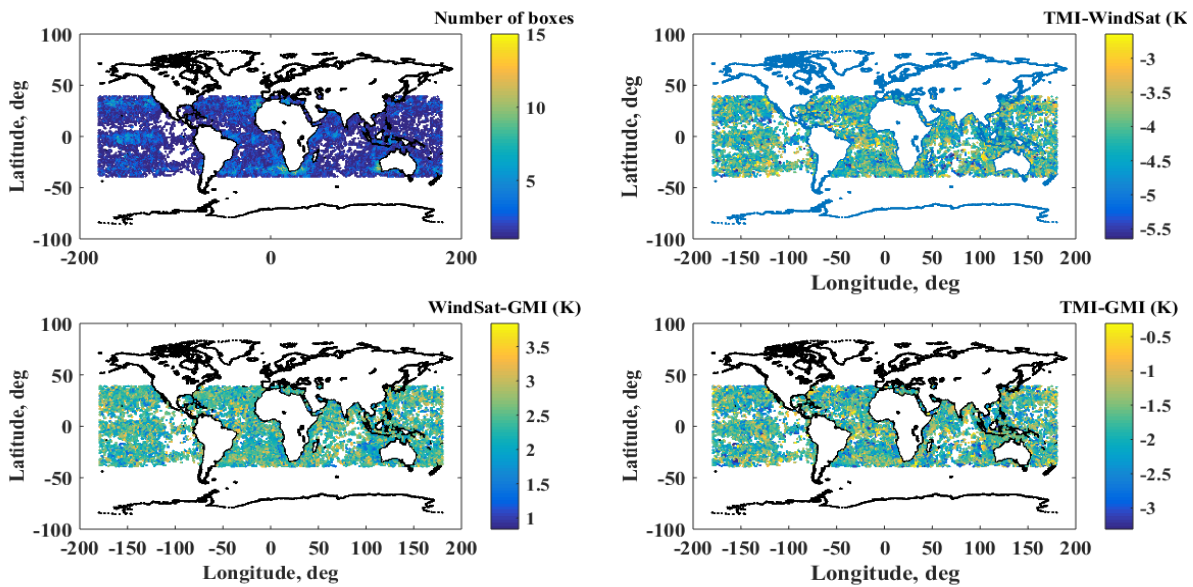


Figure 4-5 Distribution of 3-way collocations for GMI, TMI and WindSat over oceans, within ± 2 -hour time-window for the over-lap period of March 2014-March 2015. Upper left-hand panel presents the collocations, and the color scale represents the number. The upper right-hand panel represents TMI/WindSat *DD* biases, the lower panels are the WindSat/GMI and the TMI/GMI *DD* biases (left to right), and the color bar on the right side of each panel indicates the value of bias.

Our analysis shows that the histograms of the *DD*'s for all radiometers and for all channels are Gaussian, and the corresponding mean *DD* biases (μ) and standard deviations (std, σ) of the 3-way XCAL are tabulated in Table 4-3 for two different temporal collocation windows. The upper panel shows the μ and σ for ± 1 hr and the lower panel for ± 2 hr. Comparing the two temporal

window panels, 86% of the mean values have a difference ($\Delta = | \pm 2 \text{ hr} - \pm 1 \text{ hr} |$) $< 0.1 \text{ K}$ and 14% have a difference $< 0.2 \text{ K}$. Moreover, 76% of the std differences are $< 0.1 \text{ K}$, and the remainder are $\leq 0.25 \text{ K}$. In both panels of Table 4-3, the H-pol results have higher variation than V-pol for all the three sets of *DD*'s; where the greatest stability occurs in the 10V channel and the most variability occurs in 19H and 37H channels. The observed stable performance of the dataset justifies using $\pm 2 \text{ hr}$ for the *DD* comparisons that follow.

Table 4-3 Double differences mean/std, upper panel is $\pm 1 \text{ hr}$ and lower panel is $\pm 2 \text{ hr}$ temporal resolution.

	10V	10H	19V	19H	23V	37V	37H
TMI-WS	1.04/0.33	1.15/0.31	-1.36/0.47	-1.46/0.63	-1.70/0.60	-2.29/0.42	-0.43/0.68
WS-GMI	-0.38/0.20	-0.57/0.23	1.37/0.34	2.09/0.55	1.68/0.40	1.41/0.31	1.53/0.54
TMI-GMI	0.66/0.30	0.58/0.31	0.01/0.46	0.64/0.61	-0.01/0.55	-0.88/0.41	1.10/0.64
TMI-WS	1.04/0.35	1.16/0.35	-1.33/0.53	-1.44/0.76	-1.70/0.73	-2.29/0.51	-0.40/0.87
WS-GMI	-0.35/0.22	-0.57/0.30	1.39/0.41	2.12/0.71	1.74/0.54	1.44/0.41	1.54/0.74
TMI-GMI	0.69/0.32	0.59/0.36	0.06/0.52	0.68/0.75	0.03/0.68	-0.85/0.52	1.14/0.87

Results presented in Figure 4-6 show that the monthly averaged values of *DD* radiometric bias are remarkably stable over the entire 13-month period. However, as seen from the various channels, there are significant biases between instruments. Regardless, these mean biases are not an issue because GMI is the standard for the *Tb* calibration, and these offsets will be applied to transform the various radiometer *Tb*'s to be equivalent to GMI.

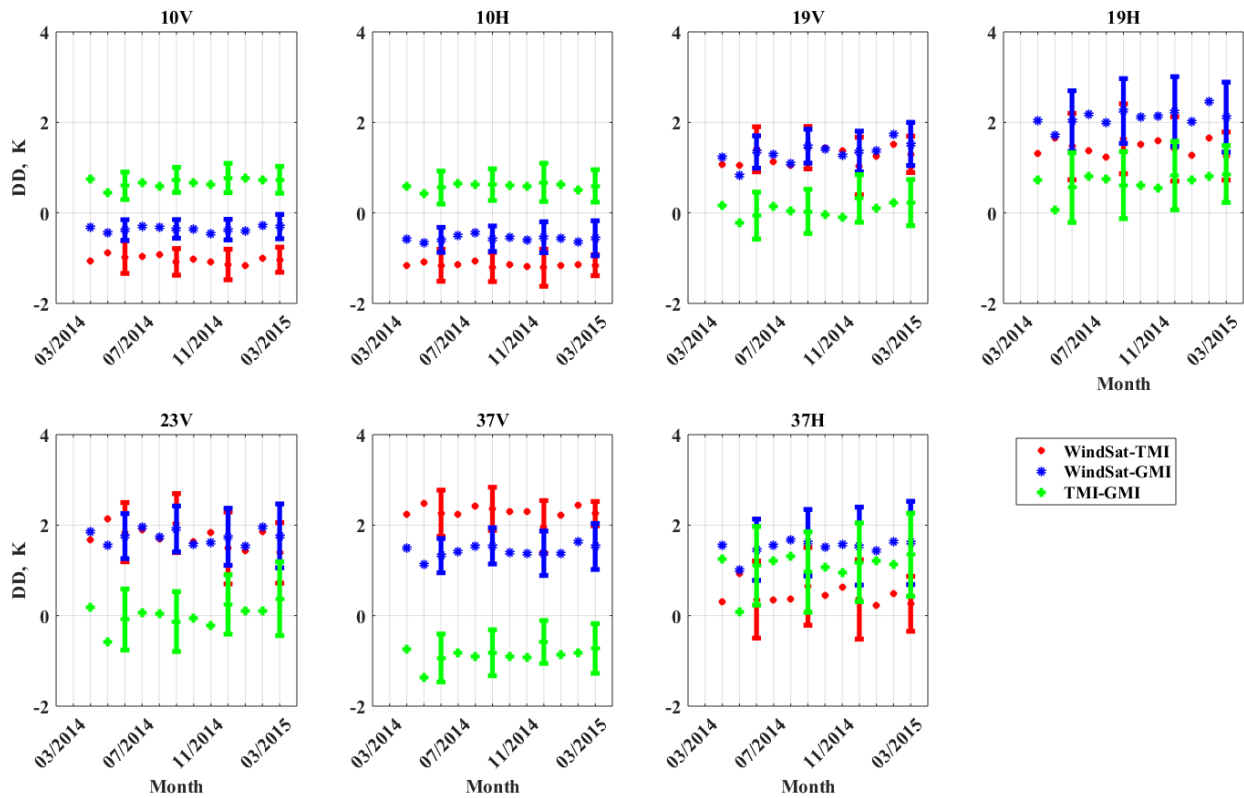


Figure 4-6 Monthly DD of 3-way inter-calibration among GMI, TMI and WindSat by radiometer channel.

Another comparison is shown in Figure 4-7, where the DD 's are stratified by latitude, and again these results show negligible dependency on geographical location. However, note that the lowest variation occurs at 10 GHz and the highest at 19H and 37H channels, which is probably related to the DD sensitivity to the variable atmospheric conditions over the 13-month period.

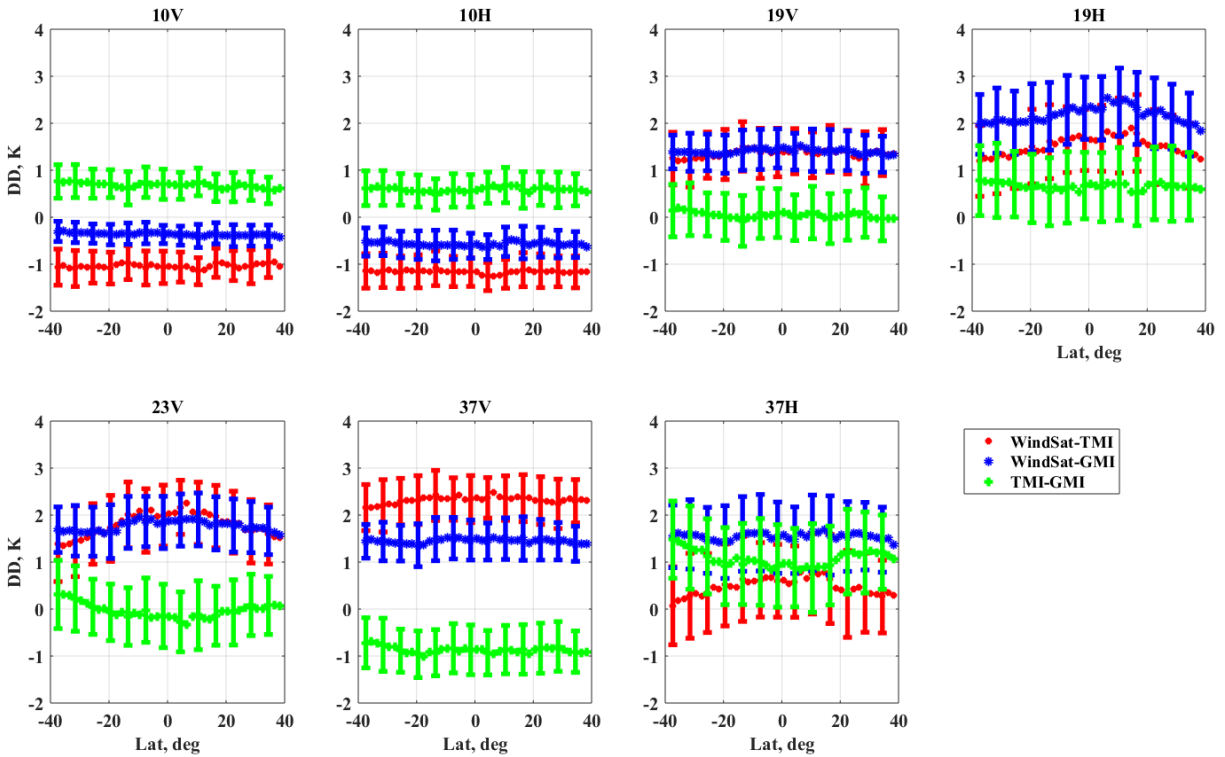


Figure 4-7 Zonal stratification of radiometer channel *DD*'s for the overlap period.

Next, to examine the radiometer calibration linearity, the *DD* bias anomalies (means subtracted) are plotted against the corresponding reference radiometer *Tb* in Figure 4-8. As it was mentioned previously, it is desirable that the *DD* biases be constant regardless of the manner of comparison; and for most channels, the results are stable indicating that there are no systematic effects. However, for the 19H and 23V channels, the plots have a slight linear dependence, where the worst case slope (< 0.03 K/K) occurs for the 19H GMI/TMI comparison. After considerable investigation, we do not believe that this is caused by radiometer non-linearity.

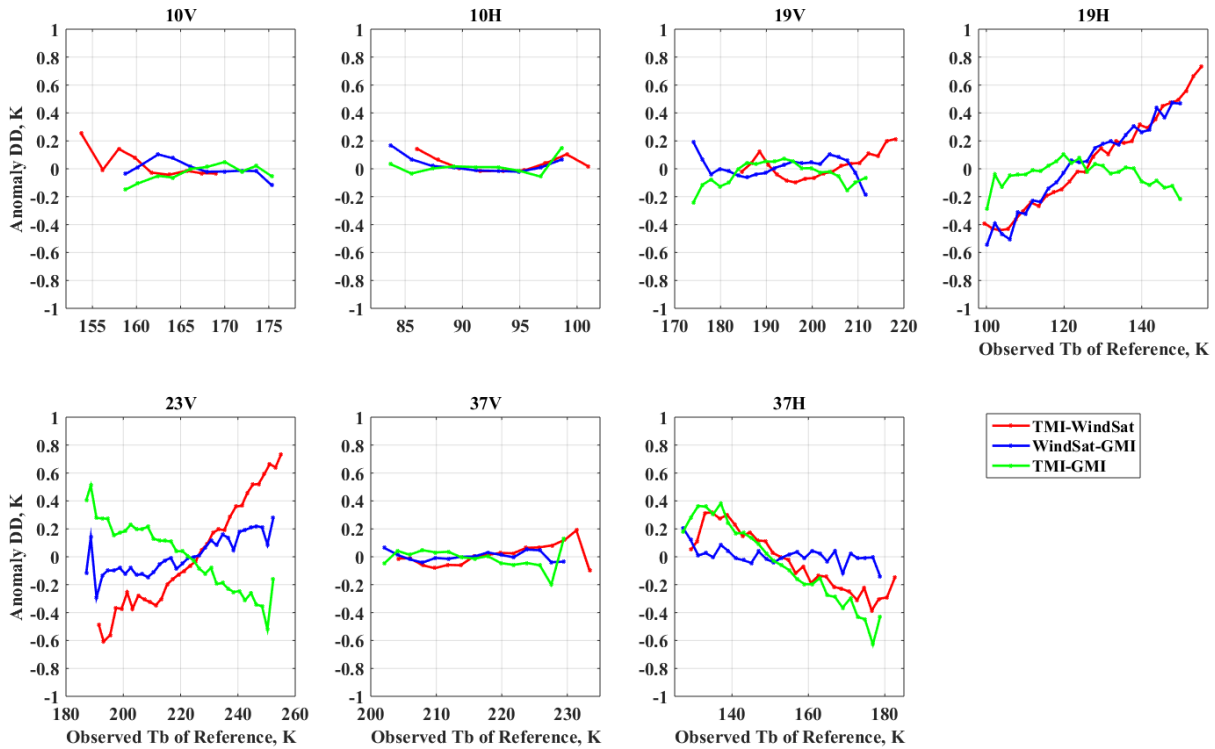


Figure 4-8 Radiometer channel bias anomalies ($DD - \text{mean-}DD$) stratified by the average scene Tb_{obs} for the reference radiometer, which is WindSat for TMI & WindSat, and GMI for the other two radiometer comparisons.

To validate this (Figure 4-8), the same DD bias anomalies are stratified by GDAS surface wind speed in Figure 4-9. For these analyses, the cross-calibration comparisons were conducted using two different ocean surface emissivity models (not shown). The results are nearly constant over the entire wind speed range for each channel. Moreover, for these channels, there is a significant atmospheric Tb component that is proportional to the integrated water vapor density. Thus, we suspect this scene dependent effect is a residual error associated with imperfect radiative transfer modeling of the water vapor resonance near 22.22 GHz, which is used in the CFRSL XCAL algorithm.

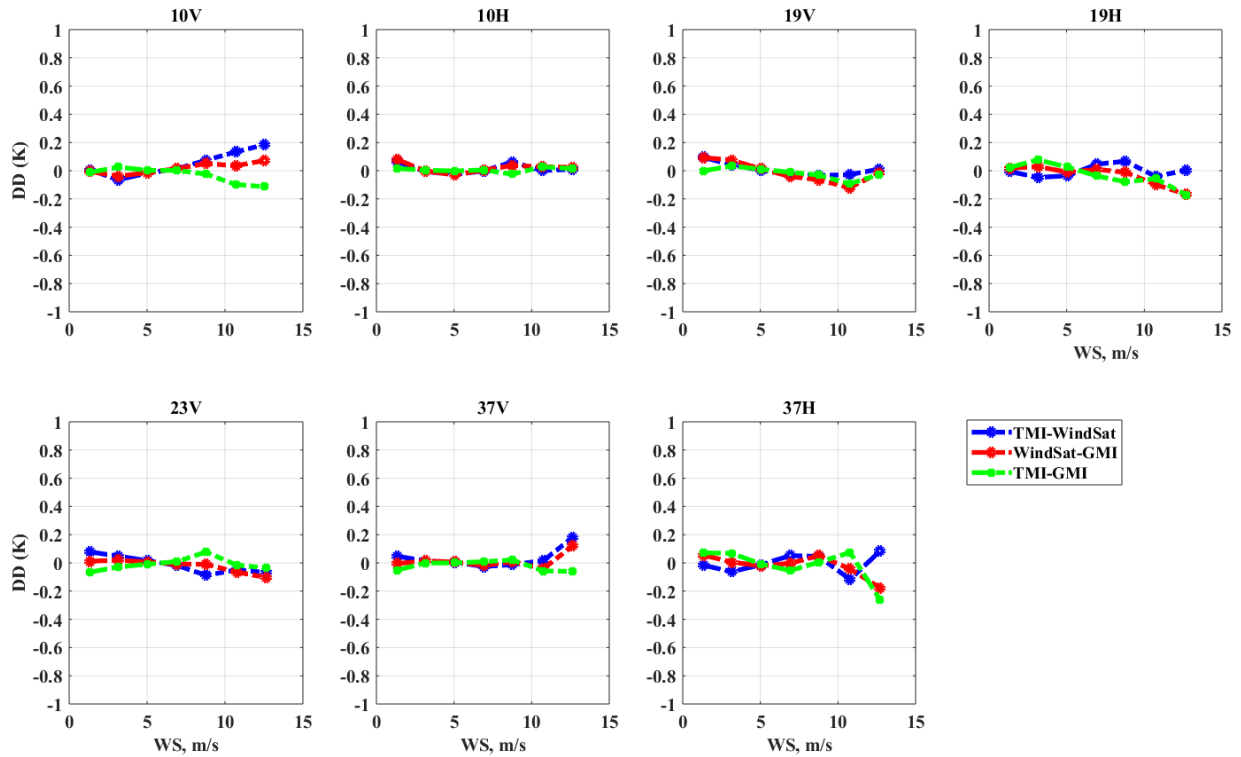


Figure 4-9 Radiometer channel bias anomalies ($DD - \text{mean-}DD$) stratified by GDAS ocean surface wind speed for the overlap period.

During this study, DD biases and anomalies between TMI/WindSat, WindSat/GMI and TMI/GMI are characterized on a channel (frequency and polarization) basis for the 13-month overlap period, and the results are stable with small uncertainties (typically $< \pm 0.1$ K). These 3-way collocations are uniformly distributed (spatial and temporal), and the resulting Tb DD 's, produced on individual collocated boxes, have Gaussian distributions with almost no perceived systematic effects. Thus, we believe that the histogram means are excellent estimates of the channel radiometric Tb bias, which is consistent with the GPM goal for intersatellite radiometric calibration. Moreover, it is important to note that the objective is to provide a good relative calibration between constellation radiometers, as opposed to an absolute Tb calibration. While the

latter is a desirable goal, we are fortunate to have GMI that appears to be extremely well calibrated and stable, which makes it an excellent calibration reference to produce the entire combined TRMM-GPM datasets and to provide the opportunity to create a consistent long-term data record [5].

Further, WindSat, which overlaps with both TMI (past) and GMI (future) will provide a much longer time series for intersatellite calibration, supporting the approach of using WindSat as the radiometric transfer standard to bridge the TRMM and GPM eras. Thus, the concern of calibration drift between GMI and TMI can be effectively mitigated by performing frequent intersatellite comparisons using WindSat to remove any long-term changes, should they exist.

Furthermore, we acknowledge that the cloud liquid water (CLW) is not well represented in GDAS numerical weather model used, and this can play a role in the RTM simulated Tb 's for the high-frequency channels. However, in a large part, this effect is mitigated by using the double difference to remove the common-mode sources of radiometric biases in the two channels considered. Moreover, future work will use microwave retrievals of CLW to evaluate its impact on DD bias and to develop more effective filters, if needed.

5 UNCERTAINTY QUANTIFICATION MODEL

While the CFRSL XCAL algorithm yields that the *Tb* bias after the composite XCAL offsets can be applied to the TMI 17-plus-year legacy *Tb* product, however, this is not an absolute bias. The RTM and input geophysical parameters are not perfect, hence the uncertainties due to these sources remain. In addition, the microwave sensors are with tens of kilometer resolution, the sampling process thus is subject to variability in both time and space, and further contribute to the *Tb* bias uncertainty. Therefore, it is necessary to quantify the uncertainty estimates considering all the uncertainty sources aforementioned and more, and to include them with the *Tb* bias for deriving science products into perspective.

A generic uncertainty quantification model (UQM) is developed herein, and the procedural steps involved are summarized as follows:

- 1) Identify sources of uncertainty.
- 2) Quantify uncertainty components: determine the standard uncertainty associated with each of the input quantities, including any uncertainty associated with the correction for systematic error.
- 3) Calculate the combined standard uncertainty from individual uncertainty.
- 4) Calculate the expanded uncertainty of the *Tb* bias by applying an appropriate coverage factor if needed.

The diagram of this model is shown in detail in Figure 5-1, and explicit explanations are provided subsequently.

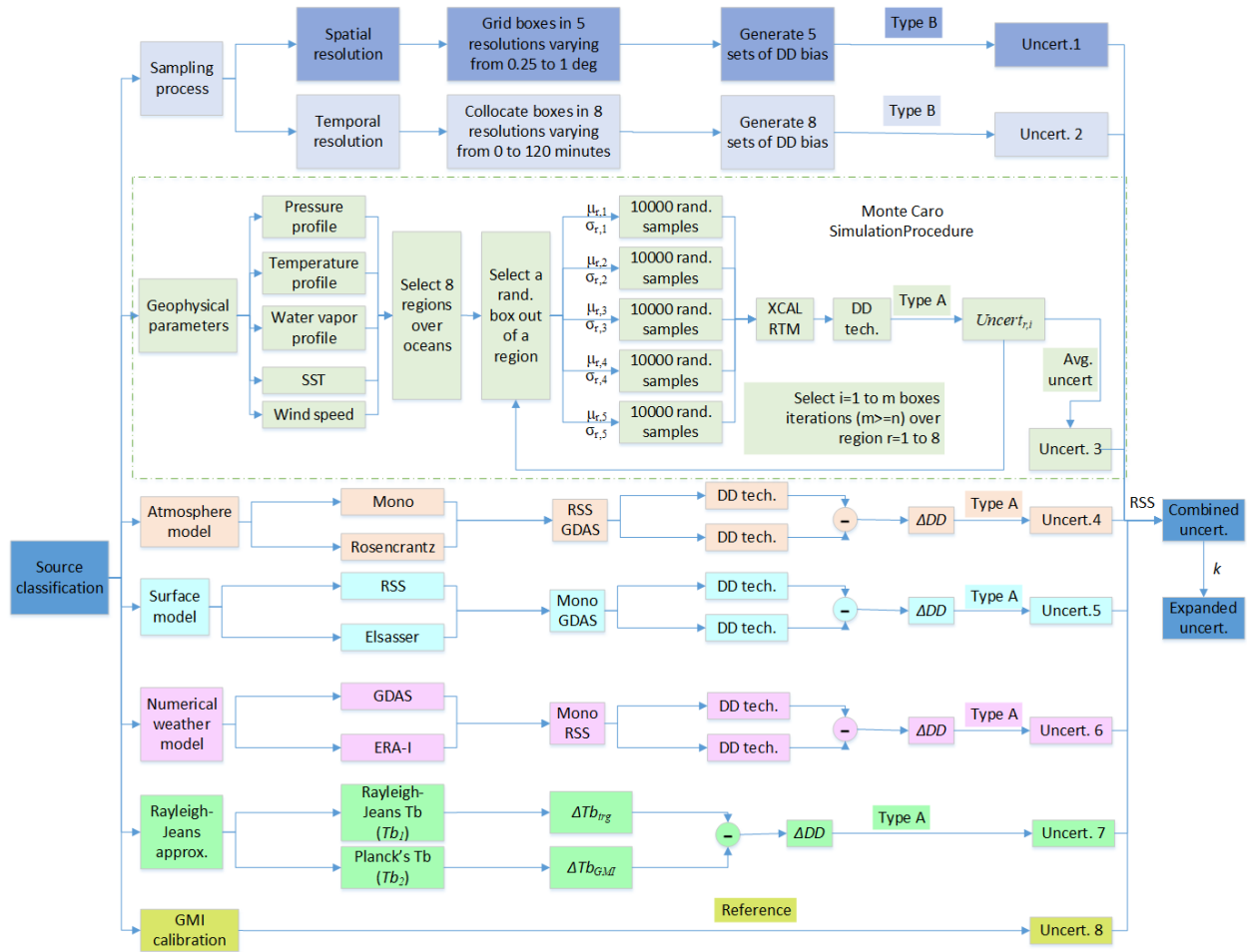


Figure 5-1 Diagram of Uncertainty Quantification Model.

5.1 Uncertainty and Error

Before proceeding to the uncertainty estimates classification and quantification, it needs to be noted that the uncertainty in Tb is different from the Tb error. By definition, the term error is the difference between the true bias and the estimated bias. The most likely or “true” value may thus be considered as the estimated value including a statement of uncertainty which characterizes the dispersion of possible measured values. Uncertainty is caused by the interplay of errors which create dispersion around the estimated bias; the smaller the dispersion, the smaller the uncertainty

[23]. The uncertainty to-be-derived in this dissertation is used with a \pm symbol following the Tb bias reported to the NASA PPS, indicating the uncertainty associated with the estimated Tb bias and not the error. The uncertainty of the Tb bias reflects the lack of exact knowledge of the bias due to various possible sources of uncertainty which will be discussed in Section 5.2. The following terminologies defined by [23] are used in this dissertation work:

1) The standard uncertainty is the uncertainty of the results of a measurement expressed as a standard deviation.

2) Any method for evaluation uncertainty using statistical analysis of a series of observations is call Type A evaluation of uncertainty. Any method for evaluation uncertainty by means other than the statistical analysis for a series of observations is call Type B evaluation of uncertainty.

Type A uncertainty estimates is often used in assessing random effects, and the treatment is usually a calculation of the standard deviation (STD)

$$s(v) = \sqrt{\frac{\sum_{i=1}^n (v_i - \bar{v}_n)^2}{n-1}} \quad (3)$$

Type B uncertainty estimation is used in systematic effects, and the treatment is to calculate the standard deviation of n mean bias of repeated experiments divided by square root of n as shown in the following equation

$$s(v_n) = \frac{s(v)}{\sqrt{n}} \quad (4)$$

3) Combined standard uncertainty of estimated Tb bias caused by various uncertainty sources equals to the positive square root of a sum of terms. Combined standard uncertainty may

contain terms whose components are derived from Type A and/ or Type B evaluations without discrimination between types.

5) Coverage factor “k” is a numerical factor used as a multiplier of the combined standard uncertainty in order to obtain an expanded uncertainty. It indicates the number of standard deviations that a particular value may be distant from the mean of the distribution. Most of this dissertation refers to standard uncertainty except in Section 5.4 where the coverage factor is chosen to be $k = 3.0$ which means that approximately 99% of the distribution will lie within three standard deviations of the mean bias.

5.2 Uncertainty Source Classification

Calculating the combined standard uncertainty of the Tb bias requires the evaluation of the standard uncertainty of each uncertainty origin that could possibly result in dispersion estimation bias relative to the true bias. As the accuracy with which the RTM model can predict the true value of Tb is dependent on the accuracies of the input data, boundary conditions and the model itself, the uncertainty sources (shown in Figure 5-2) that are studied here include sampling process, geophysical field variability, various atmospheric absorption models and surface emissivity models, different numerical weather prediction models, approximation from Planck’s Function to Rayleigh Jeans Law and uncertainty in the calibration reference, GMI.

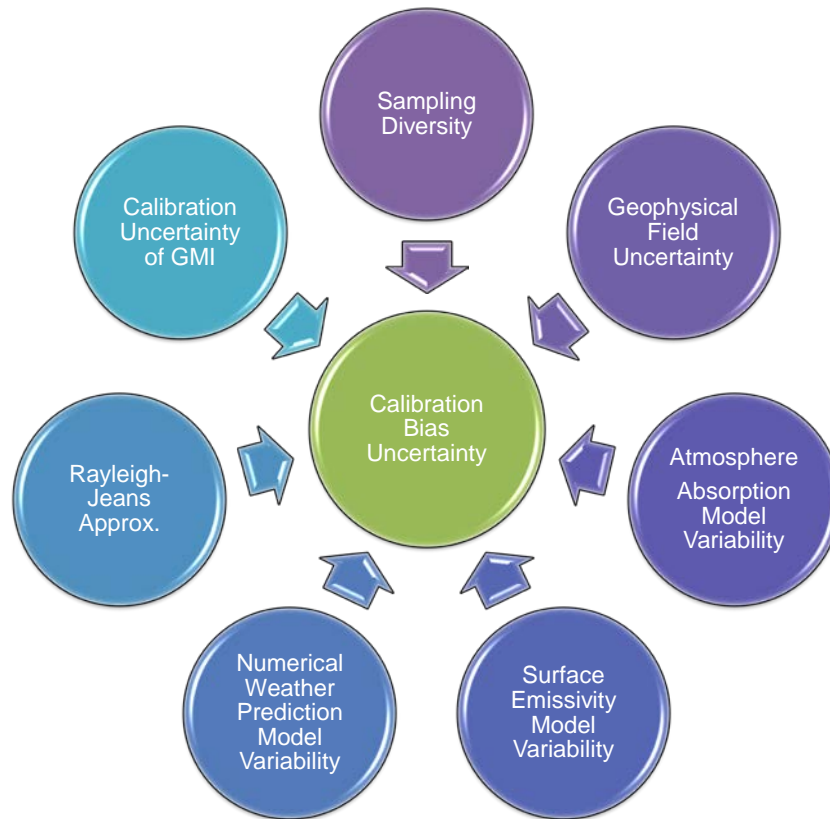


Figure 5-2 Sources that contribute to the calibration bias uncertainty.

5.3 Individual Uncertainty Estimate Quantification

Uncertainty from each source is quantified using different methods. As stated earlier in Section 5.1, methods for evaluating each single uncertainty source are classified as either “Type A” or “Type B”. A Type A evaluation of an uncertainty uses a series of measurements to estimate the standard deviation empirically. Any other method of evaluating is a Type B method. For illustration purposes, the XCAL between GMI and the TMI is used to demonstrate the quantification process.

Sample size determination is the act of choosing a sufficient number of observations to include in the uncertainty estimation model development. The sample size is an important feature

because samples that are too large may waste time and resources, while samples that are too small may lead to inaccurate results. There are two terms that affect the minimum sample size, which are margin of error and confidence level. In this dissertation, we need to determine the minimum sample size needed to estimate the uncertainty of the *Tb* calibration bias within 0.05 K margin of error and with 99% confidence, which is the basis of the UQM.

When sample data is collected and the sample mean \bar{x} is calculated, that sample mean is typically different from the population mean μ . This difference between the sample and population means can be thought of as an error. The margin of error E is the maximum difference between the observed sample mean \bar{x} and the true value of the population mean μ :

$$E \geq z_{\alpha/2} \times \frac{\sigma}{\sqrt{n}} \quad (5)$$

$z_{\alpha/2}$ is known as the critical value, the positive z value that is the vertical boundary for the area of $\frac{\alpha}{2}$ in the right tail of the standard normal distribution, σ is the population standard deviation and n is the sample size. A 99% degree confidence yields $\alpha = 0.01$ and $z_{\alpha/2} = 2.576$.

Therefore, the n value should be:

$$n \geq \left[\frac{z_{\alpha/2} \times \sigma}{E} \right]^2 \quad (6)$$

As TMI/GMI bias standard deviations for all the 9 channels are as follows:

0.28752 0.30585 0.4409 0.57454 0.53027 0.44741 0.67704 0.40266 0.66786,

the minimum sample size n should be 1217, and it should be ensured through the whole development process of the UQM. The number of the minimum sample size varies with UQM

application to other instruments' intercalibration as the mean value and boundary conditions change.

5.3.1 Uncertainty in Sampling Process

The frequently used spatial sampling resolution in the CFRSL XCAL algorithm described in Chapter 3 is 1° latitude/longitude, and temporal resolution is ± 60 minutes. As these resolutions were decided empirically and the *DD* bias would vary slightly when the spatial or temporal resolution changes. Therefore, it is necessary to estimate the uncertainty of *DD* bias caused by the spatial and temporal resolution diversity. In this section, the CFRSL XCAL algorithm is performed with different resolutions spatially and temporally, and the standard uncertainty of sampling process is therefore calculated based upon the multiple sets of calibration biases. The 8 cases of different temporal resolutions are presented in Table 5-1 in which each time window is 15 minutes. For example, Case 1 is the XCAL of TMI and GMI base on their observation time difference larger or equal to 0 and smaller than 15 minutes. The 5 case of spatial resolutions with different latitude/longitude box size are shown in Table 5-2. The minimum spatial resolution is 0.25° latitude \times 0.25° longitude which is about a size of $25 \text{ km} \times 25 \text{ km}$ box. The GMI instantaneous field of view (IFOV) at 10 GHz is 19.4 km along scan by 22.4 km cross track, which is slightly smaller than $0.25^\circ \times 0.25^\circ$ grid cell, therefore, the spatial resolution cannot go below $0.25^\circ \times 0.25^\circ$.

Table 5-1 Temporal resolutions.

Case	1	2	3	4	5	6	7	8
Temporal reso. (min)	[0, 15]	[16, 30]	[31,45]	[46,60]	[61, 75]	[76, 90]	[91, 105]	[106, 120]

Table 5-2 Spatial resolutions.

Case	1	2	3	4	5
Spatial reso. (deg)	1°×1°	0.75°×0.75°	0.5°×0.5°	0.375°×0.375°	0.25°×0.25°

After implementing the XCAL process of TMI and GMI using the above mentioned sampling resolutions, 8 sets of *DD* mean values and STD values are achieved with temporal sampling variation, and 5 sets for spatial variability are obtained with spatial sampling variation. The results per channel are shown in Figure 5-3 and Figure 5-4 where the dots in the middle of each line is the mean *DD* of the corresponding case, and the length of the line is twice of the STD values. Using the treatment of Type B uncertainty estimation (equation (3)), the spatial and temporal standard uncertainty per channel is calculated and shown on the top of each subplot as well as listed in Table 5-3, with the largest value is as small as 0.016 K. This indicates the insignificant impact of the sampling process variability on the *DD* bias derived by the CFRSL XCAL algorithm, but it does not mean that it should not be taken into account in the UQM.

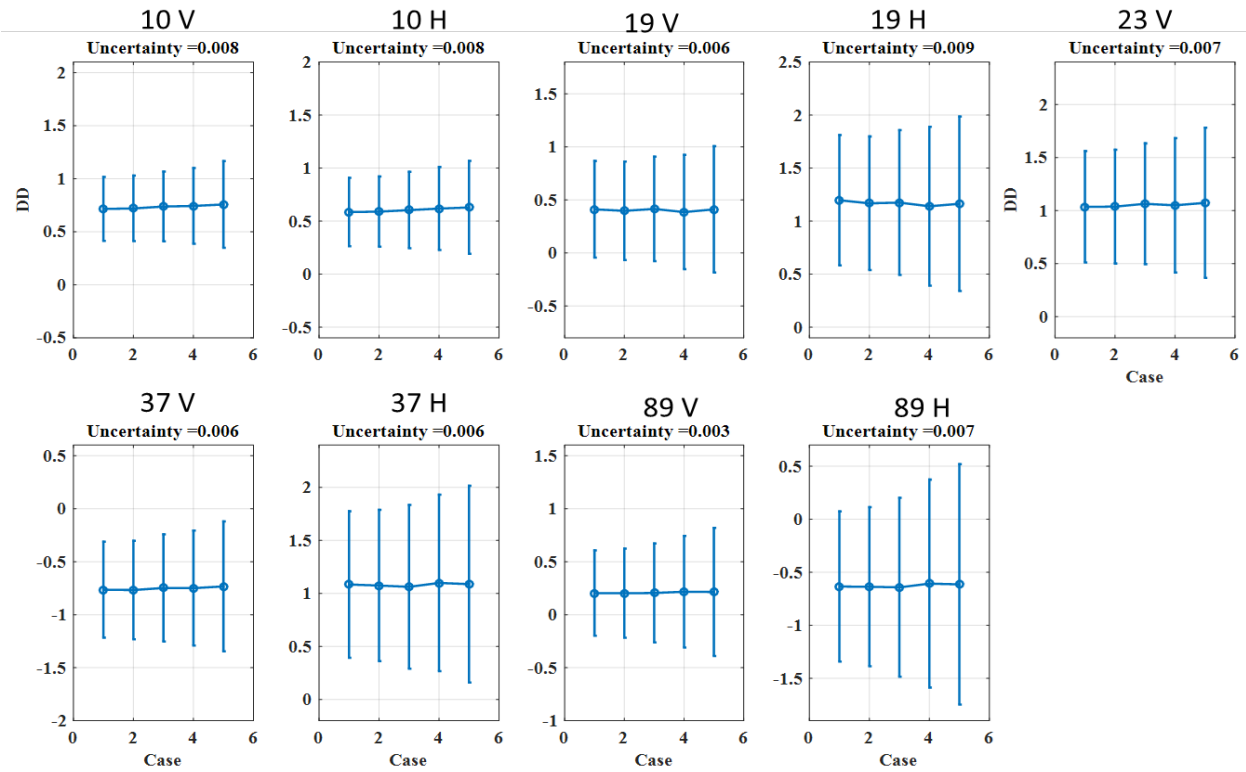


Figure 5-3 Double difference mean and STD of the common 9 channels between TMI and GMI for the 8 cases using different temporal resolutions. The dots represent mean values, and bars crossing the dots represent the values.

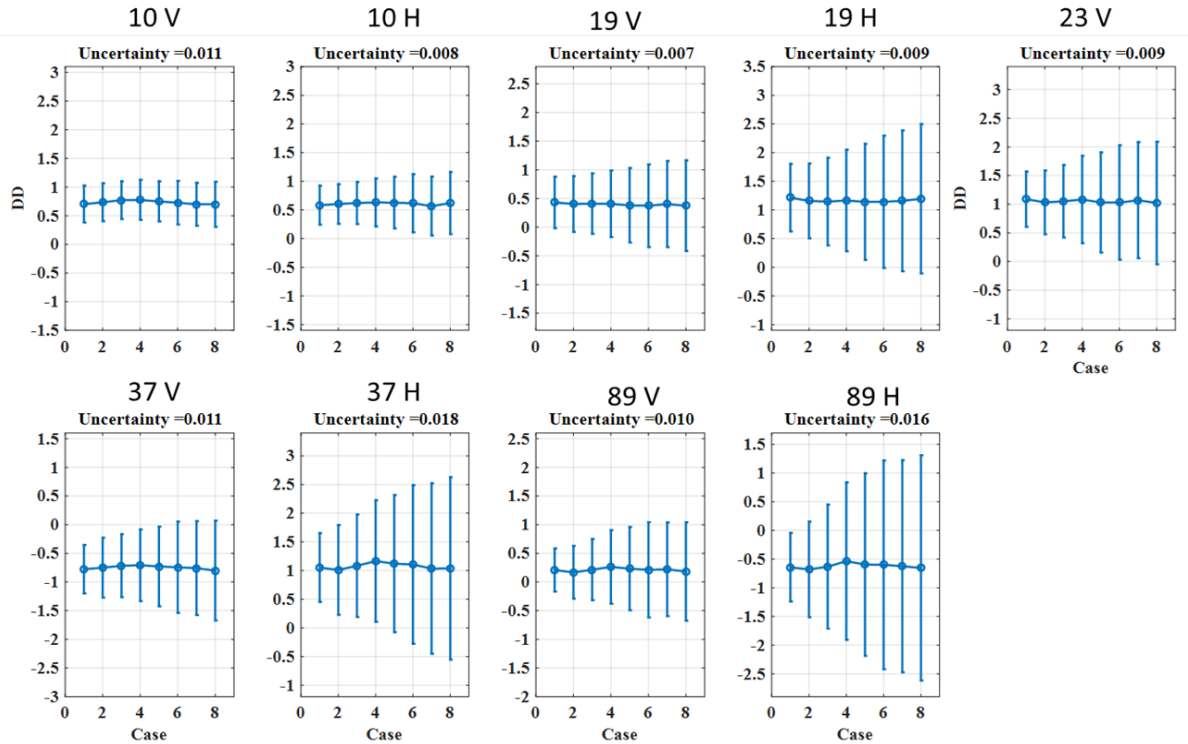


Figure 5-4 Double difference mean and STD of the common 9 channels between TMI and GMI for the 5 cases using different spatial resolutions. The dots represent mean values, and bars crossing the dots represent STD values.

Table 5-3 Standard uncertainty in sampling process.

	10V	10H	19V	19H	23V	37V	37H	89V	89H
Spatial Uncer.	0.008	0.008	0.006	0.009	0.007	0.006	0.006	0.003	0.007
Temporal Uncer.	0.011	0.008	0.007	0.009	0.009	0.011	0.018	0.010	0.016

5.3.2 Uncertainty in Geophysical Parameters

Modeling microwave Tb 's require knowledge of geophysical parameters such as sea surface temperature, wind speed, air temperature, air pressure, water vapor and cloud liquid water,

which are used as inputs to a RTM model to calculate the theoretical Tb 's for given radiometer channels, as shown in Figure 3-2. These parameters are usually obtained from GDAS (explained in Section 3.2) that is based on $1^\circ \times 1^\circ$ latitude/longitude grids. The GDAS product provides the needed atmospheric temperature, relative humidity, and cloud water density at 21 pressure layers, as well as surface measurements of sea surface temperature and ocean wind speed. As the knowledge of these parameters is imperfect, it is inevitable that the uncertainties are propagated to the output theoretical Tb 's through the RTM model and then further to the DD bias.

The NASA XCAL RTM is a state of the art for the physics associated with atmospheric and oceanic emissivity for the microwave window channels (<100 GHz). It consists of an atmosphere absorption model and a surface emissivity model, which requires environmental parameter inputs such as atmospheric water vapor (wv) and temperature profile, sea surface temperature and ocean surface wind speed to simulate Tb 's, as shown in Figure 5-4. The most important characteristic of the RTM is that it accurately captures the dynamic change of the ocean scene Tb , resulting from differences in the corresponding center frequency, bandwidth, EIA, polarization, and environmental parameters which are the inputs to the RTM, as well.

In microwave and millimeter frequency regions, the atmosphere model accounts for the absorption (emission) due to water vapor, oxygen and nitrogen as the blackbody noise emission radiation through the atmosphere. The inputs to the atmosphere absorption model includes the vertical profiles of temperature, pressure, and water vapor density (and the liquid water contribution of clouds, when present).

For clear-sky oceanic scenes, Tb 's below 90 GHz are dominated by surface emission. The ocean surface emissivity model is based upon specular Fresnel reflection that incorporates an ocean

dielectric constant model and a diffuse scattering wind-roughened ocean emissivity model with empirical coefficients. The inputs are sea surface temperature, wind speed, salinity, frequency, polarization and incidence angle. The surface model calculates the isotropic ocean surface emissivity and ignores small wind direction effects, which were investigated and found to average to zero globally and have negligible effect on the derived Tb biases.

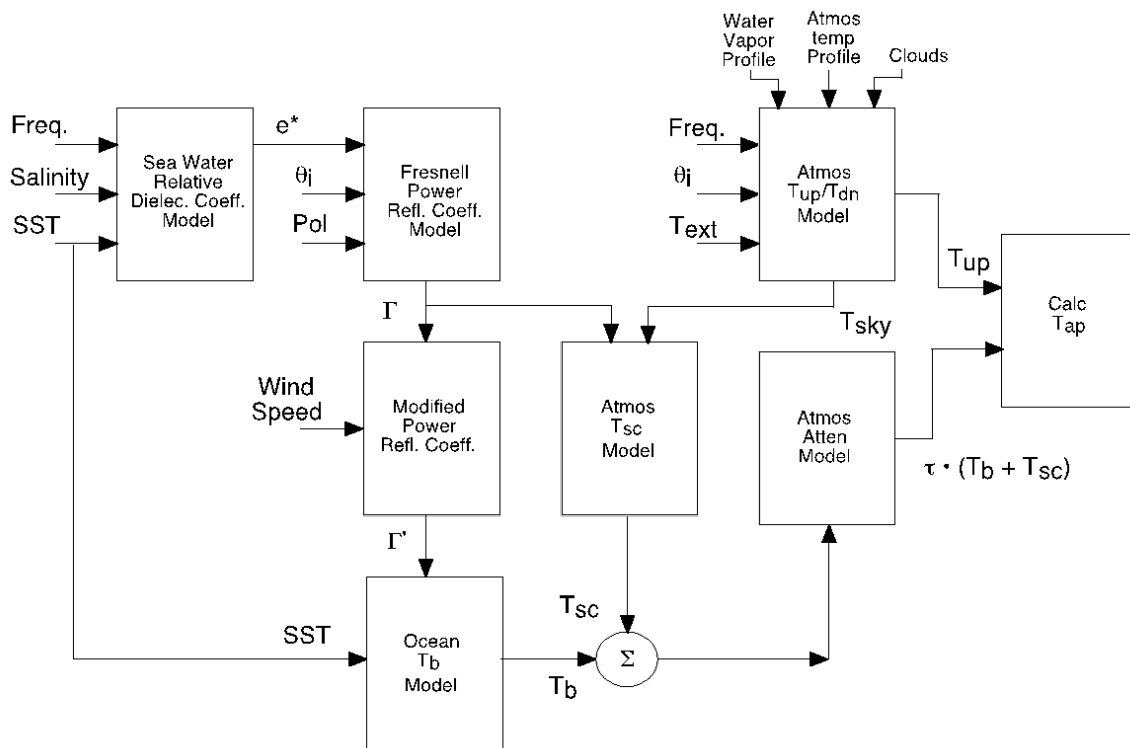


Figure 5-4 Block diagram of RTM.

As the RTM involves multiple input variables, and the relationship between the inputs and output theoretical Tb of the RTM model is quite complicated rather than linear, therefore, the Monte Carlo Simulation (MCS) Procedure is used here to quantify the uncertainty of the Tb bias propagated from the GDAS geophysical parameters.

5.3.2.1 Monte Carlo Simulation Procedure

The MCS procedure is a general approach for evaluating uncertainty where a theoretical approach would be difficult or inconclusive. The MCS procedure uses algorithmically generated pseudo-random numbers which are then forced to follow a prescribed probability distribution. For a normal distribution, the spread of random numbers is predetermined by its specified mean and its specified standard deviation. For each input, the MCS procedure generates a numeric value drawn at random from its respective probability density function (PDF). Numeric values derived in this manner are produced for all inputs to the known functional relationship which is then used to produce a single numeric value as output. The process is repeated a sufficiently large number of trials so as to produce a set of simulated results as output. The mean and standard deviation of these output results are then respective estimates of the measure and its standard uncertainty.

As these input parameters are randomly selected from the predefined probability distributions associated with each of the input variables, the overall process may thus be considered as a procedure for the propagation of distributions. Also, as the MCS procedure performs random sampling from the PDFs of the input parameters, it directly provides the probability distribution of the measure which is consistent with the PDFs of the inputs. This may be used to graphically display the distribution of output data and to directly determine the coverage interval of the measure even when the PDF of the measure has significant asymmetry [24].

In brief, the advantages of MCS procedures are as follows:

- 1) It “automatically” takes into account any nonlinearities in the functional relationship
- 2) If two inputs are correlated, the MCS procedure provides joint simulation of a bivariate distribution provided the correlation coefficient (or equivalently the covariance) has been

appropriately incorporated into the definition of the input PDF. In this manner, any correlation will have been explicitly taken into account after the completion of the MCS procedure.

- 3) A graphical representation of the distribution of the measurand can be obtained directly from the MCS procedure. In this manner, any non-normality or asymmetry in the distribution can usually be seen.
- 4) There is a significant reduction in the mathematical skills required for most evaluations.
- 5) The MCS procedure generally provides improved estimates for non-linear models.
- 6) The MCS procedure provides a coverage interval corresponding to a stipulated coverage probability.

5.3.2.2 Procedure of Monte Carlo Simulation

In order to investigate the uncertainty variation of the geophysical parameters associated with geophysical location, 8 different oceanic regions are selected within latitudes $[-45^\circ, +45^\circ]$ degree and longitudes $[-180^\circ, +180^\circ]$, as shown in Figure 5-5.

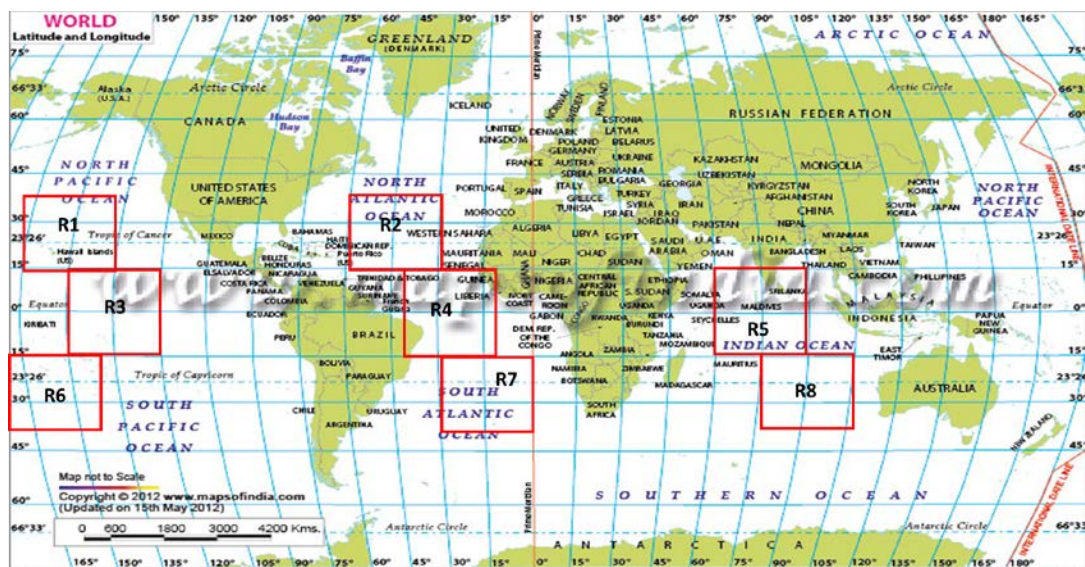


Figure 5-5 Select 8 regions that cover the whole oceans.

The atmospheric parameters taken into account in this MCS procedure are atmospheric temperature and water vapor profiles that are stored in 21 pressure layers in GDAS. The surface parameters include sea surface temperature and wind speed. The mean and rms values of these parameters are demonstrated in [25] and listed for each of the 8 regions in Table 5-4. The Monte Carlo simulation is run for 1300 iterations (larger than the minimum sample size 1270) over each region. In each iteration, 10,000 Gaussian distributed samples with predetermined mean and rms values in Table 5-4 are randomly generated for each of the four environmental parameters and then inputted into the RTM to simulate 10,000 theoretical T_b 's, to further calculate the DD bias using the CFRSL XCAL algorithm. An example histogram of 10,000 randomly sampled sea surface temperature for Region 1 (R1) is shown in Figure 5-6.

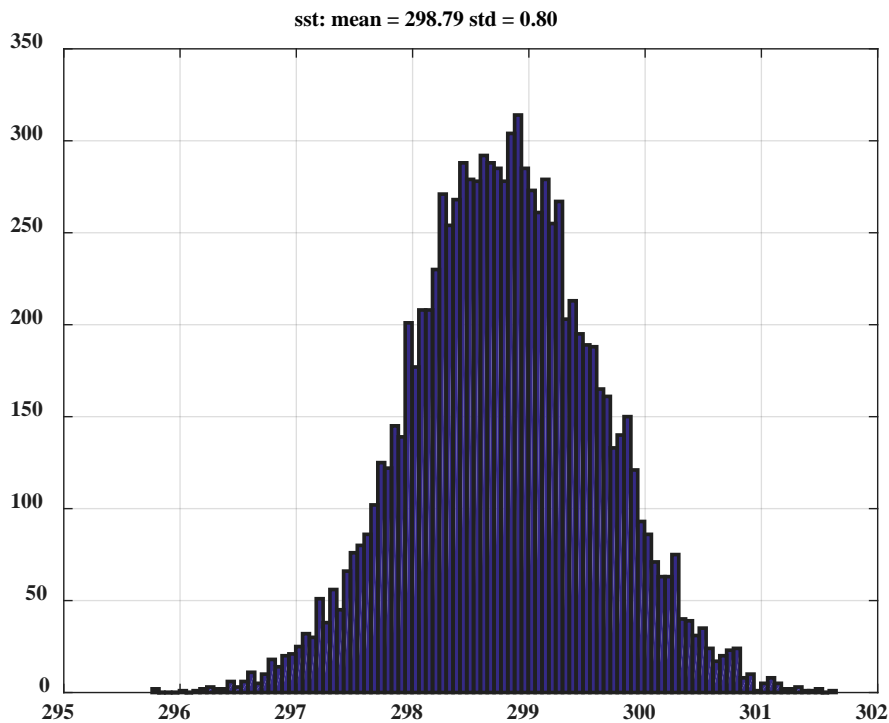


Figure 5-6 An example of randomly sampled sea surface temperature histograms at region 1.

The resulting *DD* biases from these 10,000 sets of geophysical parameters are presented in Figure 5-7, where biases follow near-Gaussian distributions that are consistent with the inputs distributions. Therefore, for each single MCS, the standard uncertainty is calculated using the Type A uncertainty estimation treatment to compute the standard deviation of the 10,000 calibration biases. With 1300 MCS iterations over each region, the averaged standard deviation of the calibration bias derived in this manner are then regarded as the standard uncertainty caused by geophysical parameter deficiency.

Table 5-4 Uncertainty in GDAS geophysical parameters for 8 oceanic regions [25].

	SST (K)		Wind speed (m/s)		Water Vapor (g/kg)		Atmosphere temperature (K)	
	bias	rms	bias	rms	bias	rms	bias	rms
R1	-0.3	0.8	-0.4	2.2	-0.5	1.6	-0.4	1.2
R2	-0.1	1.1	-1.0	3.0	0.1	1.1	-0.5	1.4
R3	-0.3	0.8	-0.4	2.2	-0.5	1.6	-0.4	1.2
R4	-0.1	1.1	-1.0	3.0	0.1	1.1	-0.5	1.4
R5	0.1	0.7	-0.4	2.3	-0.1	1.3	-0.2	0.9
R6	-0.3	0.8	-0.4	2.2	-0.5	1.6	-0.4	1.2
R7	-0.1	0.5	-0.7	2.0	0.8	1.3	-0.3	0.7
R8	0.1	0.7	-0.4	2.3	0.2	0.6	-0.2	0.9

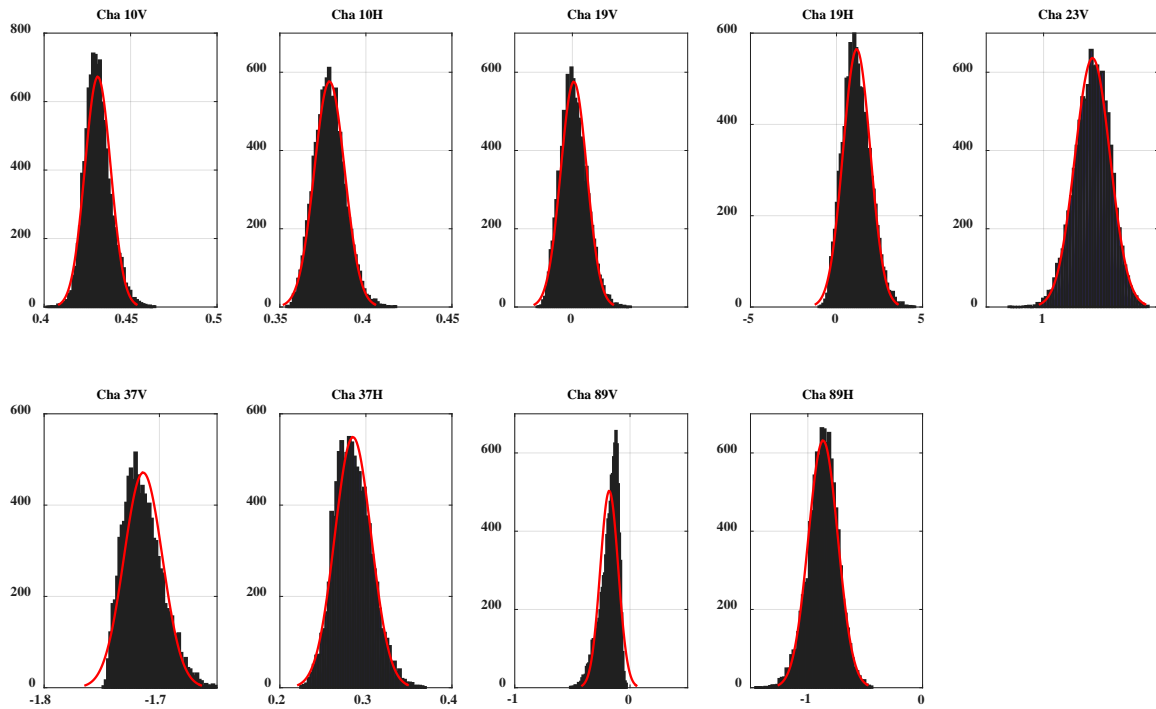


Figure 5-7 An example of double difference histograms for each channel at Region 1.

After 1300 iterations over each of the 8 regions, a total of 10,400 iterations are achieved. The standard uncertainties grouped by region for each channel using Mono absorption model are plotted in Figure 5-8 where the uncertainties of the same region are grouped together. Due to the fact that the Mono absorption model and Rosenkranz absorption model yield to calibration biases with offset as large as 1 K at 23 V channel as mentioned in Section 3.5.1, to assure that this method is independent of the absorption model selected, a similar procedure but using Rosenkranz absorption model is implemented, and the uncertainty estimates are shown in Figure 5-9. It is apparent that the patterns of the uncertainty distribution along regions are very similar between the two models.

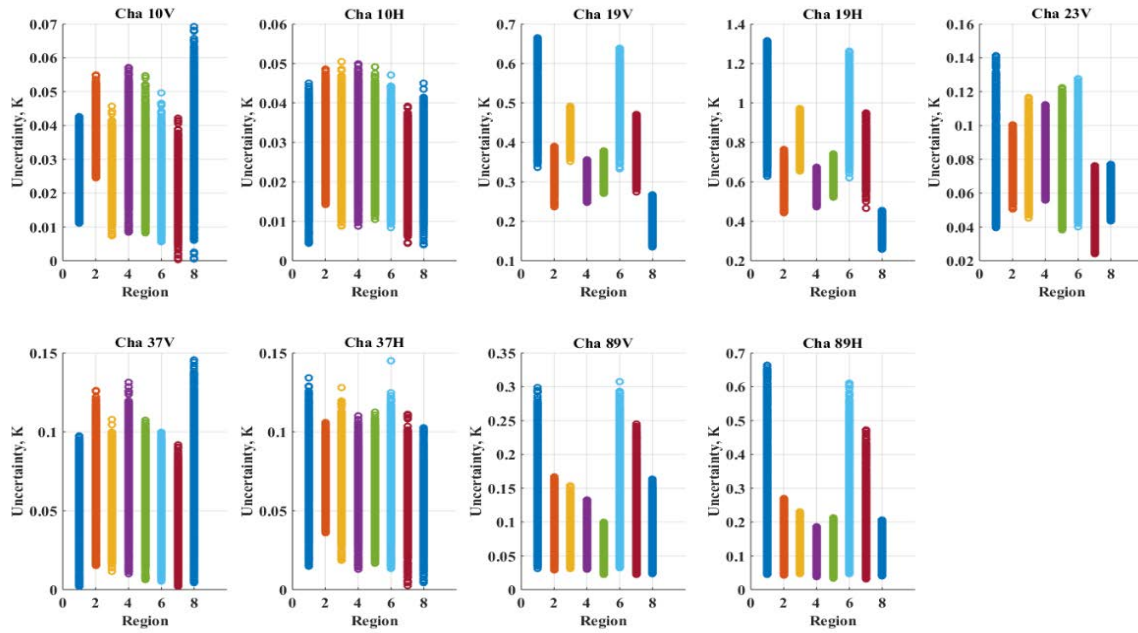


Figure 5-8 Uncertainty Estimates of 10,400 iterations grouped in region for each channel using Mono absorption model.

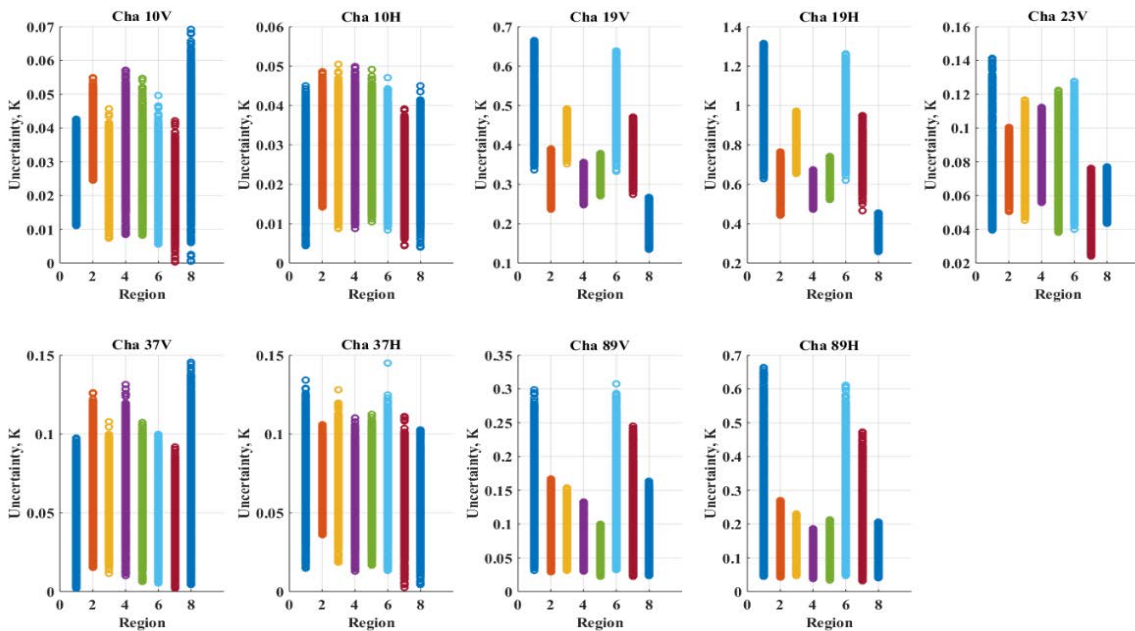


Figure 5-9 Uncertainty Estimates of 10,400 iterations grouped in region for each channel using Rosenkranz absorption model.

The standard uncertainties are then grouped into channels for each region, and results are presented in Figure 5-10 and Figure 5-11, in which Mono and Rosenkranz absorption models are used respectively. The similar patterns of the uncertainty distributions along regions using different absorption models are observed as well. The fact that the results using two different models do not vary, reinforces our confidence to use this method to quantify the uncertainty propagated from the geophysical parameters.

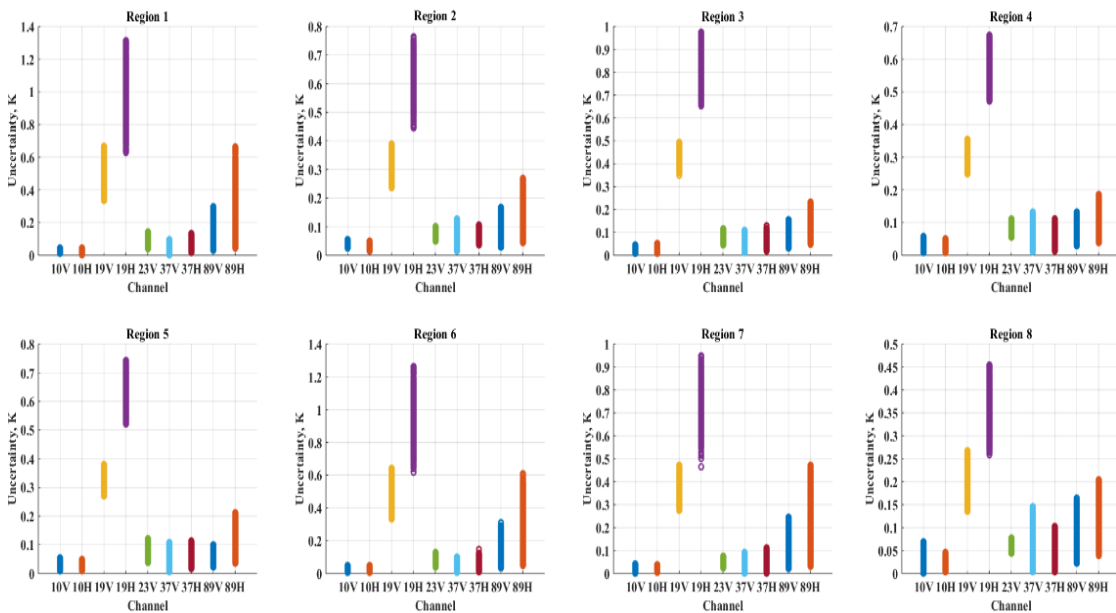


Figure 5-10 Uncertainty Estimates of 10,400 iterations grouped in channel for each region using Mono absorption model.

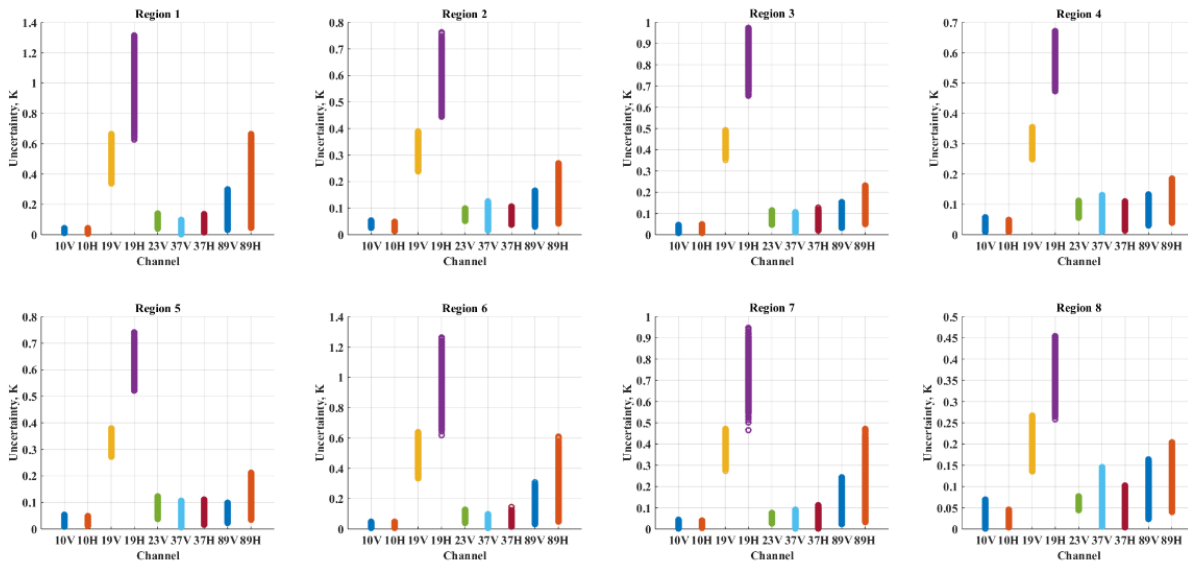


Figure 5-11 Uncertainty Estimates of 10,400 iterations grouped in channel for each region using Rosenkranz absorption model.

The averaged calibration bias and the standard uncertainties of the 10,400 iterations from 8 regions are calculated and listed in Table 5-5 and Table 5-6 for using different absorption models. As discussed earlier, the calibration bias using these two models are really close (<0.1 difference) at most channels, except for 19 V, 19 H and 23 V which are close to the 22.22 GHz water vapor line where the largest difference is 0.9 K at 23 V. However, when it comes to the standard uncertainty propagated from geophysical parameters, the difference between the two models are extremely small among all the channels with the largest 0.076 K at 19 H channel. The fact that the uncertainty propagation does not depend on RTM implies that the MCS procedure is reliable in assessing the GDAS uncertainty impact on the *DD* bias.

Table 5-5 Double difference bias between TMI and GMI.

	10V	10H	19V	19H	23V	37V	37H	89V	89H
MONO <i>DD</i>	0.70	0.56	0.18	0.78	0.05	-0.84	1.05	0.13	-0.85
Rosenkranz <i>DD</i>	0.72	0.59	0.45	1.26	1.07	-0.76	1.07	0.20	-0.63

Table 5-6 Standard uncertainties propagated from geophysical parameters.

	10V	10H	19V	19H	23V	37V	37H	89V	89H
MONO Uncer.	0.031	0.028	0.362	0.695	0.071	0.060	0.068	0.090	0.153
Rosenkranz Uncer.	0.031	0.027	0.339	0.653	0.080	0.061	0.071	0.088	0.154

Moreover, the averaged uncertainty of all the 1300 iterations on each region and each channel is listed in Table 5-7 using Mono/RSS RTM model. The regional uncertainties and the total uncertainty of each channel are then plotted in Figure 5-12. At most channels, the regional uncertainties are with extremely small discrepancy except 19 V and 19 H channels that have disparities as large as 0.3 and 0.6 K. The regions 1, 3 and 6 have much higher uncertainties, and region 8 the smallest, which are proportional to their rms values in water vapor 1.6 and 0.6 according to Table 5-4. This indicates that the calibration bias in 19 GHz is relative more sensitive to water vapor, consequently, the knowledge of water vapor needs to be enhanced in this regard.

Table 5-7 Regional standard uncertainties propagated from geophysical parameters.

	10V	10H	19V	19H	23V	37V	37H	89V	89H
Region 1	0.027	0.027	0.491	0.952	0.089	0.051	0.077	0.136	0.255
Region 2	0.038	0.032	0.318	0.612	0.075	0.071	0.070	0.084	0.126
Region 3	0.028	0.028	0.423	0.810	0.072	0.061	0.075	0.075	0.113
Region 4	0.037	0.032	0.303	0.573	0.077	0.073	0.064	0.070	0.105
Region 5	0.031	0.030	0.324	0.628	0.073	0.058	0.068	0.060	0.107
Region 6	0.027	0.027	0.476	0.920	0.074	0.051	0.074	0.120	0.224
Region 7	0.024	0.023	0.368	0.711	0.046	0.042	0.061	0.099	0.183
Region 8	0.038	0.027	0.196	0.352	0.059	0.073	0.054	0.077	0.112

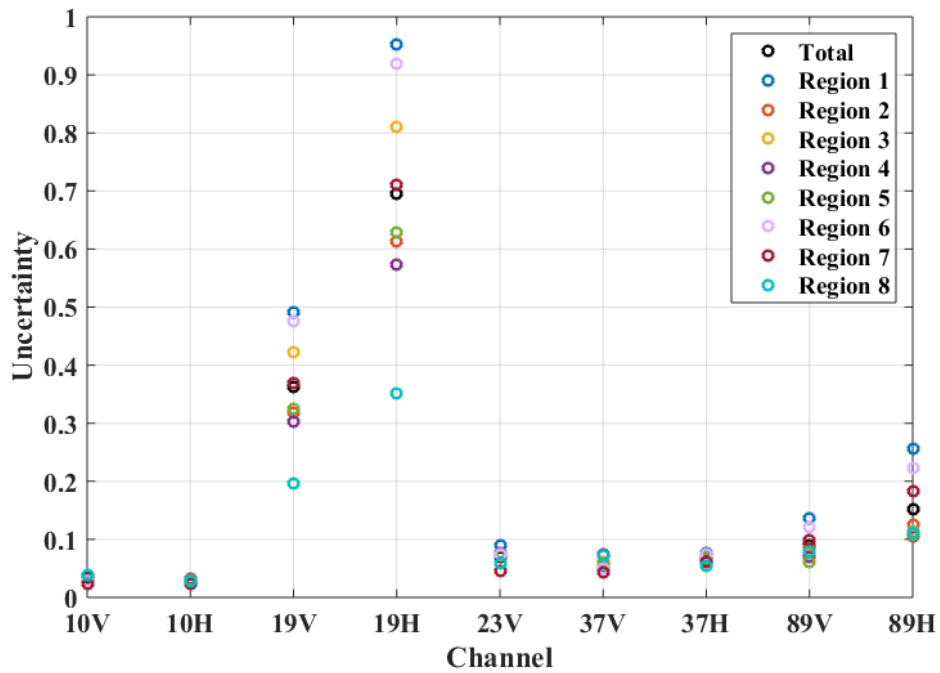


Figure 5-12 Regional standard uncertainty along with the total standard uncertainty for each channel.

5.3.3 Uncertainty in Rayleigh Jeans Approximation

The basic quantity which is intended to be measured by a microwave radiometer is power of electromagnetic radiation at the top of the atmosphere. For historic reasons, it is common in microwave physics to work in terms of brightness temperature Tb instead of the power, though in principle it would be just as easy to work in terms of power. The relationship between power and temperature is given by Planck's law as shown in the following equation:

$$I_f = \frac{2hf^3}{c^2} \left(\frac{1}{e^{hf/kT} - 1} \right) \quad (7)$$

where I_f is the spectral brightness intensity that a blackbody radiates uniformly in all directions with unit $\text{Wm}^{-2}\text{sr}^{-1}\text{Hz}^{-1}$, h is Planck's constant ($= 6.63 \times 10^{-34}$ joules*s), f is frequency (Hz), k is Boltzmann's constant ($= 1.38 \times 10^{-23}$ joules K^{-1}), T is the blackbody's absolute temperature (K), and c is the velocity of light in vacuum ($= 3 \times 10^8$ m/s). The only two variables appearing in equation (6), which includes intensities of two orthogonal polarizations, are f and T .

The use of Tb instead of power is justified by using the Rayleigh-Jeans (RJ) approximation shown in equation (7) to the correct Planck's law. The RJ approximation is very useful in the microwave region: it is mathematically simpler than Planck's law and yet its fractional deviation from Planck's exact expression is less than 1% if $f/T < 3.9 \times 10^8$ Hz K^{-1} [26]. With that being said, when a radiometer is pointing at the ground with surface temperature of 300 K, the RJ approximation will hold if $f < 117$ GHz, which covers the entire radio region and most of the usable part of the microwave spectrum.

However, to be more precise with the UQM development, the uncertainty due to approximation from Planck's Function to Rayleigh Jeans needs to be quantified and included. This

is done by calculating the standard deviation of the difference in the two sets of calibration biases derived using Planck's law and RJ approximation separately as expressed by the following equations:

$$\Delta Tb = Tb_{PF} - Tb_{RJ} \quad (8)$$

$$\Delta DD = \Delta Tb_{TMI} - \Delta Tb_{GMI} \quad (9)$$

$$SU_{RJ} = std(\Delta DD) \quad (10)$$

where Tb_{RJ} is the observed Tb from TMI or GMI, and Tb_{PF} is the Planck brightness temperature which is expressed as follows:

$$\begin{aligned} Tb_{PF} &= \frac{1}{k} \frac{hf}{e^{hf/kT} - 1} = \frac{hf}{k} \left(1 / \left(\sum_1^{\infty} \frac{(hf/kT)^n}{n!} \right) \right) \\ &= T - \frac{1}{2} \frac{hf}{k} + \frac{1}{12} \frac{hf}{k} \frac{hf}{kT} \pm \dots \end{aligned} \quad (1)$$

The RJ approximation to the Planck's law is the truncation of right side of equation (11) at 0th order which is T . This validates that the RJ Tb is equivalent to the Planck Tb . Hence, the difference between the full Planck brightness temperature and the RJ approximation is calculated as

$$\Delta Tb = Tb_{PF} - Tb_{RJ} \quad (2)$$

Figure 5-13 shows the difference as a function of observed Tb for 5 different frequencies of GMI. Figure 5-14 shows the difference as a function of frequency for 8 different Tb 's spanning from 50 to 400 K. It indicates that when the Tb becomes larger, the difference between the full Planck law and RJ approximation goes asymptotical to $-\frac{1}{2} \frac{hf}{k}$, which is the next term in the expansion of equation (11). This term is frequency dependent but temperature independent for most cases that occur in practice.

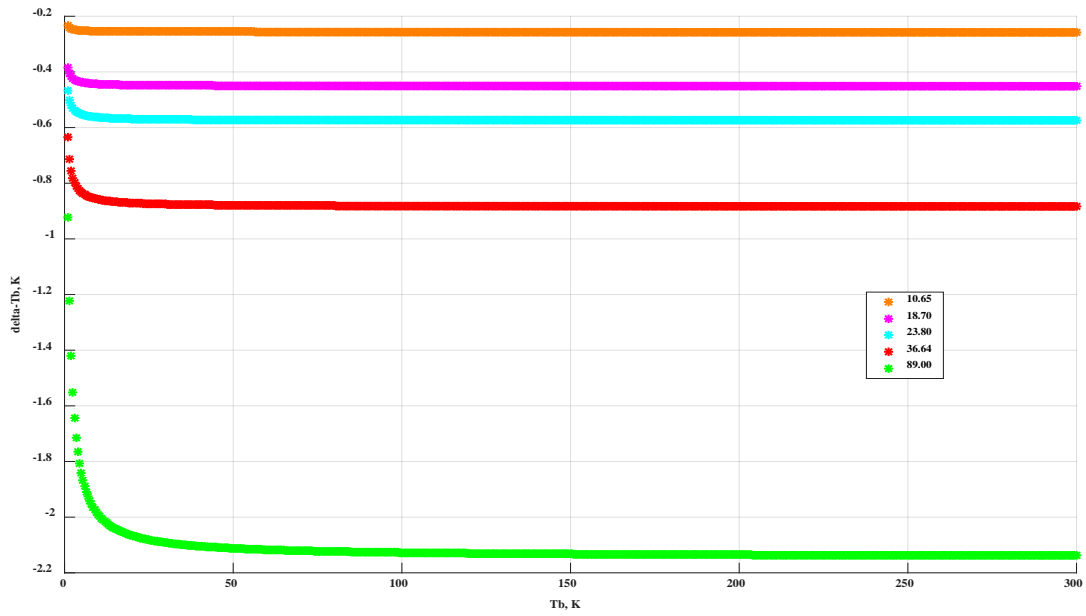


Figure 5-13 Difference (ΔT_b) of the Planck brightness temperature from Rayleigh-Jeans T_b at T_b varying between 0 and 300 K.

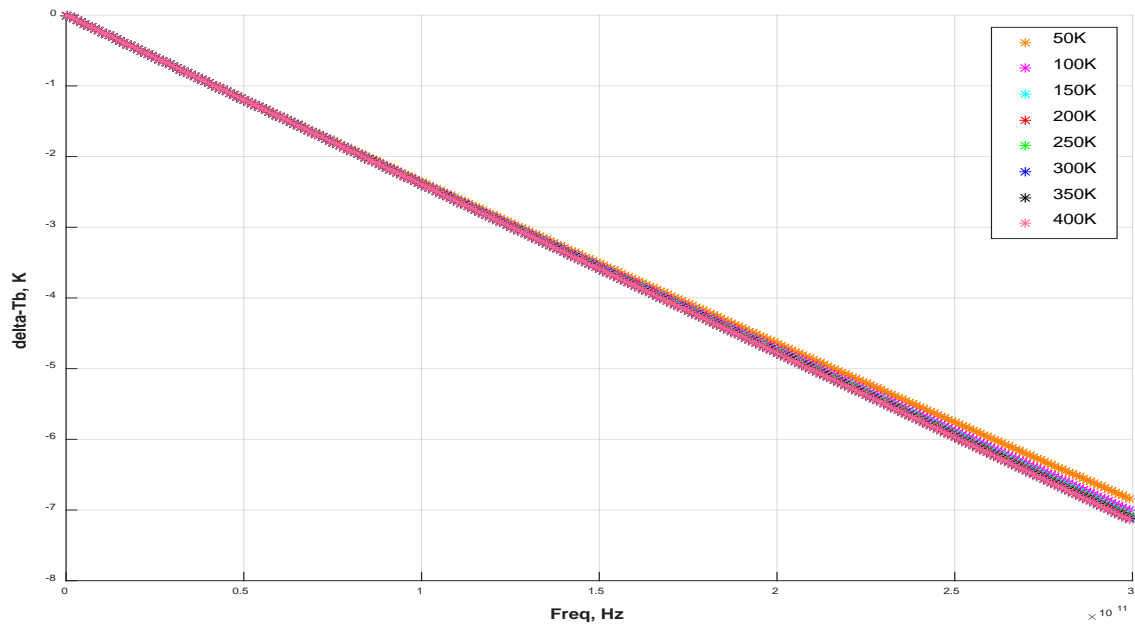


Figure 5-14 Difference (ΔT_b) of the Planck brightness temperature and Rayleigh-Jeans T_b at frequency varying between 0 and 300 GHz.

With collocated boxes of TMI and GMI, ΔTb is calculated for each instrument and the differences ΔDD between ΔTb 's of the two instruments are exhibited in Figure 5-15 for all the 9 common channels. Comparing to ΔTb magnitude in Figure 5-14, ΔDD is dramatically reduced by 13,000 times at 10 GHz (ΔDD for 10 GHz is almost zero K), this further indicates the robustness of CFRSL XCAL algorithm. Then, the Type A uncertainty estimation treatment is used to compute the standard uncertainty, as expressed in equation (9), and the results along with the absolute difference between GMI and TMI frequencies ($\Delta freq$) are presented in Table 5-8. The standard uncertainties are also plotted as a function of $\Delta freq$ as shown in Figure 5-16. The smallest uncertainty is at 10 V and 10 H channels, and largest at 89 V, which indicates that the uncertainty is proportional to the $\Delta freq$ values. Moreover, the uncertainty of H pol channels are almost two times of V pol, even though all the uncertainties are extremely small.

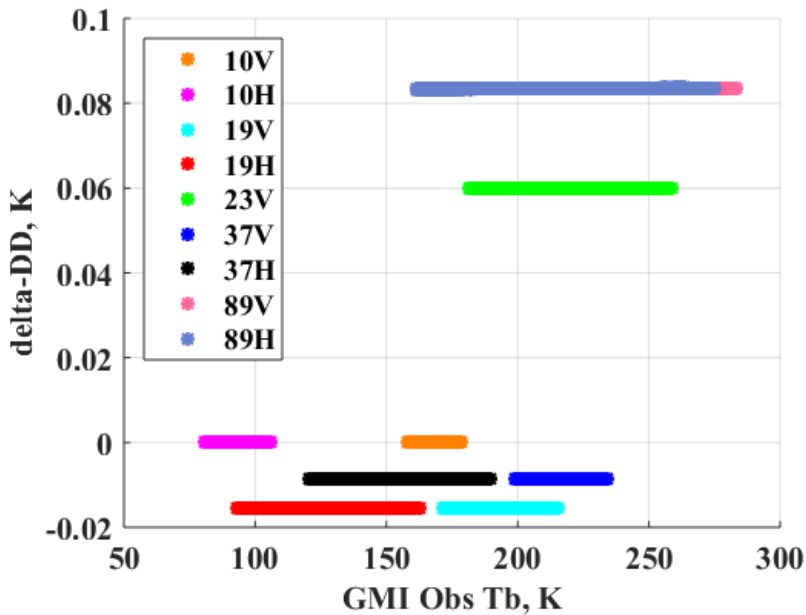


Figure 5-15 Difference (ΔDD) of ΔTb between TMI and GMI of their 9 common channels.

Table 5-8 Standard uncertainty propagated from Rayleigh-Jeans approximation.

Channel	10V	10	19V	19H	23V	37V	37H	89V	89H
diff	0.00	0.00	0.65	0.65	2.50	0.36	0.36	3.5	3.5
ΔDD	0.00	0.00	0.02	0.02	0.06	0.01	0.01	0.08	0.08
Uncer.	4.84	9.88	3.26	8.81	5.88	3.89	7.12	2.38	5.37
	$\times 10^{-7}$	$\times 10^{-7}$	$\times 10^{-6}$	$\times 10^{-6}$	$\times 10^{-6}$	$\times 10^{-6}$	$\times 10^{-6}$	$\times 10^{-5}$	$\times 10^{-5}$

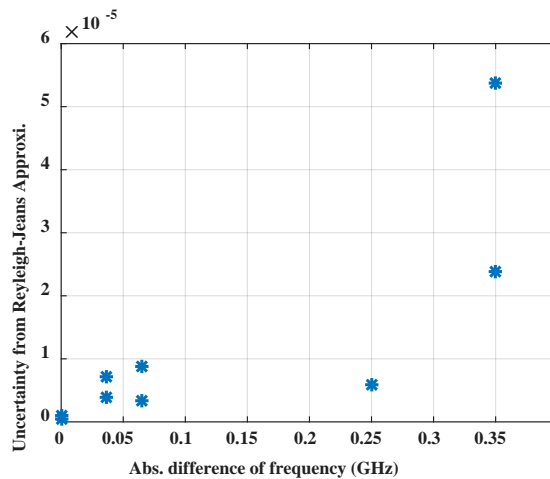


Figure 5-16 Standard uncertainty as a function of absolute difference between GMI and TMI frequencies.

5.3.4 Uncertainty in Different RTM and Different Geophysical Datasets

As described in Chapter 3, the NASA XCAL RTM consists of an atmosphere absorption model and a surface emissivity model. The Rosenkranz atmosphere model and Elsaesser surface model have been used for many years and recently replaced by the MONO and RSS models. Therefore, it is necessary to include the uncertainties caused by the deviation between these models into the UQM. Moreover, there are two geophysical parameter products: GDAS and ERA-I that

are generated by different numerical weather prediction models. Hence, the variance of these two sets of geophysical parameters needs to be taken into account as well.

The methods to quantify the uncertainty of two different RTM models as well input geophysical parameters are diagramed in Figures 5-17, 5-18, and 5-19. Basically, the CFRSL XCAL algorithm is run independently, using each of the corresponding models (atmospheric absorption, surface emissivity or numerical weather prediction models), and the standard deviation in their calibration bias difference is regarded as the uncertainty due to model deviation.

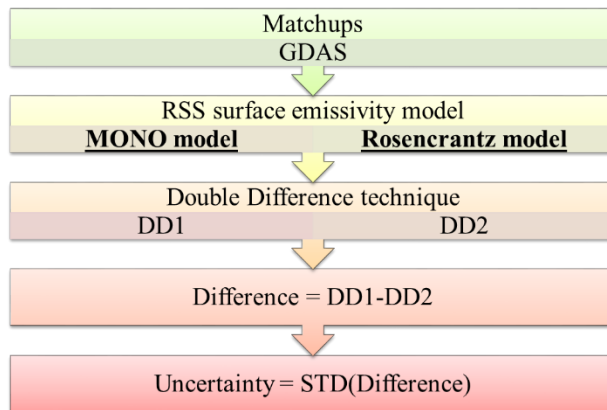


Figure 5-17 Diagram of uncertainty estimation procedure for Mono and Rosenkranz model deviation.

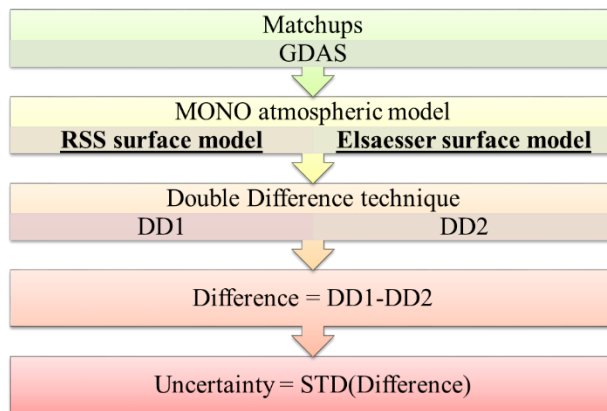


Figure 5-18 Diagram of uncertainty estimation procedure for RSS and Elsasser model deviation.

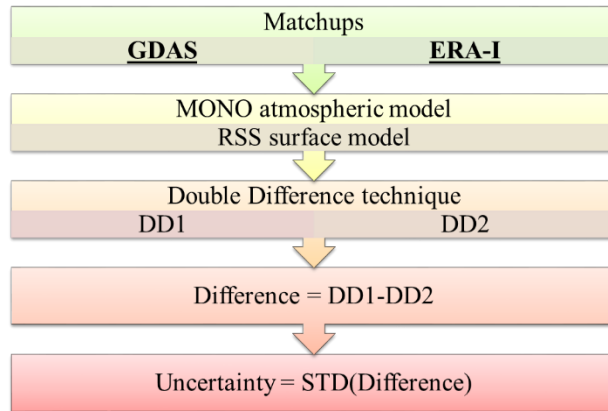


Figure 5-19 Diagram of uncertainty estimation procedure for GDAS and ERA-I model deviation.

With this procedure applied to these 3 pairs of models, the uncertainties with the averaged *DD* biases are derived individually per channel, and are presented in Table 5-9, Table 5-10, and Table 5-11.

Table 5-9 Standard uncertainty for Mono and Rosenkranz model deviation.

	10V	10H	19V	19H	23V	37V	37H	89V	89H
MONO <i>DD</i>	0.70	0.56	0.16	0.71	0.03	-0.82	1.05	0.19	-0.80
Rosenkranz <i>DD</i>	0.72	0.58	0.45	1.23	1.07	-0.75	1.07	0.25	-0.60
Uncertainty	0.005	0.006	0.089	0.159	0.222	0.009	0.009	0.047	0.113

Table 5-10 Standard uncertainty for RSS and Elsaesser model deviation.

	10V	10H	19V	19H	23V	37V	37H	89V	89H
RSS <i>DD</i>	0.70	0.56	0.16	0.71	0.03	-0.82	1.05	0.19	-0.79
Elsaesser <i>DD</i>	0.71	0.58	0.22	1.06	0.01	-0.83	1.12	0.18	-0.68
Uncertainty	0.023	0.01	0.034	0.127	0.038	0.015	0.039	0.026	0.042

Table 5-11 Standard uncertainty for GDAS and ERA-I deviation.

	10V	10H	19V	19H	23V	37V	37H	89V	89H
GDAS <i>DD</i>	0.70	0.56	0.16	0.71	0.03	-0.82	1.05	0.19	-0.79
ERA-I <i>DD</i>	0.71	0.58	0.22	1.06	0.01	-0.83	1.12	0.18	-0.68
Uncertainty	0.024	0.011	0.034	0.127	0.038	0.015	0.039	0.026	0.042

5.4 Uncertainty Estimates Combination

The estimated individual independent uncertainty should be combined into a single overall uncertainty using the root sum squared (rss) method expressed as follows:

$$u_{combined} = \sqrt{(u(a))^2 + (u(b))^2 + (u(c))^2 + \dots etc.} \quad (3)$$

With the standard uncertainties from 7 independent sources summarized in Table 5-12, the rss uncertainties are calculated and listed in the last row of the table.

Furthermore, the use of GMI as a transfer standard demands its high calibration stability and calibration uncertainty be considered. The design of GMI was predicated on eliminating potential (and in some cases observed) calibration issues (see details in Appendix B) and it has been proved that the GMI is carefully and well-designed instrument, with its calibration uncertainty documented in [5] where the coverage factor of $k = 3$. Hence, the standard uncertainties are one third of those shown in Table 5-13. With the GMI calibration uncertainty combined, the overall standard uncertainties combining all the 8 independent uncertainties are presented in Table 5-13. In order to include 99% of the distribution, the coverage factor should be 3 and the expanded uncertainty should be 3 times of the combined standard uncertainty (see Table 5-13).

After all, comparing to the RSS values in Table 5-12 and the combined standard uncertainty in Table 5-13, the uncertainty is increased dramatically after including the GMI calibration uncertainty in all the channels except 19V and 19H, which indicates that the GMI calibration is playing a dominant part in the overall uncertainty of the *Tb* products. The fact that the two largest uncertainties lie in 19 H and 19 V probably result from the inadequate knowledge of water vapor in the numerical weather prediction models and the imperfect radiative transfer modeling of the water vapor resonance near 22.22 GHz.

Table 5-12 rss uncertainty without GMI calibration uncertainty.

Channel	10V	10H	19V	19H	23V	37V	37H	89V	89H
Spatial uncer.	0.007	0.008	0.006	0.009	0.007	0.006	0.006	0.003	0.007
Temporal uncer.	0.011	0.008	0.007	0.009	0.009	0.011	0.018	0.010	0.016
GDAS uncer.	0.031	0.028	0.362	0.695	0.071	0.060	0.068	0.090	0.153
Atmos. uncer.	0.005	0.006	0.089	0.159	0.222	0.009	0.009	0.047	0.113
Surf. uncer.	0.024	0.011	0.034	0.127	0.038	0.015	0.039	0.026	0.042
Environ. uncer.	0.014	0.015	0.235	0.457	0.158	0.028	0.039	0.053	0.095
RJA uncer.	4.84 $\times 10^{-7}$	9.88 $\times 10^{-7}$	3.26 $\times 10^{-6}$	8.81 $\times 10^{-6}$	5.88 $\times 10^{-6}$	3.89 $\times 10^{-6}$	7.12 $\times 10^{-6}$	2.38 $\times 10^{-5}$	5.37 $\times 10^{-5}$
rss (w/o GMI)	0.044	0.036	0.442	0.857	0.284	0.069	0.090	0.118	0.217

Table 5-13 Combined uncertainty with GMI calibration uncertainty.

Channel	10V	10H	19V	19H	23V	37V	37H	89V	89H
GMI standard uncer.	0.400	0.400	0.420	0.420	0.323	0.260	0.260	0.353	0.353
Combined standard uncer.	0.402	0.402	0.610	0.954	0.431	0.270	0.275	0.372	0.415
Combined expanded uncer.	1.207	1.205	1.829	2.862	1.292	0.807	0.826	1.117	1.245

6 UNCERTAINTY QUANTIFICATION OF TMI/WINDSAT AND WINDSAT/GMI INTERCALIBRATION

Given the fact that WindSat is used as a calibration bridge between the GMI and the TMI when there is no overlap time in between to provide additional intercalibration for creating a consistent multi-decadal oceanic brightness temperature, it is important to assess the uncertainty associated with the calibration bias between TMI and WindSat as well as between WindSat and GMI. This chapter focuses on presenting the results and analysis after applying the UQM described in Chapter 5 to the intercalibration between TMI and WindSat for 6 years (XCAL year, 2007, 2011, 2012, 2013, and 2014), covering a more than 8-year period, and to the intercalibration between WindSat and GMI for year 2015.

6.1 UQM Applied to TMI/WindSat Intercalibration in long-term

WindSat has been in operation since its launch in 2003, and the timespan that both TMI and WindSat data are available is more than 12 years. In this dissertation, 6 years of *Tb* measurements from the two instruments are analyzed individually regarding their calibration bias and uncertainty, and then compared together to further assess the long-term consistency.

The CFRSL XCAL algorithm is first applied to derive the calibration bias of each year using the Mono atmospheric absorption model, RSS surface emissivity model and GDAS environmental parameters. Averaged biases are listed in Table 6-1 and are plotted along with the STD in Figure 6-1 from which we can observe that the averaged biases are consistent over time with very small drift (maximum 0.22 K) between year 2007 and 2011 at 19 GHz.

Table 6-1 Averaged calibration biases of TMI/ WindSat intercalibration.

Year	10V	10	19V	19H	23V	37V	37H
XCAL year	1.05	1.15	-1.40	-1.66	-1.87	-2.33	-0.46
2007	1.07	1.17	-1.44	-1.65	-1.80	-2.36	-0.44
2011	1.10	1.17	-1.24	-1.45	-1.76	-2.30	-0.45
2012	1.09	1.18	-1.22	-1.39	-1.75	-2.30	-0.40
2013	1.09	1.20	-1.21	-1.38	-1.77	-2.29	-0.39
2014	1.09	1.19	-1.22	-1.40	-1.71	-2.26	-0.39

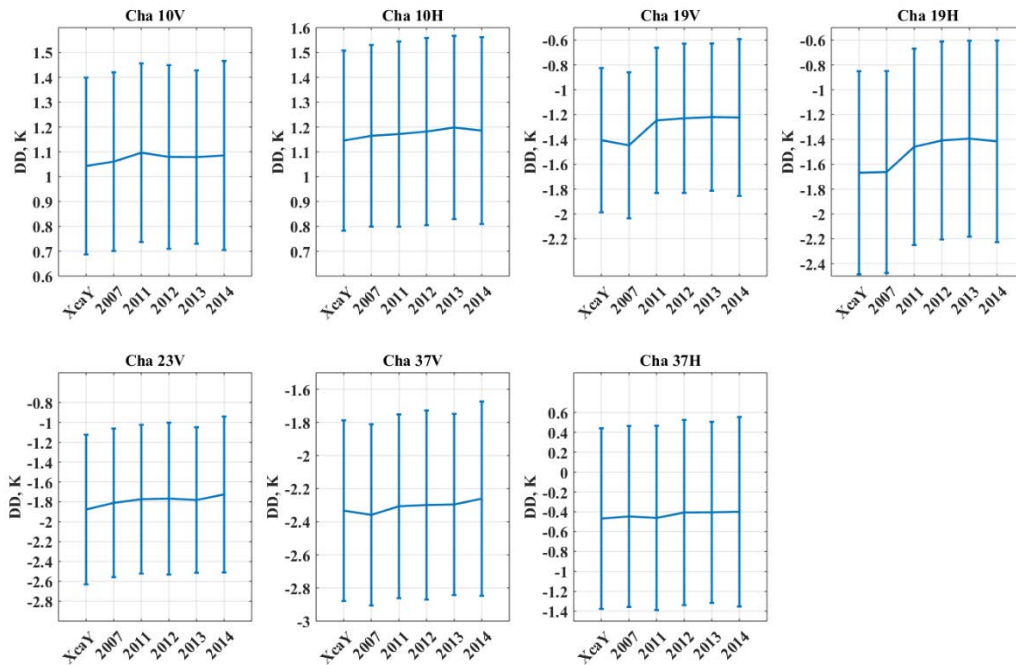


Figure 6-1 Mean and standard deviation of calibration bias of TMI relative to WindSat for 6 years between 2005 and 2014.

Next, we examine the calibration DD biases versus month of the year for the 6-year time series of TMI/WindSat. This comparison is significant because of the season variation of environmental parameters will result in dynamic changes in the monthly average scene brightness temperature, and this also impacts the RTM modeled Tb's. Results shown in Figure 6-2 demonstrate that, for the majority of channels, the biases are consistent from month to month, with the std being < 0.1 K. On the other hand, for the water vapor sensitive channels, a peak-to-peak 0.5 K variability occurs at 19 GHz and 23 GHz. Further, it is noted that the first two years are similar, but a step function change (~ 0.2 K) occurs at the third year, and this is stable for years 3-6. More analysis (shown in Appendix C) has been performed, and it has been suspected that the causes of bias variation may be the change of the GDAS geophysical parameters, which are used as inputs to the RTM. Although it is desirable to achieve zero-drift in the bias, this small step function change is acceptable.

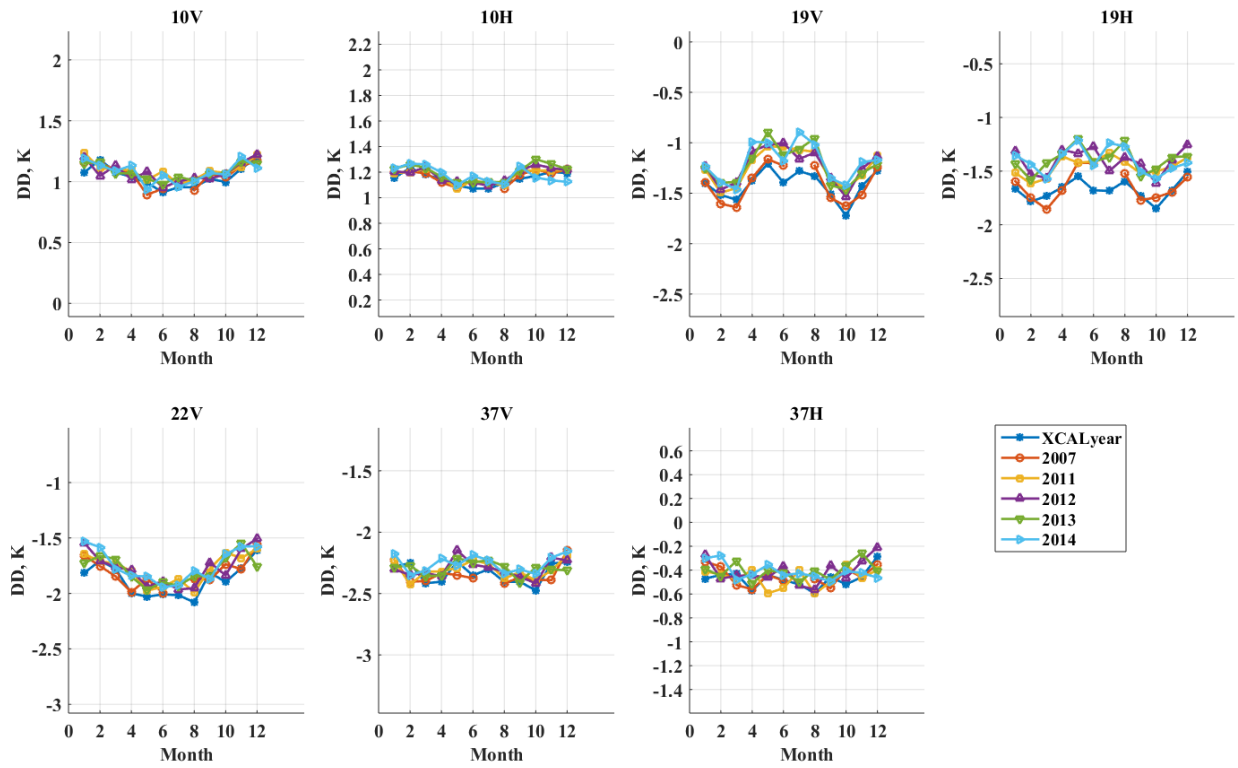


Figure 6-2 Monthly calibration bias of TMI relative to WindSat for 6 years between 2005 and 2014.

In addition, the UQM needs to be applied to the TMI and WindSat intercalibration for the 6 years individually. First of all, the spatial and temporal uncertainties of 2011 are presented in Figures 6-3 and 6-4, respectively, on a channel basis. Small uncertainties are obtained with the maximum 0.033 K of spatial uncertainty in 37H channel. The same results, for all of the 6 years combined, are given in Figure 6-5 and Figure 6-6, which shows high consistency with respect to uncertainties of the different years and the highest variation in 19 GHz.

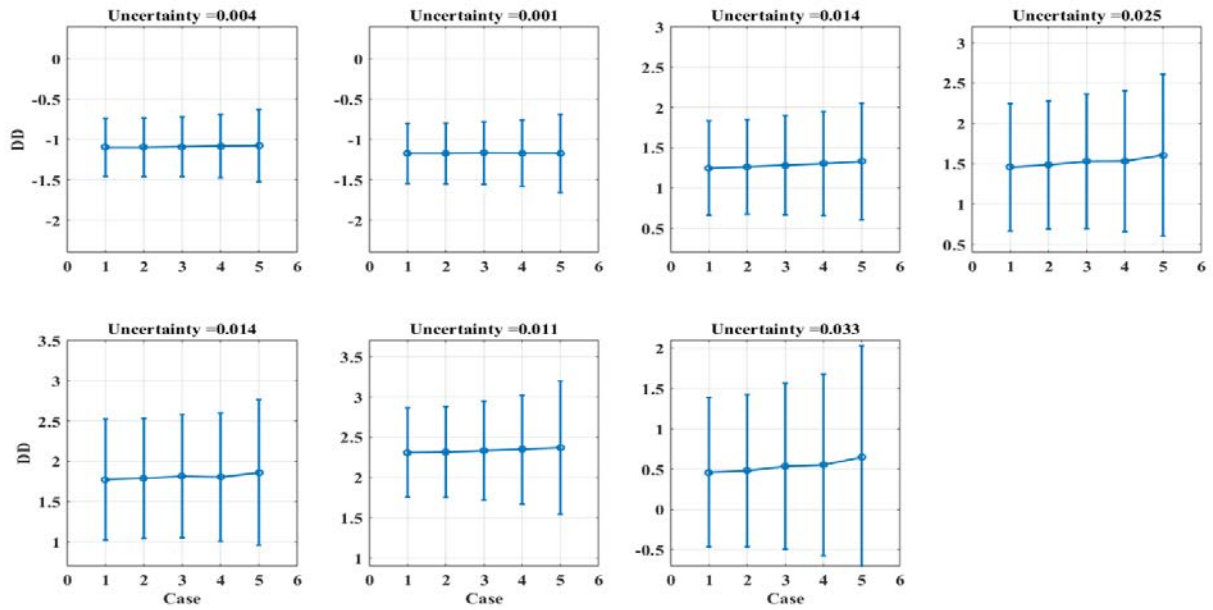


Figure 6-3 Mean, standard deviation and spatial uncertainty of double difference bias between TMI and WindSat per channel for year 2011.

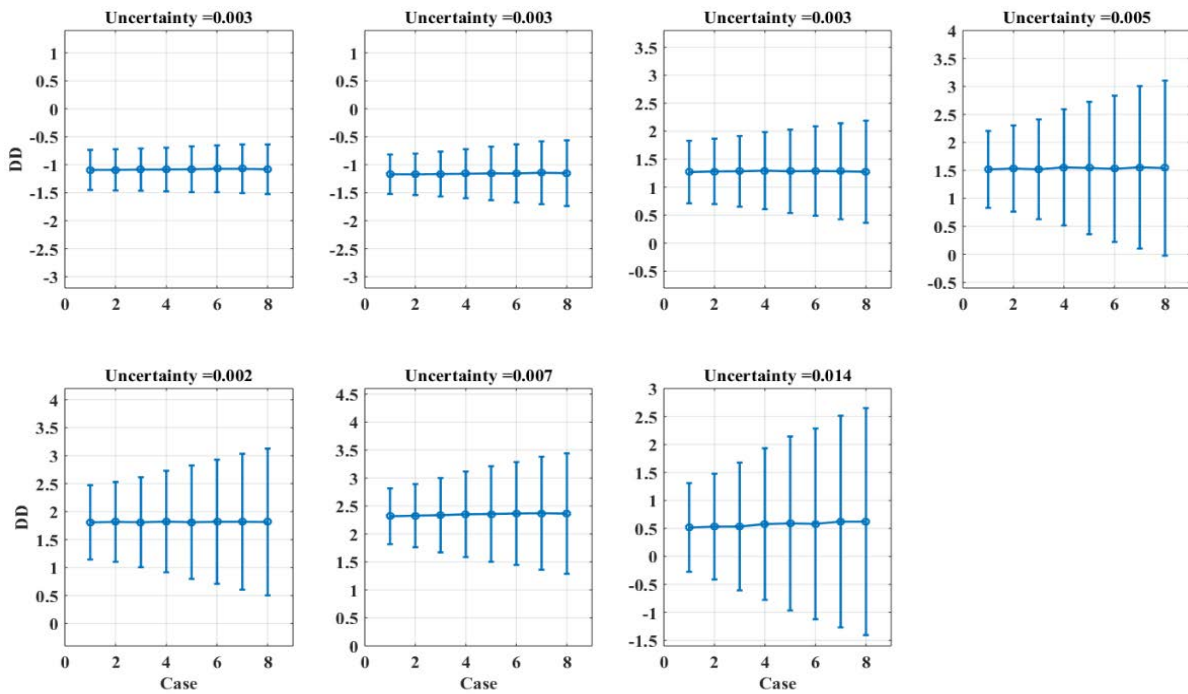


Figure 6-4 Mean, standard deviation and temporal uncertainty of double difference bias between TMI and WindSat per channel for year 2011.

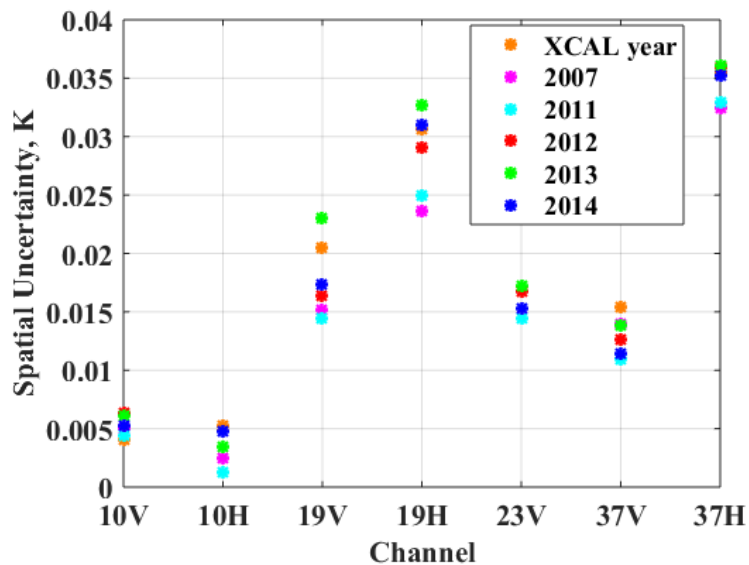


Figure 6-5 Spatial uncertainties of double difference biases between TMI and WindSat per channel for 6 different years.

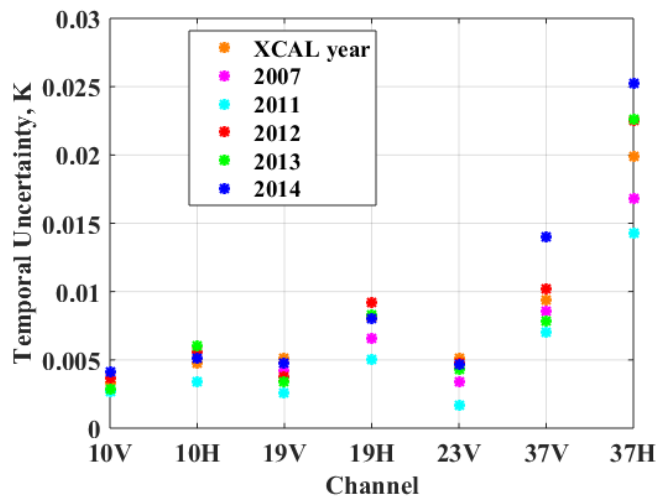


Figure 6-6 Temporal uncertainties of double difference biases between TMI and WindSat per channel for 6 different years.

The next step is to quantify the uncertainty propagated from geophysical parameters as described in Section 5.3.2 for the 6 years individually. Over each of the 8 regions, 2300

independent MCS iterations are run, which yields a total of 18,400 uncertainties. Since the results of different years are very close, for illustration purpose, the uncertainties for year 2011 are shown in Figure 6-7 and Figure 6-8. Figure 6-7 groups the uncertainties based on channel for each region, and Figure 6-8 groups based on regions per channel. The region 1, 3 and 6 located at Pacific Ocean have the highest uncertainty (1.6 rms) of water vapor, which results in higher uncertainties than the other 5 regions, especially the region 8 where the lowest water vapor uncertainty (0.6 rms) occurs. Among all the 9 channels, the 19 GHz V and 19 GHz H channels show the highest uncertainties, due to the strong sensitivity to water vapor density near 22.2 GHz. The combination of the results for all 6-year uncertainties are combined in Figure 6-9, and the resulting uncertainties for the entire time series is very small, with the maximum standard error 0.002 K occurring for the 19 GHz H-pol channel.

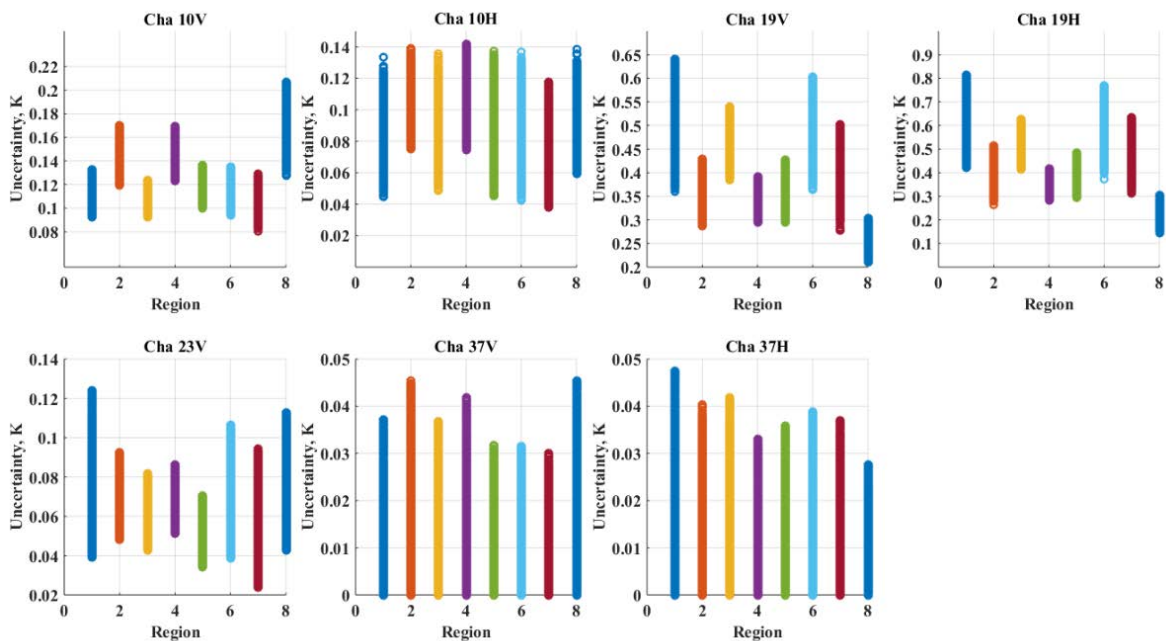


Figure 6-7 Uncertainty Estimates of 18,400 iterations grouped in region for each channel for TMI and WindSat intercalibration of year 2011.

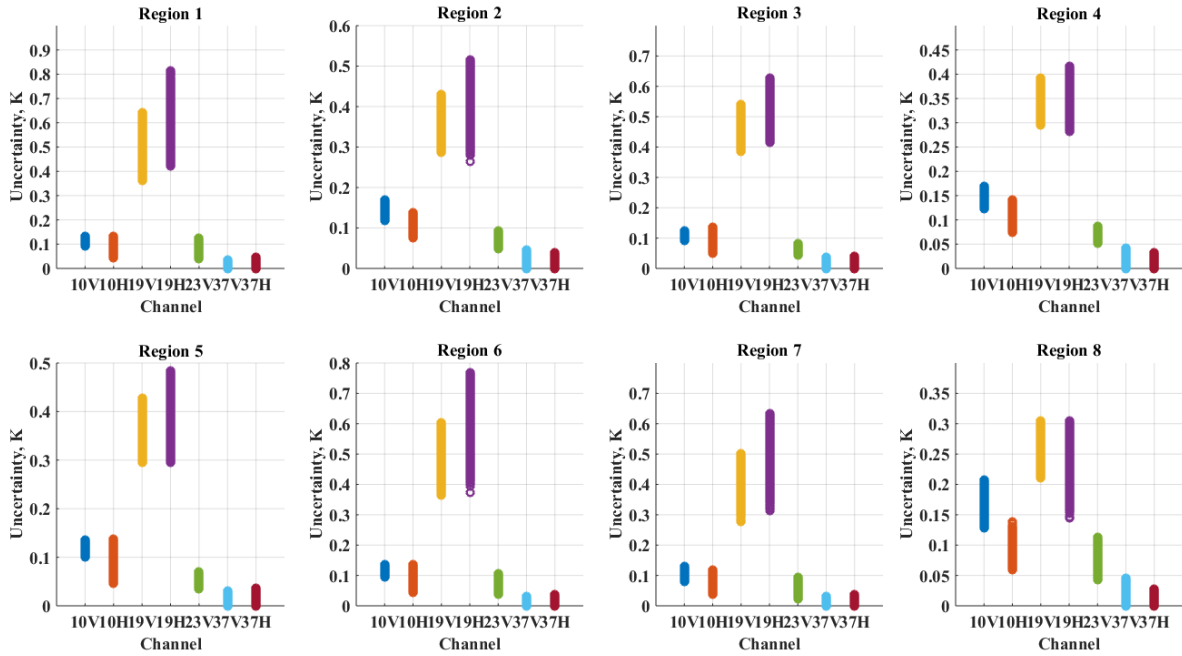


Figure 6-8 Uncertainty Estimates of 18,400 iterations propagated from GDAS are grouped in channel for each region for TMI and WindSat intercalibration of year 2011.

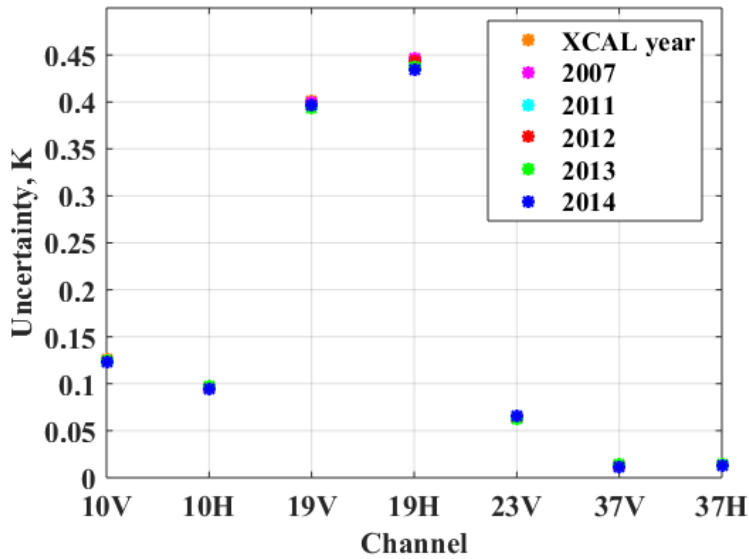


Figure 6-9 Uncertainty Estimates from GDAS of TMI and WindSat intercalibration for the 6 years.

Then, the uncertainty caused by Rayleigh-Jeans approximation from the Planck's Law is evaluated subsequently and the results of all the 6 years are presented in Figure 6-10.

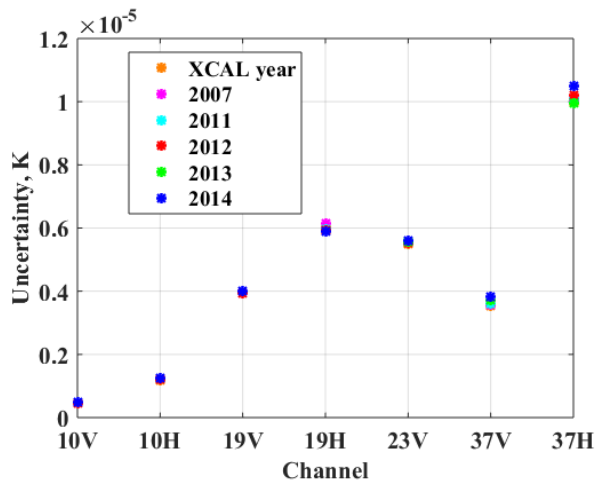


Figure 6-10 Uncertainty Estimates of TMI and WindSat intercalibration in Rayleigh-Jeans Approximation from Planck's Law for the 6 years.

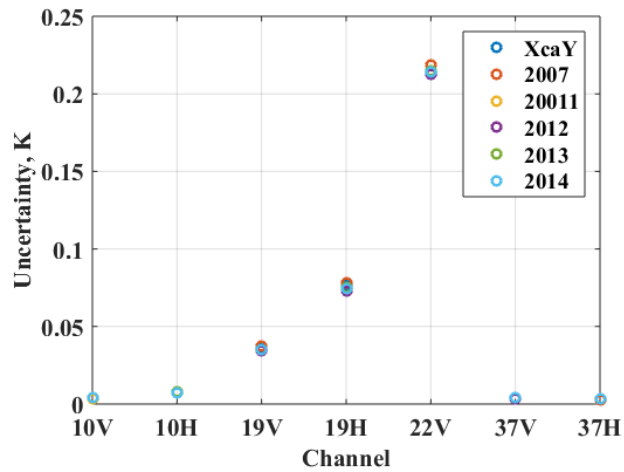


Figure 6-11 Uncertainty Estimates in MONO and Rosenkranz atmosphere absorption models for TMI and WindSat intercalibration for the 6 years.

The last step is to quantify the uncertainty caused by different RTM's and numerical weather models. As Figures 6-11, 6-12, and 6-13 show, the uncertainty difference among all the years regarding different atmosphere absorption models (Rosenkranz and Mono), surface emissivity models (Elsaesser and RSS) and numerical weather models (GDAS and ERA-I) are quite small.

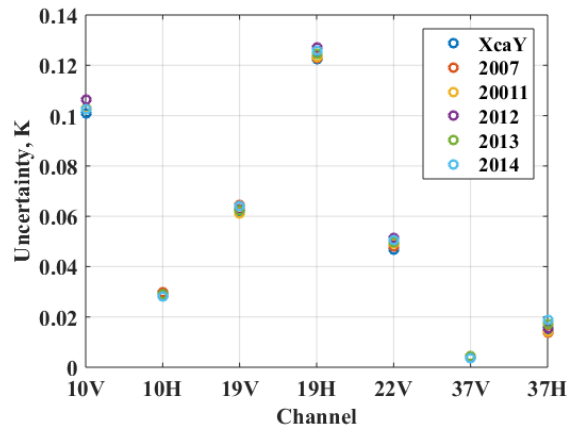


Figure 6-12 Uncertainty Estimates in Elsaesser and RSS surface emissivity models for TMI and WindSat intercalibration for the 6 years.

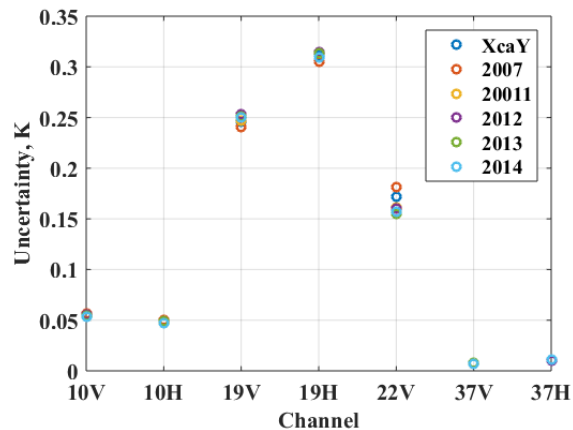


Figure 6-13 Uncertainty Estimates in discrepancy between ERA-I and GDAS models for TMI and WindSat intercalibration for the 6 years.

As a summary, the combined standard uncertainties with GMI calibration uncertainty are shown in Table 6-2, which shows significant consistency over the years with maximum standard error 0.001 K. This demonstrates the excellent stability in the long-term intercalibration between the TMI and the WindSat.

Table 6-2 Combined standard uncertainty of TMI/ WindSat intercalibration.

	10V	10	19V	19H	23V	37V	37H
XCAL year	0.435	0.415	0.635	0.703	0.432	0.261	0.264
2007	0.435	0.416	0.632	0.701	0.438	0.261	0.263
2011	0.435	0.415	0.632	0.699	0.428	0.261	0.264
2012	0.436	0.415	0.634	0.703	0.427	0.261	0.264
2013	0.435	0.416	0.632	0.698	0.426	0.261	0.265
2014	0.434	0.415	0.634	0.695	0.427	0.261	0.265

6.2 UQM Applied to WindSat/GMI Intercalibration

To complete the goal of the creating a consistent oceanic multi-decadal intercalibrated TMI-GMI constellation data record using the WindSat as a calibration bridge, the UQM model described in Chapter 5 was applied to the WindSat/GMI intercalibration for year 2015, and this chapter presents the main results and analysis.

First, the spatial and temporal uncertainties along with mean and std of calibration biases per channel are presented in Figures 6-14 and 6-15.

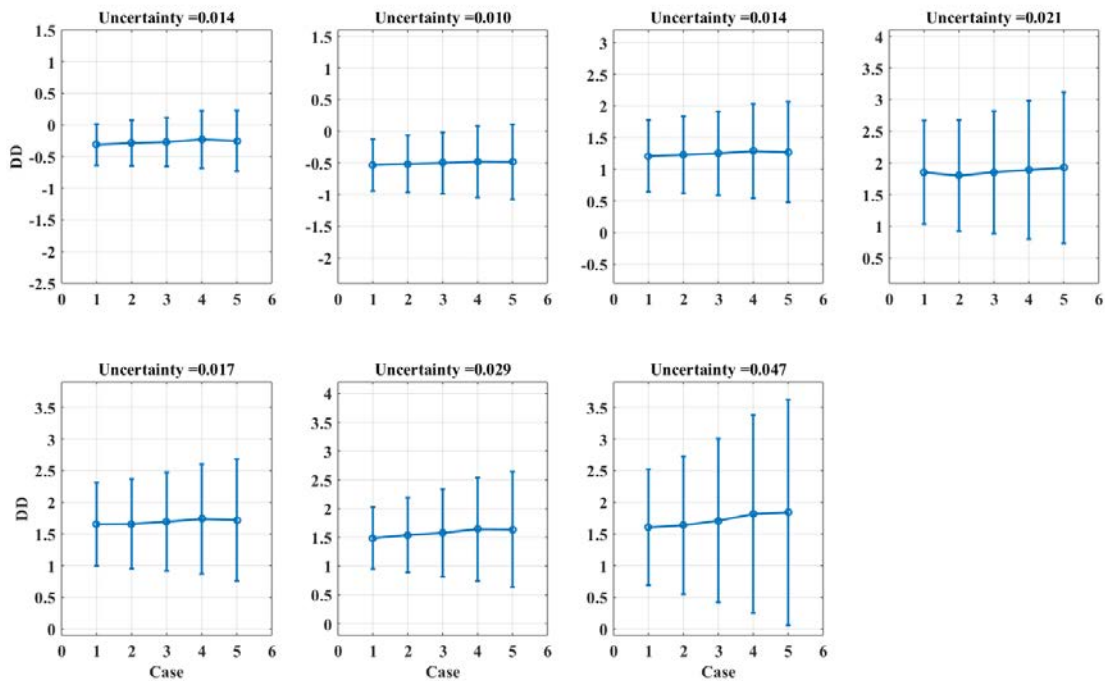


Figure 6-14 Spatial uncertainty of WindSat/GMI intercalibration.

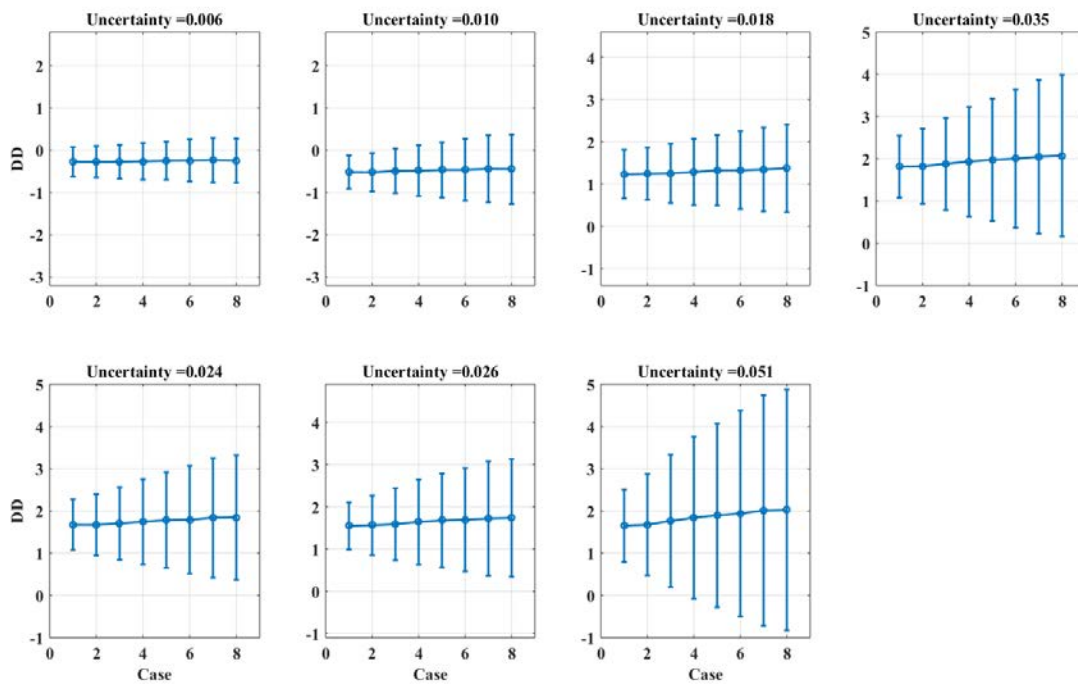


Figure 6-15 Temporal uncertainty of WindSat/GMI intercalibration.

The next step is to apply the MCS procedure 2200 iteration over each region with a total of 17600 per channel. The averaged uncertainty of each iteration are then grouped by region and channel, respectively, and the results are shown in Figures 6-16 and 6-17.

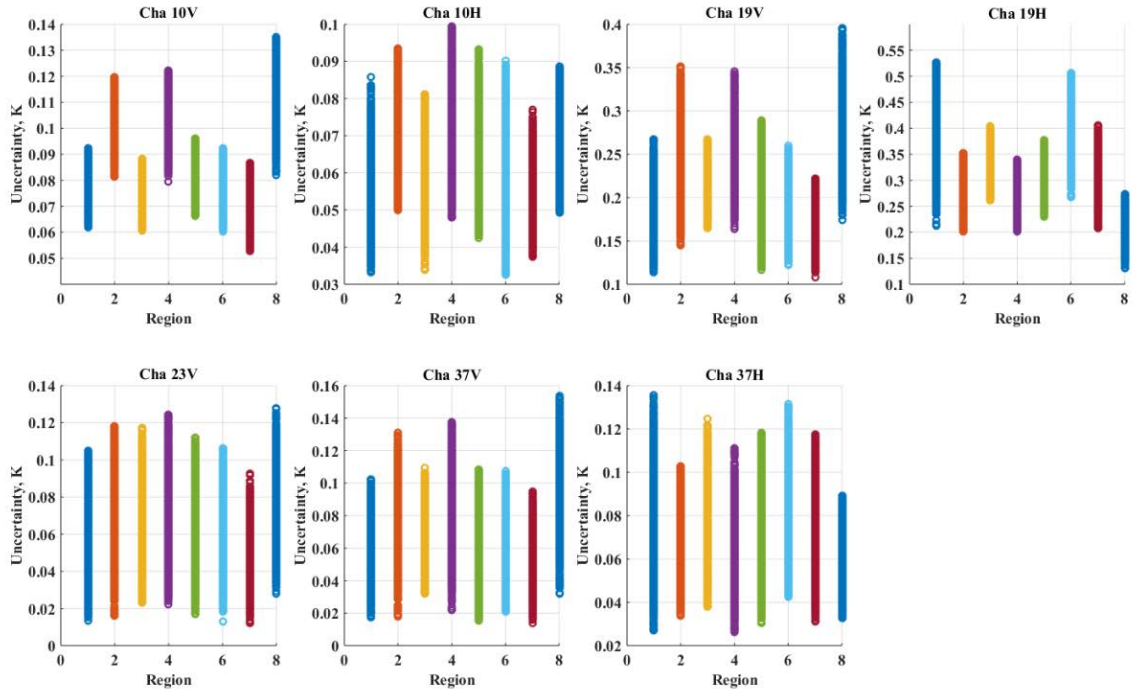


Figure 6-16 GDAS uncertainty of WindSat/GMI intercalibration grouped in region.

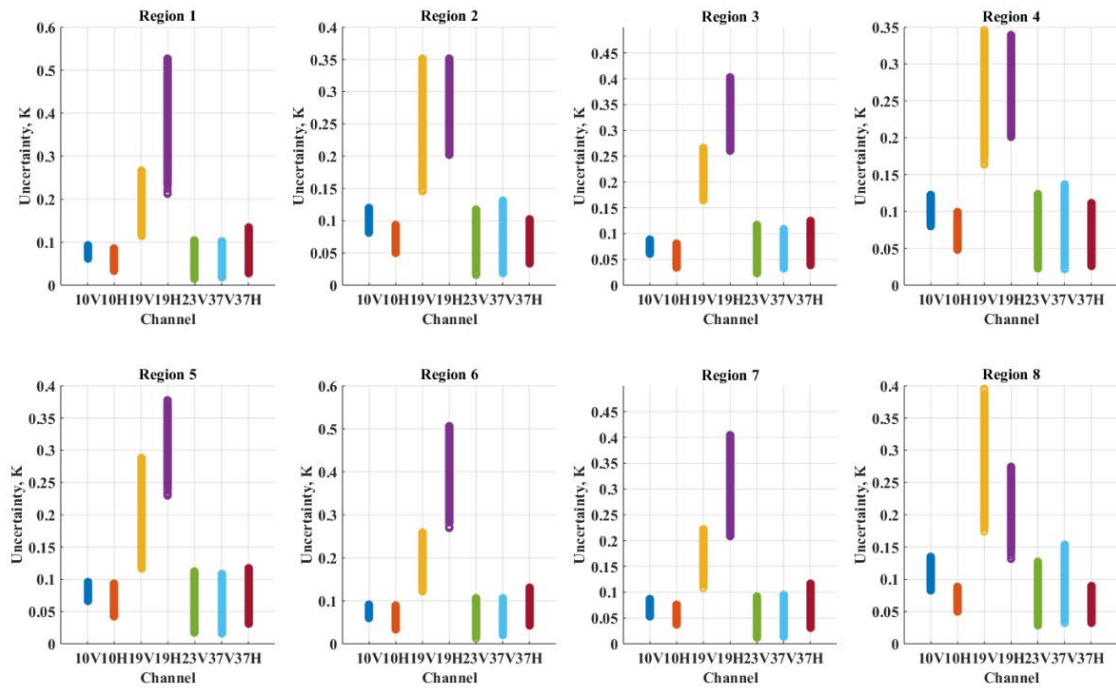


Figure 6-17 GDAS uncertainty of WindSat/GMI intercalibration grouped in channel.

Figure 6-18 presents the uncertainty propagated from Rayleigh-Jeans Approximation from Planck's Law.

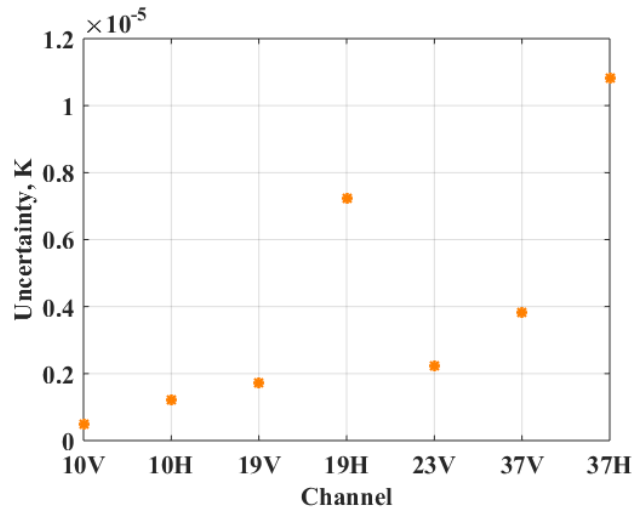


Figure 6-18 Rayleigh-Jeans uncertainty of WindSat/GMI intercalibration.

Moreover, a similar procedure as the one described in Section 5.3.4 is applied to quantify the uncertainty due to differences in Rosenkranz and MONO model, Elsaesser and RSS model, as well as GDAS and ERA-I. Results presented in Table 6-3.

Table 6-3 Uncertainty from model deviation.

Channel	10V	10	19V	19H	23V	37V	37H
MONO & Rosenkranz	0.004	0.009	0.007	0.103	0.037	0.010	0.008
RSS & Elsaesser	0.093	0.021	0.123	0.138	0.037	0.019	0.044
GDAS & ERA-I	0.043	0.033	0.107	0.177	0.034	0.038	0.04

Finally, the uncertainties from all the above-mentioned sources including GMI calibration uncertainty are combined into a final uncertainty per channel, which are presented in Table 6-4.

Table 6-4 Combined uncertainty of WindSat/GMI intercalibration.

Channel	10V	10	19V	19H	23V	37V	37H
Combined standard uncer.	0.422	0.407	0.503	0.577	0.337	0.275	0.286
Combined expanded uncer.	1.266	1.223	1.510	1.732	1.011	0.825	0.857

7 CONCLUSION

In this dissertation, a consistent, multi-decadal, intercalibrated TMI/GMI oceanic *Tb* data record, using WindSat as a calibration bridge, has been achieved by expanding the CFRSL XCAL algorithm to a three-way radiometric intercalibration between TMI, GMI and WindSat. While the CFRSL XCAL algorithm yields the *Tb* bias that can be applied to the TMI 17-plus-year legacy *Tb* product, this is not an absolute bias.

It is often acknowledged that a wide range of uncertainties from various origins accompany estimates of calibration bias, therefore, a generic uncertainty quantification model has been subsequently developed considering all possible uncertainty sources, and it has been applied successfully to this invaluable data record. The sources that could contribute to the final uncertainty of the calibration bias include: variability in spatial and temporal resolutions; uncertainties associated with the environmental parameters that propagate along the CFRSL XCAL algorithm into the calibration bias; the offset of the Rayleigh Jeans approximation from the Planck's Law; the variability in radiative transfer models and numerical weather prediction models; and finally the calibration uncertainty in the transfer standard GMI.

Prior to this research, the calibration biases of TRMM & GPM constellation sensors have been well-derived using the TMI or the GMI as the transfer standard, however, this dissertation has opened the way of quantifying the uncertainty estimates associated with these calibration biases. With this uncertainty model, the resulting GPM/TRMM inter-satellite calibrated *Tb* data record will be significantly improved for scientific utilization (especially for climate studies).

8 FUTURE WORK

Given the generic uncertain quantification model developed in this dissertation along with the CFRSL XCAL algorithm that has been applied successfully to the intercalibration between pairs of instruments among TMI, GMI and WindSat, this UQM model can be applied to the intercalibration of other sensors within the TRMM-GPM constellation. We suggest that the UQM application will result in a unified high-sampling-frequency and globally-covered Tb product with associated boundary uncertainties, which will be much improved for scientific utilization as compared to existing Tb products.

Also, based upon the results of this dissertation (see Section 5.3.2), it is recognized that there is room for improvement in the XCAL for the water vapor sensitive channels. Given the considerable sophistication of the science of water vapor spectroscopy, we doubt that improved RTM physics is likely. Therefore, this suggests that the issue may be associated with the atmospheric water vapor profile input to the RTM. Studies are suggested to use water vapor profile retrieved from millimeter radiometer sounders' measurements (rather than numerical weather predictions) to determine the impact on the DD biases of these problematic channels.

APPENDIX A: GPM CONSTELLATION

Part of the future work is to apply the UQM described in Chapter 5 to the other TRMM and GPM constellation members to drive the global precipitation retrieval product into perspective. This section will talk about the GPM constellation.

The GPM core satellite was launched from the Tanegashima Space Center in Japan on February 28th, 2014. The GMI passive microwave imager on board provides a number of improvements over TMI as well as other spaceborne conically-scanning window channel radiometers. These include increased spatial resolution, the addition of high-frequency channels at 166, 183±3, and 183±7 GHz, and an emphasis on calibration accuracy and stability. The design requirements for GMI were driven both by requirements for its use in building the *a priori* database for the microwave precipitation retrieval algorithm as well as for providing the reference calibration standard for the GPM radiometer constellation. The GMI radiometric uncertainty requirements included the radiometric sensitivity, or noise equivalent delta temperature (NEΔT), the calibration accuracy, and the calibration stability. Some of the GMI calibration related developments include the addition of noise diodes for a four point calibration of the window channels, design considerations to reduce/eliminate calibration issues affecting prior sensors such as emissive reflectors and solar intrusions into the warm load, and multiple on-orbit calibration maneuvers. Details of the GMI calibration are provided in Appendix B.

Due to the inclination of the orbits and their higher observing altitude, the radiometers on board polar-orbiting satellites provide the bulk of the global coverage needed to meet the desired 3-hourly global sampling requirements for the GPM constellation.

The conical-scanning window channel radiometers include TMI, which was turned off on 8 April 2015, the Advanced Microwave Scanning Radiometer 2 (AMSR2) on board GCOM-W1,

and four Special Sensor Microwave Imager/ Sounder (SSMIS) instruments on board the DMSP F16, F17, F18, and F19 spacecraft. Coriolis WindSat is also a conical-scanning radiometer, but it is not currently part of the operational GPM constellation. This is due to the fact that changes in the SDR calibration (i.e. level 1B) are only applied going forward and not reprocessed for a consistent data record. In addition, cross-track sounding radiometers with channels near the 183 GHz water vapor line are used for GPM precipitation retrievals. These currently include the Advanced Technology Microwave Sounder (ATMS) on board the Suomi National Polar-orbiting Partnership (NPP) spacecraft, the Microwave Humidity Sounder (MHS) on board MetOp-A, MetOp-B, NOAA-18, and NOAA-19, and the Sondeur Atmosphérique du Profil d'Humidité Intertropicale par Radiométrie (SAPHIR) on board Megha-Tropiques. Differences in channel availability and characteristics between sensors leads to significant challenges in ensuring consistency in both the input Tb as well as resulting precipitation estimates.

APPENDIX B: GPM CALIBRATION

The use of GMI as a transfer standard demands calibration stability. If the absolute calibration can also be trusted, that simplifies the problem by enabling GMI to be used as both the calibration transfer standard and the reference standard. The design of GMI was predicated on eliminating potential (and in some cases observed) calibration issues. A very high quality reflective coating was used on the main and cold calibration sub-reflectors. Noise diodes were included in the calibration scheme for the channels from 10.7 to 36.64 GHz. This provides a level of redundancy that enables an explicit solution for non-linearity in the radiometer response functions and also provides the ability to bridge across times when the sun, moon, or radio frequency interference is in the cold calibration field-of-view. Additionally, the cold calibration sub-reflector is somewhat oversized to reduce spillover issues and the warm calibration load is shrouded to minimize solar intrusion.

After launch, a series of spacecraft attitude maneuvers were performed to provide checks on and refinements to the calibration. One of these maneuvers involved pitching up the GPM spacecraft so that both the main beam and the cold calibration mirror viewed cold space. The voltage from the radiometers was determined to be identical to within measurement uncertainty for both the main and sub-reflectors, thus indicating that either there are no significant emissivity issues for either reflector or they are identical for both. While it is highly improbable that both reflectors would have identical emissivity issues, even in that case the reflector emissivity would cancel out in the calibration process to the extent that the two reflectors share the same physical temperature. Thus it appears that the choice of the antenna and reflector coating resulted in a non-emissive or very low emissivity reflector.

The GPM spacecraft was also pitched down so that so that the main beam viewed directly at nadir for part of the scan. On average, at nadir there should be no difference in the antenna temperatures between the horizontal and vertical polarizations. An analysis of the nadir viewing data indicated that the differences were less than 0.3 K when viewing the ocean and less than 0.2 K when viewing land surfaces. This also provides a significant constraint on the calibration. Note that due to schedule constraints requiring that the V04 GMI calibration be finalized by mid-2015 in order to meet early 2016 deadlines for GPM product development, preliminary analyses of the attitude maneuvers were used. A more refined analysis has subsequently been performed by Wentz and Draper

For a spaceborne radiometer, the largest source of calibration uncertainty in converting from counts to Tb involves the spillover correction, or the fraction (η) of the total antenna pattern that intercepts the Earth. The pre-launch values were derived from antenna patterns either measured on a near field range or modeled. The bulk of the portion that misses the Earth ($1-\eta$) comes from the portion of the feed pattern that misses the main reflector, *i.e.* the spillover. Unfortunately, given that the spillover estimates from the near field antenna measurements are very uncertain, model results were used instead.

In order to refine the estimates of $1-\eta$, the GPM spacecraft was put into an inertial hold so that the spillover region intercepted the Earth, while the main reflector viewed cold space. While some modeling is required to estimate the Earth Tb , the impact of the uncertainty in these calculations is at least an order of magnitude less than using the Tb modeling directly given that the values of η are all greater than 0.9. The V04 η estimates for the two polarizations at each frequency were found to agree within their uncertainty, so the two values were averaged for each

frequency to reduce the statistical error and to assure that the constraints from the nadir viewing observations were satisfied. These, along with straightforward numbers such as the calibration of the thermistors, constitute a purely physical calibration that is not tuned to any model and is completely independent of the calibration of any other spaceborne microwave radiometer.

With above and intercomparisons with other well-calibrated radiometers such as WindSat and MHS, it is conservative to state that the absolute calibration accuracy of GMI is within 1 K at 37 GHz and below, and 0.5 K above. Furthermore, as mentioned previously the GMI orbit creates many coincident observations with all of the other constellation members from which inter-comparisons can be made. For Version 4, therefore, GMI is used as the calibration reference standard to which all the constellation sensors are adjusted.

**APPENDIX C: ADDITIONAL ANALYSIS OF TMI/WINDSAT
INTERCALIBRATION**

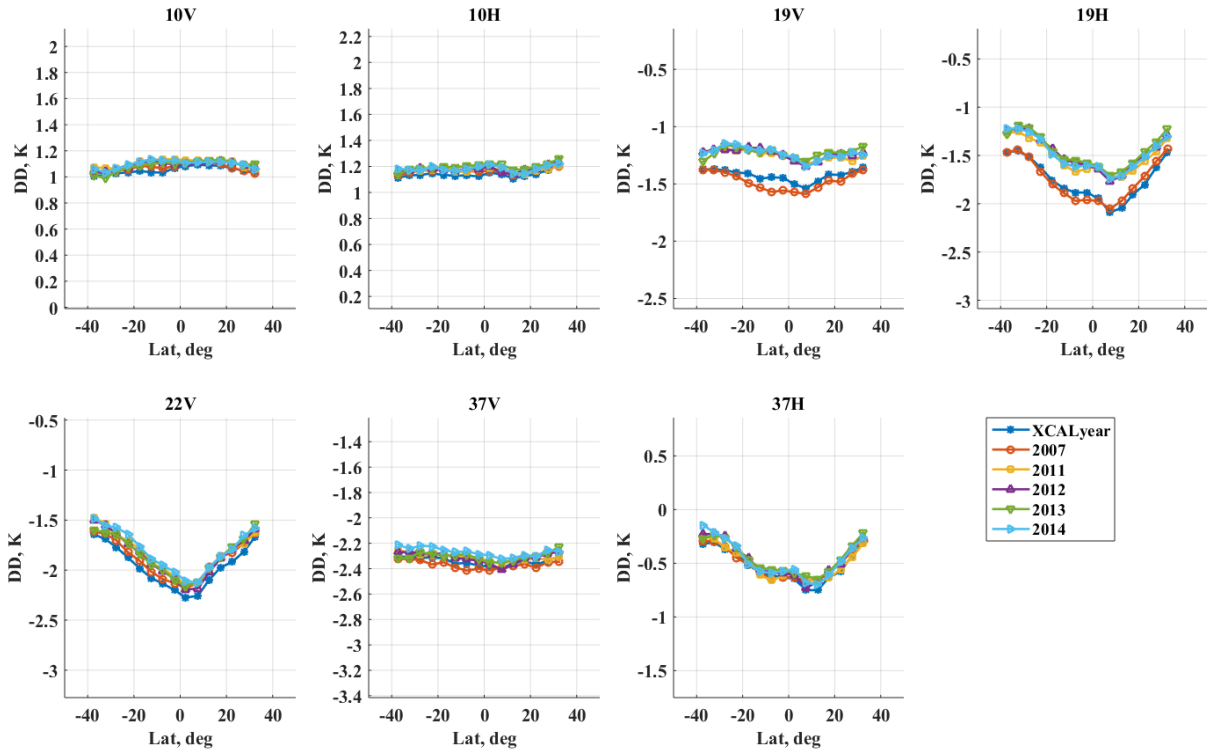


Figure 8-1 Latitude dependence of calibration bias of TMI relative to WindSat. The patterns are stable along the years, and the water vapor channels (19V, 19H, and 22V) present smile shape and a peak—to-peak 0.5 drift along the whole latitude range.

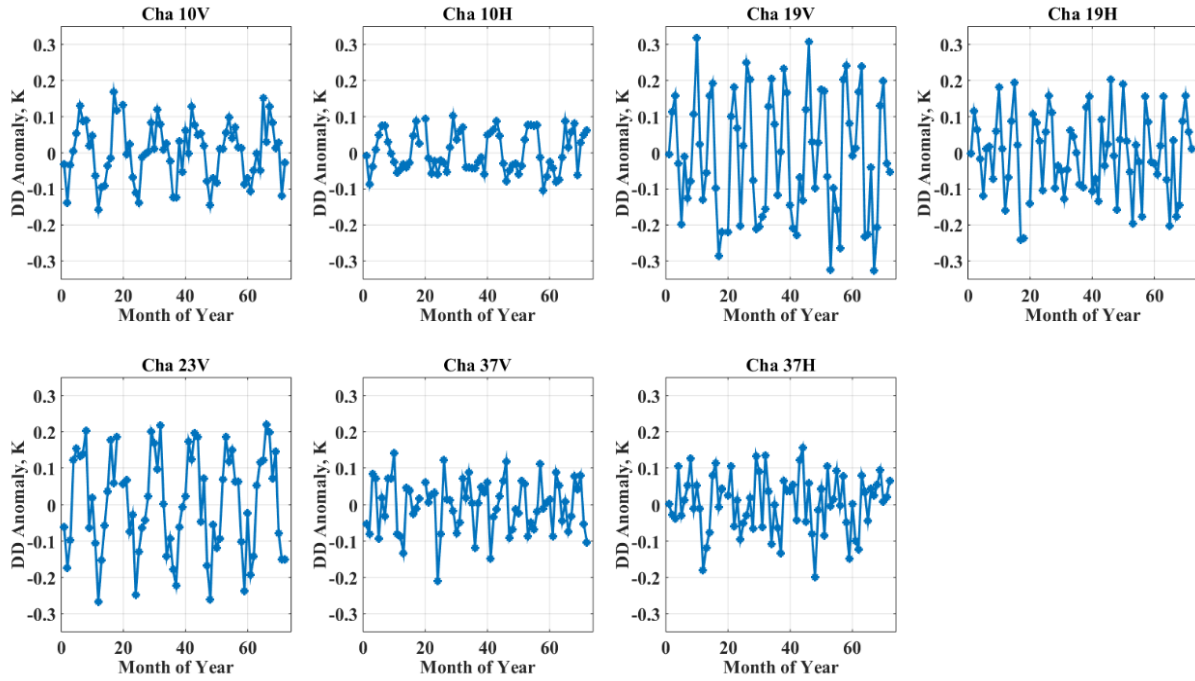


Figure 8-2 Monthly *DD* anomaly in time series from 2005 to 2014, where a cyclic pattern is shown.

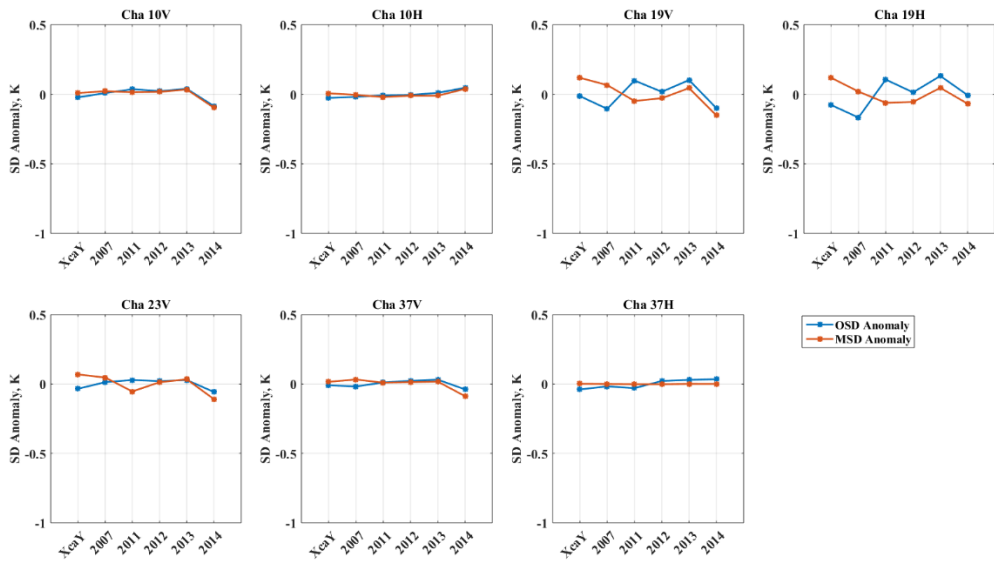


Figure 8-3 Observed mean single difference and simulated (modeled) mean single difference of TMI relative to WindSat for the 6 years.

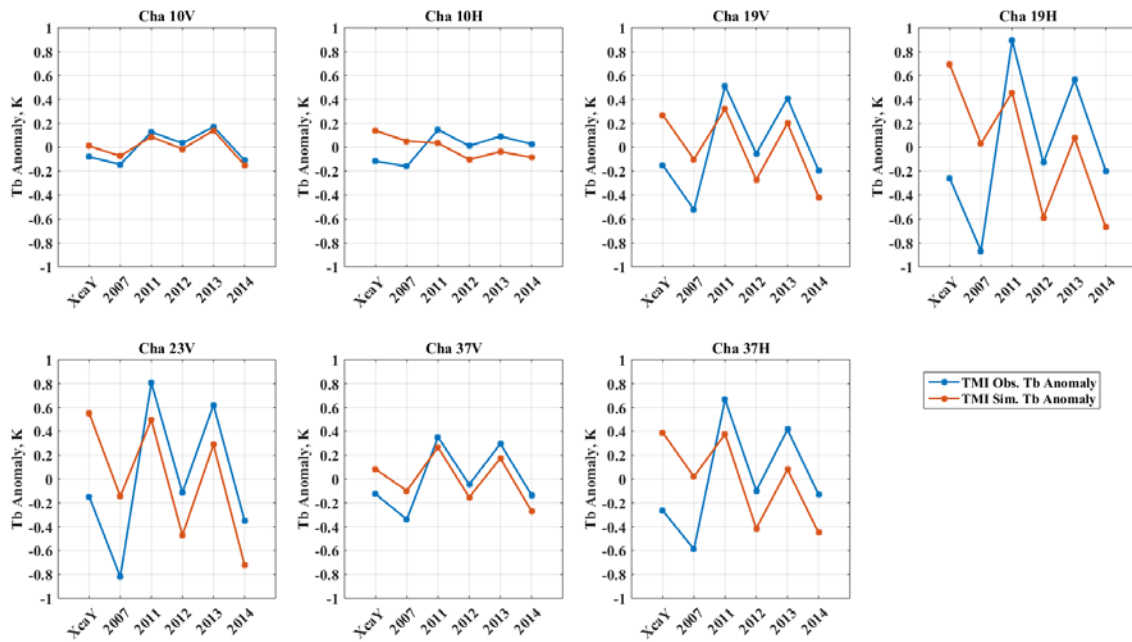


Figure 8-4 Observed and simulated *Tb* anomaly of TMI for the 6 years.

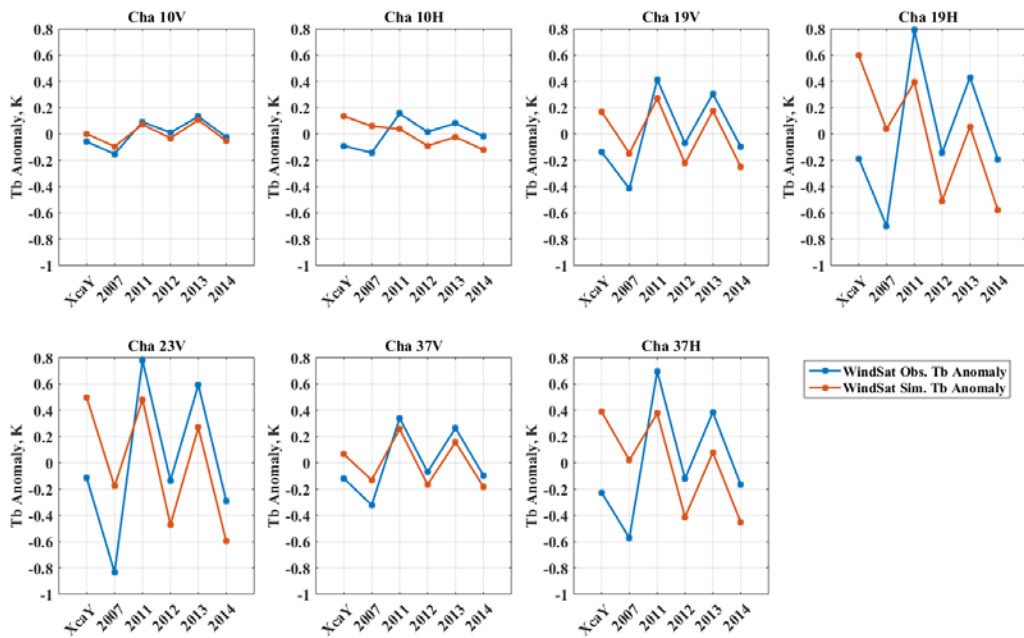


Figure 8-5 Observed and simulated *Tb* anomaly of WindSat for the 6 years.

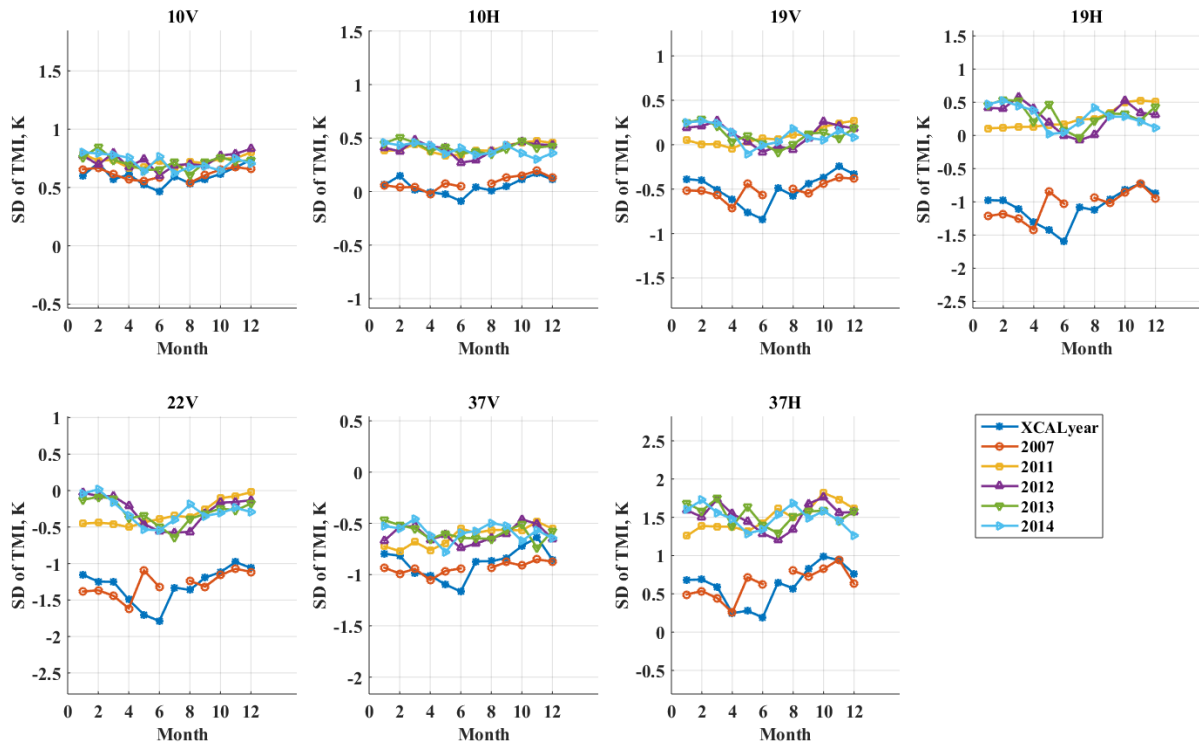


Figure 8-6 TMI single differences for the 6 years.

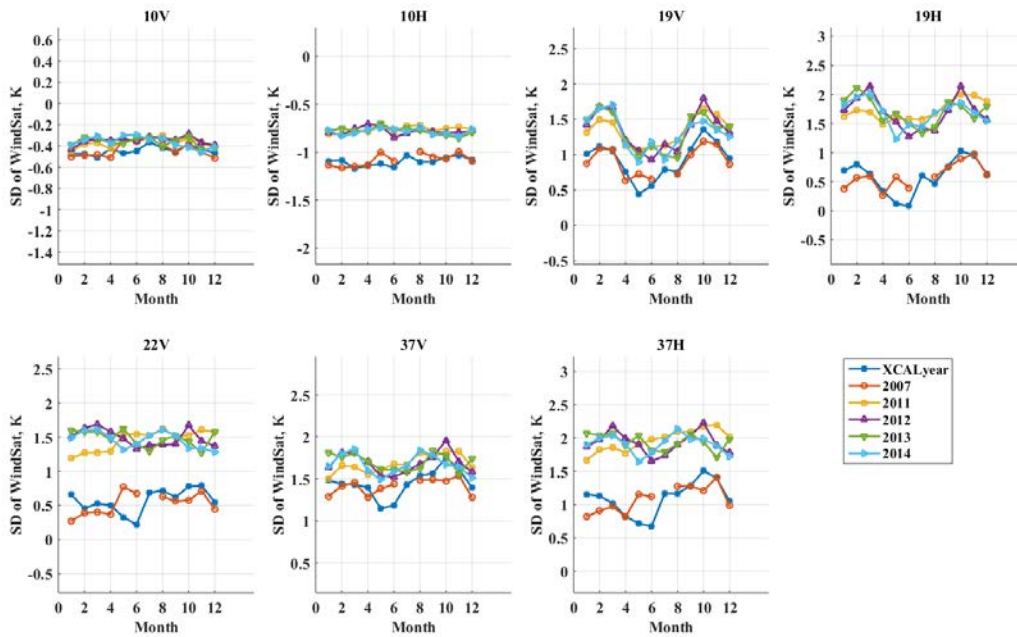


Figure 8-7 WindSat single differences for the 6 years.

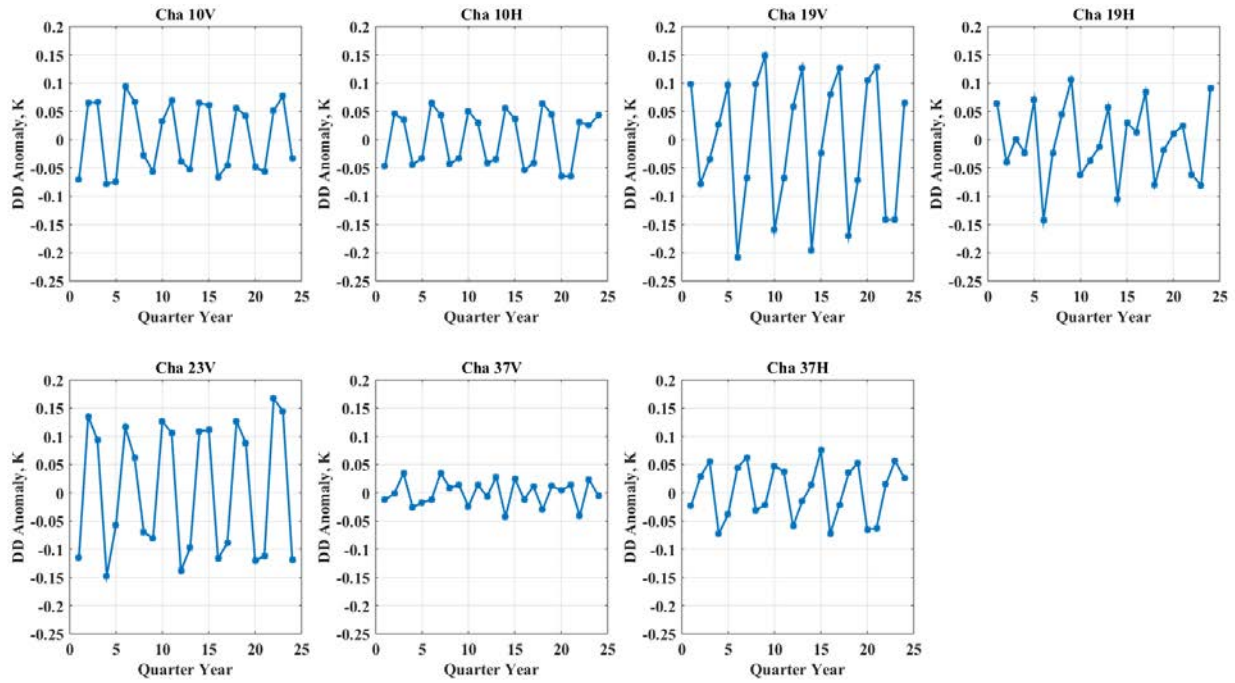


Figure 8-8 Averaged *DD* anomaly for each quarter (3 months) of TMI relative to GMI for the 6 years.

LIST OF REFERENCES

- [1] W. Berg *et al.*, “Intercalibration of the GPM Microwave Radiometer Constellation,” *J. Atmospheric Ocean. Technol.*, vol. 33, no. 12, pp. 2639–2654, Oct. 2016.
- [2] C. Kummerow, W. Barnes, T. Kozu, J. Shiue, and J. Simpson, “The Tropical Rainfall Measuring Mission (TRMM) Sensor Package,” *J. Atmospheric Ocean. Technol.*, vol. 15, no. 3, pp. 809–817, Jun. 1998.
- [3] R. Chen, F. Alquaied, and W. L. Jones, “Assessing Radiometric Stability of the 17-Plus-Year TRMM Microwave Imager 1B11 Version-8 (GPM05) Brightness Temperature Product,” *Climate*, vol. 5, no. 4, p. 92, Dec. 2017.
- [4] A. Y. Hou *et al.*, “The Global Precipitation Measurement Mission,” *Bull. Am. Meteorol. Soc.*, vol. 95, no. 5, pp. 701–722, Sep. 2013.
- [5] D. W. Draper, D. A. Newell, F. J. Wentz, S. Krimchansky, and G. M. Skofronick-Jackson, “The Global Precipitation Measurement (GPM) Microwave Imager (GMI): Instrument Overview and Early On-Orbit Performance,” *IEEE J. Sel. Top. Appl. Earth Obs. Remote Sens.*, vol. 8, no. 7, pp. 3452–3462, Jul. 2015.
- [6] P. W. Gaiser *et al.*, “The WindSat spaceborne polarimetric microwave radiometer: sensor description and early orbit performance,” *IEEE Trans. Geosci. Remote Sens.*, vol. 42, no. 11, pp. 2347–2361, Nov. 2004.
- [7] W. L. Jones, J. D. Park, S. Soisuvarn, L. Hong, P. W. Gaiser, and K. M. S. Germain, “Deep-space calibration of the WindSat radiometer,” *IEEE Trans. Geosci. Remote Sens.*, vol. 44, no. 3, pp. 476–495, Mar. 2006.
- [8] S. K. Biswas, S. Farrar, K. Gopalan, A. Santos-Garcia, W. L. Jones, and S. Bilanow, “Intercalibration of Microwave Radiometer Brightness Temperatures for the Global Precipitation Measurement Mission,” *IEEE Trans. Geosci. Remote Sens.*, vol. 51, no. 3, pp. 1465–1477, Mar. 2013.
- [9] National Centers For Environmental Prediction/National Weather Service/NOAA/U.S. Department Of Commerce, “NCEP FNL Operational Model Global Tropospheric Analyses, continuing from July 1999.” UCAR/NCAR - Research Data Archive, 2000.
- [10] D. P. Dee *et al.*, “The ERA-Interim reanalysis: configuration and performance of the data assimilation system,” *Quart J Roy Meteor Soc*, vol. 137, pp. 553–597, 2011.
- [11] K. Gopalan, “A Time-Varying Radiometric Bias Correction for The TRMM Microwave Imager,” Ph.D. dissertation, Dept. Electrical and Computer Engineering, University of Central Florida, Orlando, FL, 2008.
- [12] T. Meissner and F. J. Wentz, “The Emissivity of the Ocean Surface Between 6 and 90 GHz Over a Large Range of Wind Speeds and Earth Incidence Angles,” *IEEE Trans. Geosci. Remote Sens.*, vol. 50, no. 8, pp. 3004–3026, Aug. 2012.
- [13] J. L. Moncet and S. A. Clough, “Accelerated monochromatic radiative transfer for scattering atmospheres: Application of a new model to spectral radiance observations,” *J. Geophys. Res. Atmospheres*, vol. 102, no. D18, pp. 21853–21866, Sep. 1997.
- [14] P. W. Rosenkranz, “Water vapor microwave continuum absorption: A comparison of measurements and models,” *Radio Sci.*, vol. 33, no. 4, pp. 919–928, Jul. 1998.

- [15] H. J. Liebe, G. A. Hufford, and T. Manabe, "A model for the complex permittivity of water at frequencies below 1 THz," *Int. J. Infrared Millim. Waves*, vol. 12, no. 7, pp. 659–675, Jul. 1991.
- [16] H. J. Liebe, P. W. Rosenkranz, and G. A. Hufford, "Atmospheric 60-GHz oxygen spectrum: New laboratory measurements and line parameters," *J. Quant. Spectrosc. Radiat. Transf.*, vol. 48, no. 5, pp. 629–643, Nov. 1992.
- [17] P. Rosenkranz, "Absorption of Microwaves by Atmospheric Gases," John Wiley and Sons, 1993.
- [18] R. Chen, H. Erahimi, and W. L. Jones, "Sensitivity of XCAL double difference approach to ocean surface emissivity and its impact on inter-calibration in GPM constellation," in *2016 IEEE International Geoscience and Remote Sensing Symposium (IGARSS)*, 2016, pp. 871–874.
- [19] G. S. Elsaesser and C. D. Kummerow, "Toward a Fully Parametric Retrieval of the Nonraining Parameters over the Global Oceans," *J. Appl. Meteorol. Climatol.*, vol. 47, no. 6, pp. 1599–1618, Jun. 2008.
- [20] R. Chen, A. Santos-Garcia, S. Farrar, and W. L. Jones, "Assessment of the long-term radiometric calibration stability of the TRMM microwave imager and the WindSat Satellite Radiometers," in *2014 13th Specialist Meeting on Microwave Radiometry and Remote Sensing of the Environment (MicroRad)*, 2014, pp. 187–191.
- [21] T. Wilheit *et al.*, "A Consensus Calibration based on TMI and Windsat," in *2011 IEEE International Geoscience and Remote Sensing Symposium*, 2011, pp. 2641–2644.
- [22] R. Chen, H. Ebrahimi, and W. L. Jones, "Creating a Multidecadal Ocean Microwave Brightness Dataset: Three-Way Intersatellite Radiometric Calibration Among GMI, TMI, and WindSat," *IEEE J. Sel. Top. Appl. Earth Obs. Remote Sens.*, vol. 10, no. 6, pp. 2623–2630, Jun. 2017.
- [23] "JCGM 100: 2008, Evaluation of measurement data - Guide to the expression of uncertainty in measurement." 2008.
- [24] I. Farrance and R. Frenkel, "Uncertainty in Measurement: A Review of Monte Carlo Simulation Using Microsoft Excel for the Calculation of Uncertainties Through Functional Relationships, Including Uncertainties in Empirically Derived Constants," *Clin. Biochem. Rev.*, vol. 35, no. 1, pp. 37–61, Feb. 2014.
- [25] S. R. Smith, D. M. Legler, and K. V. Verzone, "Quantifying Uncertainties in NCEP Reanalyses Using High-Quality Research Vessel Observations," *J. Clim.*, vol. 14, no. 20, pp. 4062–4072, Oct. 2001.
- [26] F. T. Ulaby and D. G. Long, "Microwave Radiometry and Radiative Transfer," in *Microwave Radar and Radiometric Remote Sensing*, Ann Arbor, 2014, pp. 255–256.